



HAL
open science

Simulations of plasma sputtering deposition and thin film growth

Lu Xie

► **To cite this version:**

Lu Xie. Simulations of plasma sputtering deposition and thin film growth. Other [cond-mat.other]. Université d'Orléans, 2013. English. NNT : 2013ORLE2024 . tel-00933201

HAL Id: tel-00933201

<https://theses.hal.science/tel-00933201>

Submitted on 20 Jan 2014

HAL is a multi-disciplinary open access archive for the deposit and dissemination of scientific research documents, whether they are published or not. The documents may come from teaching and research institutions in France or abroad, or from public or private research centers.

L'archive ouverte pluridisciplinaire **HAL**, est destinée au dépôt et à la diffusion de documents scientifiques de niveau recherche, publiés ou non, émanant des établissements d'enseignement et de recherche français ou étrangers, des laboratoires publics ou privés.



UNIVERSITÉ D'ORLÉANS



ÉCOLE DOCTORALE
ENERGIE, MATERIAUX, SCIENCES DE LA TERRE ET DE L'UNIVERS

LABORATOIRE GREMI

THÈSE présentée par :
Lu Xie

soutenue le : **02 septembre 2013**

pour obtenir le grade de : **Docteur de l'université d'Orléans**

Discipline/ Spécialité : Physique

**Simulations du dépôt par pulvérisation
plasma et de la croissance de couches
minces**

THÈSE dirigée par :

Jean-Marc BAUCHIRE MC, HdR , GREMI, Orléans
Pascal BRAULT DR CNRS, GREMI, Orléans

RAPPORTEURS :

Erik NEYTS Professeur, Université d'Anvers
Alain DOLLET DR CNRS, PROMES, Perpignan

JURY :

Jean-Marc BAUCHIRE MdC, HdR, GREMI, Université d'Orléans,
Pascal BRAULT DR CNRS, GREMI, Université d'Orléans
William BUSSIÈRE MdC, HdR, LAEPT, Université Blaise Pascal
Alain DOLLET DR CNRS, PROMOES, Université Perpignan
Erik NEYTS Professeur, PLASMANT, Université d'Anvers
Leanne PITCHFORD DR CNRS, LAPLACE, Université Paul-Sabatier
Anne-Lise THOMANN CR CNRS, HdR, GREMI, Université d'Orléans

I dedicate this to my sister, Wenxu Zhang.

Acknowledgments

Completing my PhD degree is probably the most challenging activity of my first 27 years of my life. The best and worst moments of my doctoral journey have been shared with many people. It has been a great privilege to spend 3 years in GREMI, and its members will always remain dear to me. I deeply thanks Prof. C. Leborgne, director, for welcoming me in GREMI.

Foremost, I would like to express my greatest thanks to my supervisor, Dr. Pascal Brault. To Pascal, I attribute my understanding of how to do good science, and, as important, how to communicate that science to others. Even without basic knowledge of Molecular dynamic simulation, he teaches me everything from zero and he gives me unconditional belief and faith, which encouraged me from the first day on. His patience, motivation, enthusiasm, and immense knowledge never failed to inspire me.

Utmost gratitude to my second supervisor, Jean-Marc Bauchire, His determination and perseverance strengthen my belief to swim upstream in science difficult problem. His teachings on plasma physics, fluid dynamics, and partial differential equations led me to develop the necessary theoretical background in the least possible time.

A big thanks to Dr. Anne-Lise Thomann for her guidance and support for my thesis. Her knowledge in the experiment had a tremendous help for me to complete this work. Besides, I would like to thank the rest of my thesis committee: Prof. Erik Neyts, Dr. Alain Dollet, Dr. William Bussière, and Dr. Leanne Pitchford, for their encouragement, insightful comments, and hard questions.

Furthermore, my friends in the lab were sources of laughter, joy, and support. Special thanks go to Hagop Tawidian, Pierre Audier, Laurent schwaederlé, Lucile Pentecoste, Cuynet Stephane, Hervé Hidalgo. I am very happy that, in many cases, my friendships with you have extended well beyond our shared time in GREMI.

Finally, I love and respect my parents and my sister for giving me full support and having faith in me. Their love provided my inspiration and was my driving force. I owe them everything and wish I could show them just how much I love and appreciate them.

Lu XIE

August 2013

Summary

Chapter 1: Introduction	6
1.1 Plasma magnetron sputtering deposition	7
1.2 Molecular dynamics simulation of magnetron sputtering deposition of thin film	10
1.3 Thesis Outline	11
Chapter 2: Molecular dynamics simulations	12
2.1 Classical molecular dynamics	12
2.1.1 The Algorithm of MD simulation	14
2.1.2 Boundary conditions	17
2.1.3 The thermostat for controlling temperature	19
2.1.4 Interatomic potentials in the MD simulation	20
2.2 The setup model in plasma environment	26
2.2.1 Plasma environment in MD simulations	26
2.2.2 The MD model for deposition	28
2.3 The analysis method	30
Chapter 3: Molecular dynamics simulation of Zr_xCu_{100-x} thin film growth	35
3.1 Introduction	35
3.2 Experimental part	37
3.3 MD Model configuration	38
3.4 Result and discussion	38
3.4.2.2 Result and discussion in Condition 2	52
3.4.2.3 Result and discussion in condition 3	58
3.5 Solid-solution formation rules for the system Zr_xCu_{100-x}	64
3.6 Conclusions	66
Chapter 4: Molecular dynamics simulation of AlCoCrCuFeNi high entropy alloy thin film deposition and annealing onto silicon	67
4.1 Introduction	67
4.2. Experiments	69
4.3 MD simulation of magnetron sputtering deposition	70
4.4 Results and discussion	71
4.4.1 AlCoCrCuFeNi clusters growth onto silicon using potential of EAM	71
4.4.2 AlCoCrCuFeNi thin film deposition onto silicon with small size cell	78
4.4.3 AlCoCrCuFeNi thin film deposition and annealing onto silicon using hybrid of EAM and Lennard-Jones potentials	86
4.5 Conclusions	96
Chapter 5: Molecular dynamics simulations of platinum atom deposition onto nanostructured carbon	98
5.1 Introduction	98
5.2 Computational details	99
5.3 Result and discussion	102
5.3.1 Platinum atom deposit on carbon nanotube array	102
5.3.2 Platinum atom deposit on porous carbon with Pt - C LJ potential	106
5.3.3 Platinum atom deposit on porous carbon with Pt - C LJ potential 2	110
5.4 Conclusion	114
Chapter 6: Two dimensional fluid model for magnetron plasma discharge with COMSOL	115
6.1 Introduction	115
6.2 Formulation review	118
6.2.1 The electron equations	118

6.2.3 The electric and static magnetic fields equations.....	123
6.2.4 Input data.....	124
6.3 Numerical procedure with COMSOL	127
6.3.1 Geometry.....	127
6.3.2 Materials and initial value	129
6.3.3 Model implementation	129
6.3.4 Boundary conditions	130
6.3.5 Mesh.....	133
6.4 Preliminary result	133
6.5 Conclusion.....	138
Chapter 7: Conclusion and future work	140
Summary	141
Future Work	144
References	147

Chapter 1: Introduction

La compréhension de la croissance de couches minces est d'une importance primordiale dans les technologies de revêtement notamment pour améliorer les propriétés des films, à la fois générale (structural, l'adhérence, ...) et (protection, barrière thermique, catalytique, chimique, biocompatibilité, ...) spécifique.

La croissance de couches minces dépend des conditions de dépôt ainsi que la nature du substrat: composition et morphologie. Le présent travail se concentrera sur l'étude numérique de la croissance d'agrégats et de films mince pour comprendre dépôt par pulvérisation cathodique magnétron et des mécanismes de croissance dans certains cas spécifiques comme les applications en catalyse (en particulier, les couches catalytiques des piles à combustible) et de la mécanique (multi-couches minces métalliques complexes).

1.1 Les dépôts plasma magnétron

La technique de dépôt par pulvérisation magnétron a été choisie pour les études de croissance de couches minces au GREMI en raison de sa facilité de contrôle sur la composition et la microstructure, des taux de dépôt relativement élevés et de sa simplicité conceptuelle. De plus, elle est largement utilisée pour le dépôt de couches minces et de revêtements dans l'industrie. Fondamentalement, les ions créés dans le plasma sont responsables du processus de pulvérisation. Habituellement, un gaz rare tel que l'Ar est utilisé, ainsi les ions Ar^+ créés sont accélérés vers la cathode, polarisée négativement, avec une énergie cinétique correspondant à cette chute de potentiel. Ils bombardent alors la cible, déclenchant une cascade de collisions dans la cible. Ceci conduit à l'éjection éventuelle d'un atome de la surface. Les atomes pulvérisés se déplacent à travers le plasma et peuvent être déposés sur un substrat faisant face à la cible et ensuite il y a donc formation d'un film.

Parallèlement à l'utilisation généralisée de cette technologie et l'augmentation de la complexité des matériaux qui peuvent être synthétisés, l'effort de recherche a été consacré à la compréhension des mécanismes fondamentaux à l'échelle atomique déterminant la croissance, le développement de la microstructure et la composition. Le fait que les plasmas peuvent modifier considérablement les surfaces est lié à la complexité du plasma. De plus, il est difficile, expérimentalement, de détecter et d'étudier directement les effets des espèces au niveau des surfaces. Cette complexité des processus limite également le recours à des méthodes purement théoriques. Donc, d'une manière pertinente de procéder est de développer et d'appliquer des simulations numériques au niveau moléculaire pour interpréter les mesures de laboratoire. Une technique populaire pour simuler les interactions plasma-surface est la dynamique moléculaire (MD). D'autre part, en raison de la nécessité de conditions initiales plus précises et réalistes pour la simulation des phénomènes de croissance à l'aide de MD, la simulation de la phase plasma, en particulier du transport d'espèces vers la surface est également hautement souhaitable.

1.2 Simulation par Dynamique Moléculaire du dépôt de films minces par pulvérisation magnétron.

L'approche par dynamique moléculaire utilise la loi de Newton avec des potentiels interatomiques appropriés pour résoudre les équations du mouvement. Elle peut donc déterminer à chaque instant les vitesses et les positions atomiques. Il est donc possible d'avoir un aperçu des phénomènes de croissance à l'échelle moléculaire. Frenklach fournit un bilan utile des méthodes générales sur les modèles thermodynamiques, cinétiques qu'il a utilisé pour simuler des réactions de surface associés au dépôt chimique en phase vapeur (CVD) [1]. Cavallotti et al ont énoncé des remarques similaires sur le défi que constitue le large éventail d'échelles à aborder dans les réacteurs CVD [2]. Halley et al précise que les interactions de surface couvrent environ 10 ordres de grandeur [3], tout comme dans les interactions plasma-surface [4]. Afin de bien traiter les conditions initiales de croissance, il est important de tenir compte de la distribution d'énergie des atomes pulvérisés, de la composition chimique de la vapeur d'atomes afin de bien décrire les mécanismes d'assemblage d'atomes au cours de la croissance du film [4-7]. Les réactions en phase gazeuse pendant le transport vers le substrat et les processus chimiques de surface doivent être pris en compte pour la description des interactions plasma-surface [4]. Par ailleurs, en pulvérisation magnétron équilibré, le flux d'ions sur le substrat est faible. Si cela est nécessaire, les ions impactant le substrat / film peuvent être considérés comme des particules neutralisées avec l'énergie des ions impactant la surface du substrat.

1.3 Organisation du document

L'objectif général de cette étude est de contribuer à la compréhension des mécanismes fondamentaux de croissance de film, la formation de la structure et de la composition lors de dépôts par pulvérisation plasma. Le manuscrit de thèse est donc articulé comme suit :

Le chapitre 2 commence avec la présentation des simulations par Dynamique Moléculaire. Nous discutons ensuite du modèle spécifique de simulation de la MD en configuration de plasma de dépôt par pulvérisation cathodique. Enfin, nous présentons les méthodes d'analyse des données générées par la simulation MD et les règles de formation de solutions solides d'alliage multi-composants.

Dans le chapitre 3, nous présentons les résultats de simulations de MD sur une étude structurale des alliages métalliques en couches minces Zr_xCu_{100-x} produits lors des dépôts par plasma de pulvérisation magnétron.

Dans le chapitre 4, nous étudions le dépôt et les propriétés après recuit d'alliages à haute entropie (HEA) en couches minces AlCoCrCuFeNi sur substrats Si (100).

Dans le chapitre 5, nous utilisons les simulations par dynamique moléculaire pour étudier l'évolution structurale et dynamique d'atomes de platine déposés sur des substrats carbonés nanostructurés (réseau de nanotubes de carbone et de carbone poreux, respectivement) avec trois distributions d'énergie de dépôt.

Le chapitre 6 présente un modèle fluide de référence à deux dimensions (r, z), en fonction du temps décrivant le transport de deux espèces chargées, ions et électrons positif, dans un réacteur cylindrique en courant continu symétrique magnétron plan. Ensuite, nous utilisons COMSOL pour résoudre les équations non linéaires corrélées décrivant le plasma de pulvérisation.

Dans le chapitre 7, les résultats importants des travaux présentés sont résumés et des orientations futures possibles de ce travail sont suggérées.

The understanding of growth of thin films is of paramount importance in coating technologies especially for improving films properties, both general (structural, adhesion, ...) and specific (protective, thermal barrier, catalytic, chemical, biocompatibility, ...).

Thin film growth is dependent on deposition conditions as well as substrate nature: composition and morphology. The present work will focus on studying numerically growth of clusters and films for understanding magnetron sputtering deposition and growth in some specific cases relevant for applications in catalysis (especially catalytic layers of fuel cells) and in mechanics (complex multicomponent metallic thin films).

1.1 Plasma magnetron sputtering deposition

Plasma is referred to as the fourth state of matter, and consists of a partially ionized gas. The presence of reactive ions and electrons, and the interactions between them, is the origin of plasma applications. Besides plasmas in the universe like stars, sun wind, lightning... Laboratory plasmas are very often subdivided into two groups, according to their

temperature. The plasmas that are investigated in this work are low temperature plasmas or gas discharges.

A gas discharge is generated by applying a sufficiently high potential difference between two electrodes placed in a gas. The generated electric field partially breaks down the gas into ions and electrons, which can interact in different plasma processes. When besides the electric field, also a magnetic field is applied, the electrons can be used more efficiently. Magnetrons make use of the fact that a magnetic field configured parallel to the target surface can constrain electron motion to the vicinity of the target. The magnets are arranged in a way that one pole is positioned at the central axis of the target and the second pole is formed by a ring of magnets around the outer edge of the target. Trapping the electrons in this way substantially increases the probability of an ionising electron-atom collision occurring. The increased ionization efficiency of a magnetron results in a dense plasma in the target region. This, in turn, leads to increased ion bombardment of the target, giving higher sputtering rates and, therefore, higher deposition rates at the substrate. In addition, the increased ionisation efficiency achieved in the magnetron mode allows the discharge to be maintained at lower operating pressures and lower operating voltages than is possible in the basic sputtering mode.

Magnetron plasma sputtering deposition has been chosen for thin film growth studies in GREMI due to its versatility, control over the composition and microstructure, relatively high deposition rates and conceptual simplicity and because it is widely used for deposition of thin films and coatings in industry. Basically the ions created during the plasma ignition and at stationary operation are responsible for the sputtering process. Usually a rare gas like Ar is used and Ar^+ ions are accelerated to the negatively biased cathode with a sufficient kinetic energy. They are thus bombarding the target, which initiates a collision cascade in the target,

leading to a possible release of a surface atom. The sputtered atoms travel through the plasma and can be deposited on a substrate facing the target and then, forming a coating. The plasma sputter deposition mechanism is schematically presented in figure 1.1.

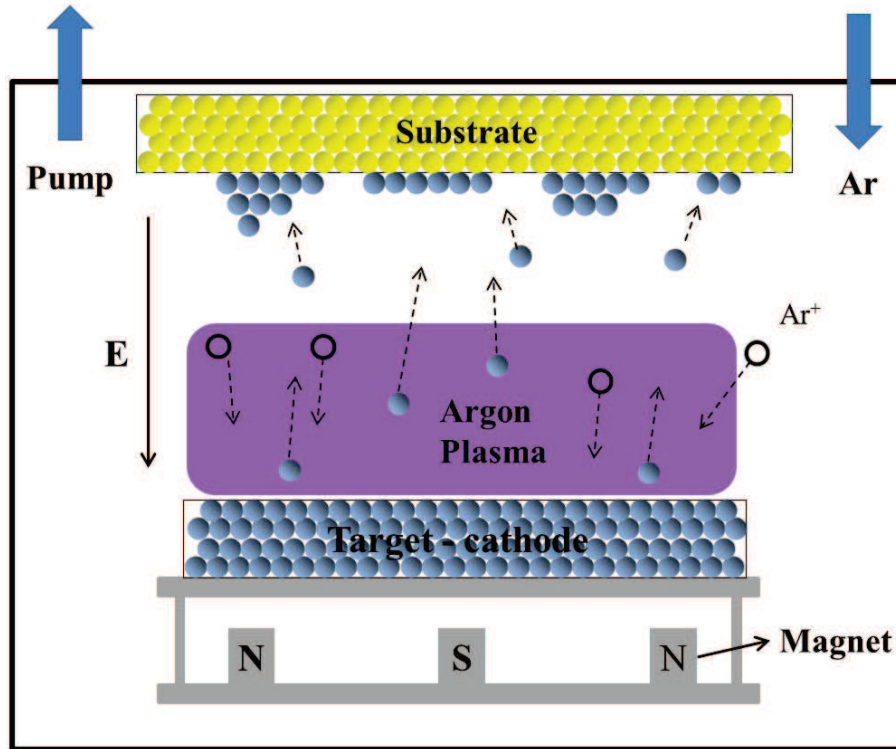


Figure 1.1- Schematic presentation of the magnetron sputtering deposition process

Parallel to the widespread use of this technology and the increase of complexity of the materials that can be synthesized, research effort has been devoted towards understanding the fundamental atomistic mechanisms that determine growth, structure formation and phase composition in materials. Actually, the fact that plasmas can alter surfaces dramatically with such a wide range of effects is related to the complexity of the sputtering plasma itself and the target. Meanwhile, it is hard to directly detect and study in experiments the effects of the impacting species occurring at surfaces in the plasma, especially to probe the mechanisms in situ and in real time. This complexity of the processes also limits the use of purely theoretical methods. So a relevant way to proceed is to develop and apply numerical simulations at the molecular level to interpret laboratory measurements. A popular technique to simulate

plasma–surface interactions are molecular dynamics (MD) simulations. On the other hand, due to the need of more precise and realistic initial conditions for simulating growth phenomena using MD, relevant plasma phase simulation resulting in the transport of depositing species is highly desirable too.

1.2 Molecular dynamics simulation of magnetron sputtering deposition of thin film

The molecular dynamics approach uses Newton's law and suitable interatomic potentials to solve the equations of motion and thus can determine at each time the atom velocities and positions. So it is possible, to have insights in growth phenomena at the molecular scale. Frenklach provides a useful summary of the general methods about thermodynamic models, general kinetic which he used to simulate surface reactions associated with chemical vapor deposition (CVD) [1]. Cavallotti et al make similar points about the challenges of addressing the large range of scales in CVD reactors and include a discussion including reactor-scale phenomena [2]. Halley et al point out that it is very important that the processes of electrochemical – surface interactions span about 10 orders of magnitude [3], similar to estimates for plasma–surface interaction studies [4]. As a result, it is convenient to introduce the sputtered atom energy distribution, chemical composition for describing the mechanisms of atom assembly during film growth [4-7]. Gas-phase reaction during travelling to the substrate and surface chemical process should be taken into account for describing plasma-surface interactions [4]. Moreover in balanced magnetron sputtering deposition, primary ion flux is negligible. If not, ions impinging the substrate/film can be considered as neutralized particles with the ion incoming energy.

1.3 Thesis Outline

The overall goal of this research is to contribute to the understanding of the fundamental atomistic mechanisms of film growth, structure formation and phase composition under plasma sputtering deposition conditions. The outline of our work is as follows:

Chapter 2 begins with the presentation of MD simulation. We then discuss the setup MD simulation model of plasma sputter deposition. Finally, we introduce the data analysis methods and the solid-solution forming rules for multi-components alloy.

In chapter 3, we report on results of MD simulations and on a structural study of Zr_xCu_{100-x} metal alloy thin films grown by magnetron plasma sputter deposition.

In chapter 4, we study the deposition and annealing properties of AlCoCrCuFeNi high entropy alloy (HEA) thin film on Si(100) substrates.

In chapter 5, we use MD simulations to investigate the structural and dynamical evolution of platinum atoms deposited on nanostructured carbon substrates (carbon nanotube array and porous carbon) with three deposition energy distributions.

Chapter 6 firstly present a reference two-dimensional (r, z), time-dependent fluid model approach describing the transport of two charged species, electron and positive ions, in a cylindrical symmetric dc planar magnetron reactor. Then we use COMSOL to solve the correlated non-linear equations describing the sputtering plasma.

In Chapter 7, the important results of the work presented are summarized, and future directions for related research are suggested.

Chapter 2: Molecular dynamics simulations

Le but de ce chapitre est de fournir au lecteur les éléments de mise en œuvre de la dynamique moléculaire classique (MD) nécessaires à la description de la croissance de couches. Ce chapitre peut être considéré comme introduction aux chapitres suivants. Je commence avec la présentation des fondements de la dynamique moléculaire classique et des méthodes d'intégration numérique, les différents potentiels interatomiques semi-empirique de paire, à 3-corps et à N-corps, le contrôle de température et de l'énergie (thermostats) et des conditions aux limites périodiques. Je discute ensuite la configuration d'un modèle de simulation de DM pour la pulvérisation dépôt plasma. Enfin, je présente les méthodes d'analyse des données générées par les simulations MD, au rang desquelles on trouvera les distributions de densité radiale, la détermination des spectres de diffraction X, les règles de formation de solutions solides.

The purpose of this chapter is to provide reader with the implementation of classical molecular dynamics (MD) simulation for describing thin film growth issued from plasma sputtering deposition. This chapter may be regarded as both introductory and supplemental to the following chapters. I begin with the presentation of the foundation of classic molecular dynamic simulation which involves the introduction of numerical integration, various analytical interatomic empirical potential for pair, 3-body and N-body interaction, temperature and energy control (thermostats) and periodic boundary conditions. I then discuss the setup of MD simulation model for plasma sputtering deposition. Finally, I introduce the analysis methods for the data generated by MD simulation.

2.1 Classical molecular dynamics

Classical molecular dynamics (MD) is a method intended to numerically solve the Newton equations of motion for a given system of particles, for which the interactions are governed by a model describing the forces between these particles. Molecular dynamic simulations are originally developed in the late 1950s and used for the study of atomic vibrations in molecules. [8-10]. Alder and Wainwright in 1957 study a solid-fluid transition in a system composed of hard spheres interacting by instantaneous collisions [11], Gibson et al. [12] in 1960 use continuous repulsive Born-Mayer interaction potential to simulate the radiation damage in a Cu target and Aneesur Rahman in 1964 [10] use Lennard – Jones potential to describe a system of 864 argon atoms with both attractive and repulsive interactions.

Molecular dynamics is, however, meaningful in its depiction of velocity, changes in atomic position over time. An advantage of molecular dynamics simulations is that systems can be studied with an atomic resolution at short time- and length-scales, down to femtoseconds and angstroms up to nanoseconds and sometimes to microseconds. A very striking advantage in MD simulations is no assumption is made about the processes/mechanism in the system. Based on the experimental conditions, the result of computational simulation may lead to the discovery of new physical mechanisms. Besides, the thermodynamics information of the system describing the driving force for atomic interactions can also be obtained from MD simulation which expresses the energetic relationships between its various possible states.

Molecular dynamics simulation consists of searching for the numerical, step-by-step, solution of the classical equations of motion, which for a simple atomic system may be written as:

$$\vec{F}_i = m_i \vec{a}_i = m_i \frac{d\vec{v}_i}{dt} = m_i \frac{d^2 \vec{r}_i}{dt^2} \quad (\text{E-2.1})$$

Where m_i , \vec{r}_i , \vec{v}_i and \vec{a}_i are the mass, position, velocity and acceleration of atom i in a defined coordinate system, respectively. The force \vec{F}_i acting on each atom i accelerates the particle i , which in turn leads to a new position, velocity, and acceleration. Forces are derived as the negative gradients of the potential energy (interaction potential) U with respect to atomic positions:

$$\vec{F}_i = -\vec{\nabla}_{r_i} U(\vec{r}_1, \vec{r}_2, \vec{r}_3, \dots, \vec{r}_N) \quad (\text{E-2.2})$$

The potential energy, as stated before, can be obtained using either empirical potential energy expressions, semi-empirical methods, or exact *ab initio* approaches. In MD simulations, the calculations of the potential energy and force are the most computer time consuming parts. Once the initial conditions and interaction potential are defined, Equation (E-2.1, E-2.2) can

be integrated to follow the time evolution of the atoms in response to the applied forces. The trajectory of all atoms can be obtained as solutions of Equation (E-2.2), in the form of positions and velocities of all the atoms at each time step. Figure 2.1 shows a flow chart of a basic MD simulation code.

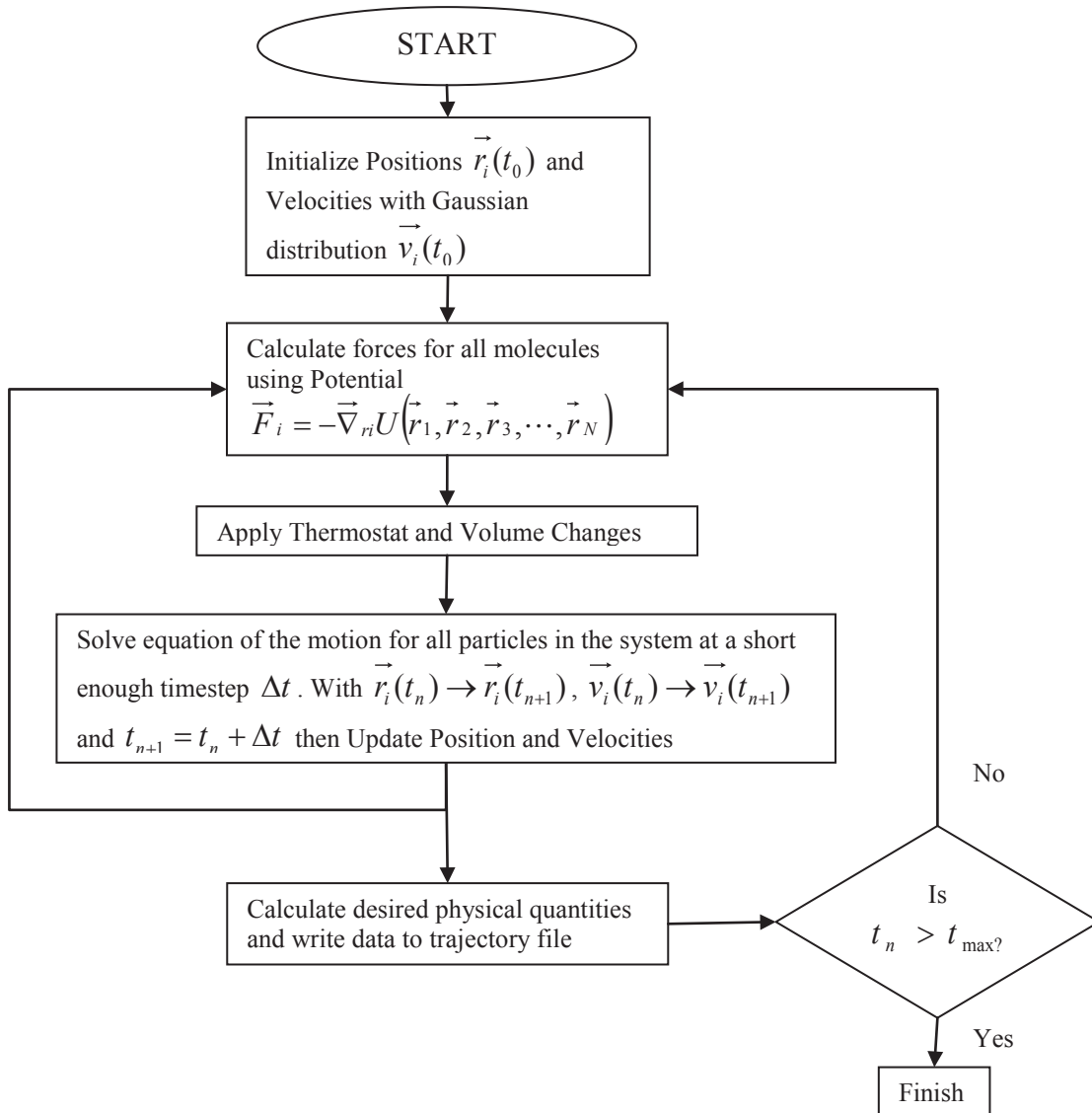


Figure 2.1 – schematic diagram of the basic MD simulation code

2.1.1 The Algorithm of MD simulation

All the integration algorithms assume the positions, velocities and accelerations can be approximated by a Taylor series expansion:

$$r(t + \delta t) = r(t) + v(t)\delta t + \frac{1}{2}a(t)\delta t^2 + \dots \quad (\text{E-2.3})$$

$$v(t + \delta t) = v(t) + a(t)\delta t + \frac{1}{2}b(t)\delta t^2 + \dots \quad (\text{E-2.4})$$

$$a(t + \delta t) = a(t) + b(t)\delta t + \dots \quad (\text{E-2.5})$$

Where r is the position, v is the velocity (the first derivative of r with respect to time), a is the acceleration (the second derivative with respect to time), δt is the integration time step.

To derive the Verlet algorithm one can write

$$r(t + \delta t) = r(t) + v(t)\delta t + \frac{1}{2}a(t)\delta t^2 \quad (\text{E-2.6})$$

$$r(t - \delta t) = r(t) - v(t)\delta t + \frac{1}{2}a(t)\delta t^2 \quad (\text{E-2.7})$$

Summing these two equations, one obtains

$$r(t + \delta t) = 2r(t) - r(t - \delta t) + a(t)\delta t^2 \quad (\text{E-2.8})$$

The Verlet algorithm by Loup Verlet in 1967 [13] is a suitable algorithm complying criteria: the conservation of total energy and momentum, and permitting a long time step, which uses positions and accelerations at time t and the positions from time $t - \delta t$ to calculate new positions at time $t + \delta t$. The Verlet algorithm uses no explicit velocities.

The Leap-frog algorithm

$$r(t + \delta t) = r(t) + v\left(t + \frac{1}{2}\delta t\right)\delta t \quad (\text{E-2.9})$$

$$v\left(t + \frac{1}{2}\delta t\right) = v\left(t - \frac{1}{2}\delta t\right) + a(t)\delta t \quad (\text{E-2.10})$$

In this algorithm, the velocities are first calculated at time $t + 1/2\delta t$; these are used to calculate the positions, r , at time $t + \delta t$. In this way, the velocities *leap* over the positions, and then the

positions *leap* over the velocities. The advantage of this algorithm is that the velocities are explicitly calculated, however, the disadvantage is that they are not calculated at the same time as the positions. The velocities at time t can be approximated by the relationship:

$$v(t) = \frac{1}{2} \left[v\left(t - \frac{1}{2}\delta t\right) + v\left(t + \frac{1}{2}\delta t\right) \right] \quad (\text{E-2.11})$$

The Velocity Verlet algorithm

This algorithm yields positions, velocities and accelerations at time t .

$$r(t + \delta t) = r(t) + v(t)\delta t + \frac{1}{2}a(t)\delta t^2 \quad (\text{E-2.12})$$

$$v(t + \delta t) = v(t) + \frac{1}{2}[a(t) + a(t + \delta t)]\delta t \quad (\text{E-2.13})$$

The schematic of these three different algorithms are shown below:

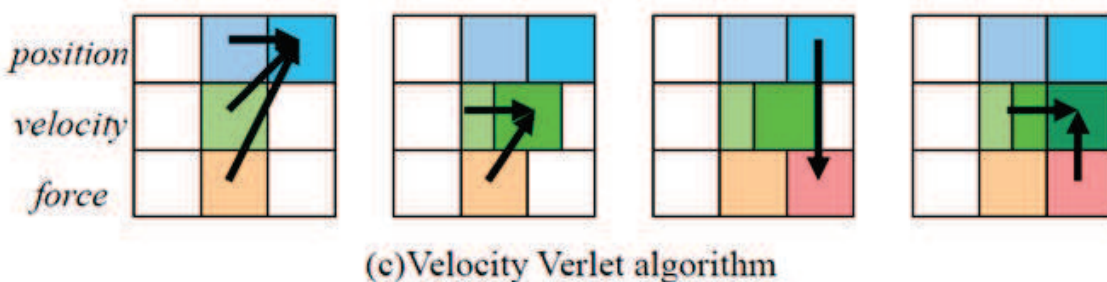
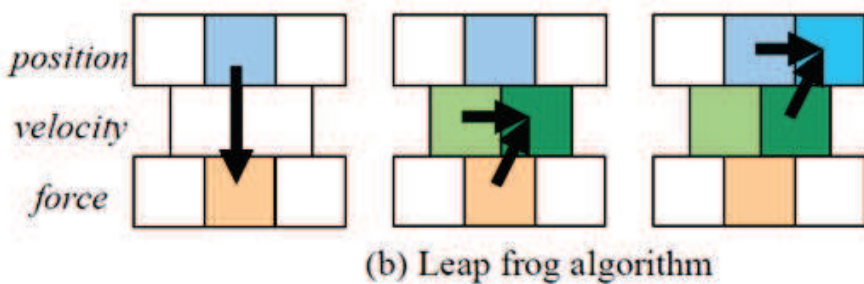
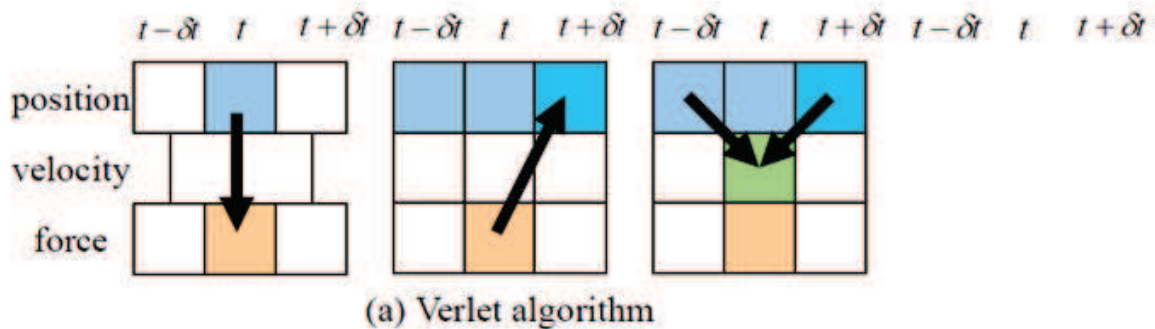


Figure 2.2 – Schematic diagram of the three different Verlet algorithms

2.1.2 Boundary conditions

Molecular dynamics is typically applied to small systems containing limited number of atoms. Thus, the number of atoms in any MD simulation is hard to directly compare to any macroscopic material. Even the simulation of 1 mole of material, containing 6.022×10^{23} atoms, using a simple interatomic potential, would take tens of years or a century. Therefore, a system must be constructed in which the atoms are effectively contained, but nevertheless free of physical walls. This can be accomplished by periodic boundaries, as shown schematically in Fig. 2.3.

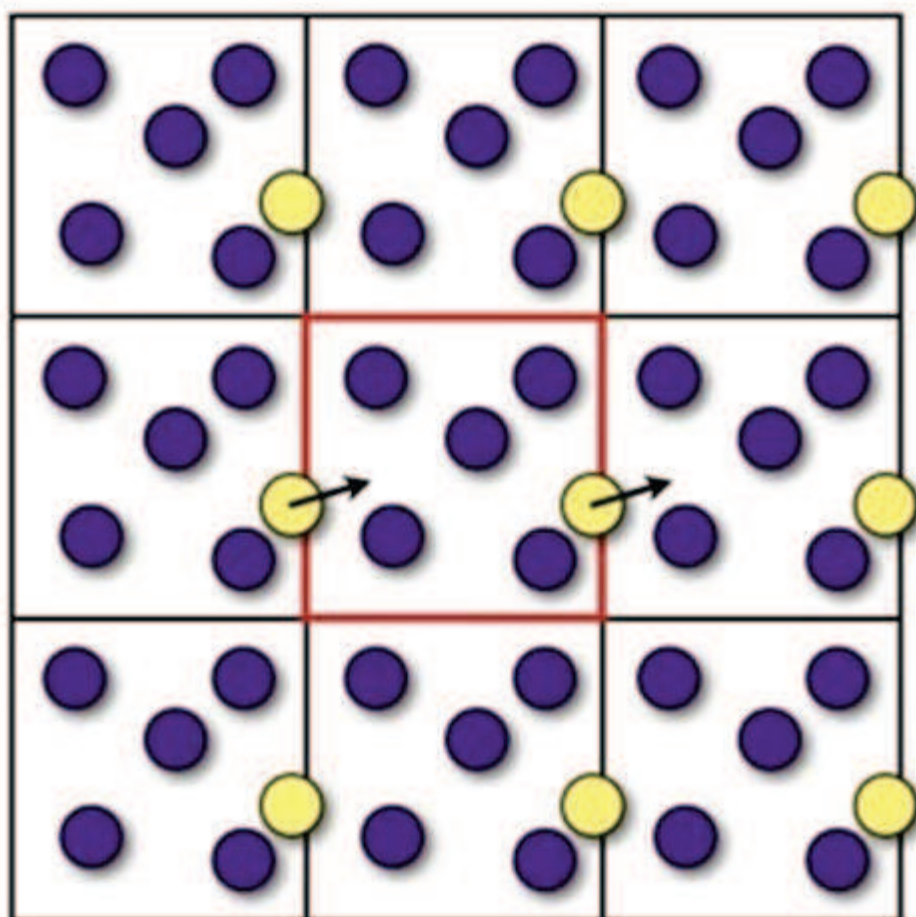


Figure 2.3 - The meaning of periodic boundary conditions.

Atoms are generated and simulated in a volume V which is called the primary cell. The bulk or the surface is assumed to be composed of the primary cell surrounded in 3D or 2D by its exact replicas to model a macroscopic sample. The image cells not only have the same size and shape as the primary one but also contain particles that are images of the particles in the primary cell. Cells are separated by open boundaries so particles can freely enter or leave any cell. When particles leave the cell, their images simultaneously enter the cell through the opposite face.

The atoms will also interact with each other through the periodic boundaries. That is, an atom near the $+x$ boundary, will interact with an atom within a distance smaller than the cut-off of the interatomic potential near the $-x$ boundary, through the $\pm x$ periodic boundary. The atom then interacts with the nearest image of its neighbor. This so-called nearest image criterion is depicted schematically in Fig. 2.4.

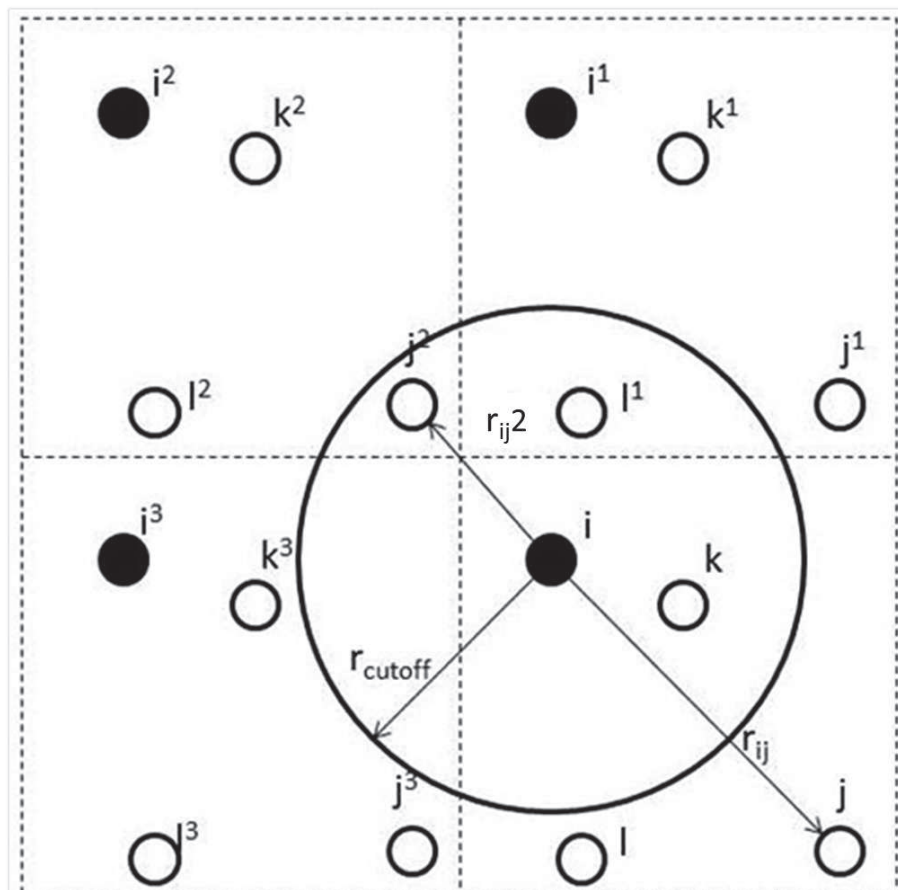


Figure 2.4 - the minimum image criterion

The Figure 2.4 shows the simulation box (in two dimensions), with atoms i , j , k and l . Since periodic boundaries are applied, all atoms have image atoms in the repeated cells. The image atoms are denoted as j^1 - j^3 , k^1 - k^3 and l^1 - l^3 . The minimum image criterion states that the distance between any pair of atoms is the shortest possible distance between them. Consider e.g. the pair of atoms i , j . From the Figure it is clear that the distance r_{ij}^2 is smaller than r_{ij} . Hence, the distance between these atoms is determined to be equal to r_{ij}^2 corresponding to the pair of atoms i , j and not r_{ij} .

For most of the simulations discussed in this thesis, MD simulation of plasma sputter of atoms deposition and film growth focus on the domain of surface in system, so I use periodic boundary condition in x and y directions and free boundary condition in z direction.

2.1.3 The thermostat for controlling temperature

A system of N particles allowed to evolve using Newtonian mechanics will conserve total energy. At equilibrium, the temperature of such a system will fluctuate around an average value. Temperature is calculated from statistical mechanics,

$$\frac{3}{2}NkT = \sum_i \frac{1}{2}m_i v_i^2 \quad (\text{E-2.14})$$

So, if we wish to compute properties of a system at a fixed temperature, we must suppress these fluctuations when making our observation of the system. Further, the deposition or an impact event is highly non-equilibrium in nature, and the temperature of a simulation domain will rise dramatically due to the particle impact, depending on the energy of the incoming particle. Consequently, we are required to control the temperature of the simulation cell in order to mimic natural heat conduction out of the simulation box.

This can be accomplished by changing the atomic velocities according to E-2.14. The temperature can then be controlled by modifying the equations of motion to effectively change the temperature, as well as suppressing the fluctuations in the atomic velocities. There exist several methods for dealing with this problem. Hard thermocoupling scales each particle velocity by the ratio of instantaneous system velocity over specified thermal velocity. Actually, this rather crude method prevents natural temperature fluctuations. One of them, Berendsen thermostat [14], used in this thesis, is implemented by scaling the atomic velocities of the substrate atoms at each time step or interval of time steps by a factor λ :

$$\lambda = \left(1 + \frac{\delta t}{\tau} \left(\frac{T_{\text{set}}}{T} - 1 \right) \right)^{\frac{1}{2}} \quad (\text{E-2.15})$$

Here, δt is the timestep, and τ parameter determines the strength of the coupling. A small τ corresponds to a strong heat bath relative to one with a large τ . Relaxation time values between $10 \delta t$ and $100 \delta t$ are typically used in this thesis, T_{set} is the set point temperature, and T is the temperature of the microscopic state measured using the relation (E -2.15).

2.1.4 Interatomic potentials in the MD simulation

In classical MD simulations, the forces between atoms in the system are derived from a potential energy function; this functional form is often based on a quantum mechanical treatment of the system. The more fundamental quantum mechanical treatment is simplified, by the use of various parameters, the values of which are taken either from first principle calculations or from fits of the model to experimental data. If the latter is used, the potential model is called semi-empirical. If the energy can be calculated by summing up terms, which depend on the atom under consideration and only one of any of its surrounding atoms, this potential is called a pair potential. If the energy, on the other hand, depends on the environment in a more complicated manner, so called many-body potentials must be used.

Lennard-Jones potential

A widely used model to describe the interactions is the Lennard-Jones (LJ) potential. This model is useful for soft-sphere pair potentials and was introduced in 1924 by Lennard-Jones [15]. In the present work, Lennard-Jones potential are used to describe the interactions of the Si-(ZrCu) (Chap 3) and the Cr-(AlCoCuFeNiSi) , Si-(AlCoCrCuFeNi) (Chap 4) [4, 16, 17]

$$V_{ij}(r_{ij}) = 4\varepsilon \left[\left(\frac{\sigma}{r_{ij}} \right)^{12} - \left(\frac{\sigma}{r_{ij}} \right)^6 \right] \quad (\text{E-2.16})$$

The parameters ε and σ of Al, Co, Cr, Cu, Fe, Ni, Zr ,Si LJ potentials are summarized in table 2-1. σ is the distance at which the LJ potential $V_{ij}(\sigma) = 0$ and $-\varepsilon$ is the well depth of the LJ potential.

Table 2-1 LJ potential parameters σ and ε for Al, Co, Cr, Cu, Fe, Ni, Si and Zr

Species	$\varepsilon(\text{eV})$	$\sigma(\text{\AA})$
Al	0.392	2.620
Co	0.516	2.284
Cr	0.502	2.336
Cu	0.409	2.338
Fe	0.527	2.321
Ni	0.520	2.282
Si	0.0175	3.826
Zr	0.739	2.932

While pair potential parameters for the corresponding compound materials are not directly available, the Lorentz-Berthelot mixing rule is used for species i and j , giving: $\varepsilon_{ij} = (\varepsilon_i \varepsilon_j)^{1/2}$ and $\sigma_{ij} = (\sigma_i + \sigma_j)/2$ [4]. More generally, for any kind of potential we can use, in a first approximation, the following general rules: for length terms we consider arithmetic averaging and for energy terms, geometric averaging.

For interactions of platinum atoms with carbon atoms in Chap. 5, we used a Lennard-Jones (LJ) 12 - 6 potential issued from fitting Pt interaction. The force thus becomes:

$$\vec{F}_i(Pt-C) = 24\epsilon_{Pt-C} \sum_j \left\{ 2 \left[\frac{\sigma_{Pt-C}}{r_{ij}} \right]^{12} - \left[\frac{\sigma_{Pt-C}}{r_{ij}} \right]^6 \right\} \frac{\mathbf{r}_{ij}}{r_{ij}^2} \quad (\text{E-2.17})$$

Embedded-atom method (EAM) potential for metals and metal alloys

Such a potential, first introduced by Daw, Baskes and Foiles [18-22], is non-pairwise in the sense that it is based on concepts coming from density functional theory which stipulates, in general that the energy of a solid is a unique function of electron density.

The embedded-atom method uses the idea of electron (charge) density to describe metallic bonding. Essentially, each atom contributes a spherical, exponentially-decaying field of electron charge, centered at its nucleus, to the overall charge density of a system. Binding of atoms is modeled as embedding these atoms in this “pool” of charge, where the energy gained by embedding an atom at location r is some function of local density, $\rho(r)$.

The total EAM energy E of the system can be expressed as:

$$E_{pot} = \sum_{i=1}^N E_i = \frac{1}{2} \sum_{i=1}^N \sum_{j, i \neq j}^N \phi_{ij}(r_{ij}) + \sum_{i=1}^N F_i(\rho_i) \quad (\text{E-2.18})$$

where E_i is the potential energy of an atom i , $\phi(r_{ij})$ is the pair energy term defined as a function of the interatomic distance r_{ij} between atoms i and j , and $F_i(\rho_i)$ is the many body embedding energy term defined as a function of the local electron density, ρ_i , at the position of atom i . The local electron density is calculated as a linear sum of the partial electron density contributions from the neighboring atoms,

$$\rho = \sum_{j, j \neq i}^N f_j(r_{ij}) \quad (\text{E-2.19})$$

Where $f_j(r_{ij})$ is the contribution from atom j to the electron density at the site of the atom i .

The pair energy term is defined as:

$$\phi(r) = \frac{A \exp\left[-\alpha\left(\frac{r}{r_e}-1\right)\right]}{1 + \left(\frac{r}{r_e} - \kappa\right)^{20}} - \frac{B \exp\left[-\beta\left(\frac{r}{r_e}-1\right)\right]}{1 + \left(\frac{r}{r_e} - \lambda\right)^{20}} \quad (\text{E-2.20})$$

Where r_e is the equilibrium spacing between nearest neighbors, A, B, α , and β are four adjustable parameters, and κ and λ are two additional parameters for the cutoff distances. The electron density function is taken with the same form as the attractive term in the pair potential with the same values, for example, the parameter of β , λ .

The electron density function is:

$$f(r) = \frac{f_e \exp\left[-\beta\left(\frac{r}{r_e}-1\right)\right]}{1 + \left(\frac{r}{r_e} - \lambda\right)^{20}} \quad (\text{E-2.21})$$

The pair potential between two different species (a and b) is then constructed as:

$$\phi^{ab}(r) = \frac{1}{2} \left[\frac{f^b(r)}{f^a(r)} \phi^{aa}(r) + \frac{f^a(r)}{f^b(r)} \phi^{bb}(r) \right] \quad (\text{E-2.22})$$

And the embedding energy function is represented by three equations defining it in different electron density ranges and having matching values and slopes at the two junctions,

$$F(\rho) = \sum_{i=0}^3 F_{ni} \left(\frac{\rho}{0.85\rho_e} - 1 \right)^i, \quad \rho < 0.85\rho_e \quad (\text{E-2.23})$$

$$F(\rho) = \sum_{i=0}^3 F_i \left(\frac{\rho}{\rho_e} - 1 \right)^i, \quad 0.85\rho_e \leq \rho < 1.15\rho_e \quad (\text{E-2.24})$$

$$F(\rho) = F_n \left[1 - \eta \ln\left(\frac{\rho}{\rho_s}\right) \right] \left(\frac{\rho}{\rho_s} \right)^\eta, \quad \rho \geq 1.15\rho_e \quad (\text{E-2.25})$$

Table 2-2 All the parameters of EAM potential of Al, Co, Cr, Cu, Fe, Ni, Zr are listed below [6, 23]:

	Al	Co	Cr	Cu	Fe	Ni	Zr
--	----	----	----	----	----	----	----

re (Å)	2,863924	2,505979	2,493879	2,556162	2,481987	2,488746	3,199978
fe (eV/Å)	1,403115	1,975299	1,793835	1,554485	1,885957	2,007018	2,230909
pe (eV/Å)	20,41820	27,20678	17,64130	21,17587	20,04146	27,56201	30,87999
ps (eV/Å)	23,19574	27,20678	19,60545	21,17539	20,04146	27,56203	30,87999
α	6,613165	8,679625	8,604593	8,12762	9,81827	8,383453	8,55919
β	3,527021	4,629134	7,170494	4,334731	5,236411	4,471175	4,564902
A (eV)	0,314873	0,421378	1,551848	0,39662	0,392811	0,429046	0,424667
B (eV)	0,365551	0,640107	1,827556	0,548085	0,646243	0,633531	0,640054
κ	0,379846	0,5	0,18533	0,308782	0,170306	0,443599	0,5
λ	0,759692	1	0,277995	0,756515	0,340613	0,820658	1
Fn0 (eV)	-2,807602	-2,541799	-2,022754	-2,170269	-2,534992	-2,693513	-4,485793
Fn1 (eV)	-0,301435	-0,219415	0,039608	-0,263788	-0,059605	-0,076445	-0,293129
Fn2 (eV)	1,258562	0,733381	-0,183611	1,088878	0,193065	0,241442	0,990148
Fn3 (eV)	-1,247604	-1,589003	-2,245972	-0,817603	-2,282322	-2,375626	-3,202516
F0 (eV)	-2,83	-2,56	-2,02	-2,19	-2,54	-2,7	-4,51
F1 (eV)	0	0	0	0	0	0	0
F2 (eV)	0,622245	0,705845	-0,056517	0,56183	0,200269	0,26539	0,928602
F3 (eV)	-2,488244	-0,68714	0,439144	-2,100595	-0,14877	-0,152856	-0,98187
η	0,785902	0,694608	0,456	0,31049	0,39175	0,44547	0,597133
Fe (eV)	-2,824528	-2,559307	-2,020038	-2,186568	-2,539945	-2,7	-4,509025
ntype	13	27	24	29	26	28	40
Mass (amu)	26,98153	58,9332	51,9961	63,546	55,847	58,6934	91,224

Tersoff potential

The Tersoff potential is a three-body potential functional which explicitly includes an angular contribution of the force [24-27]. Tersoff potential are based on the concept of *bond order*: the strength of a bond between two atoms is not constant, but depends on the local environment. This idea is similar to that of the "glue model" for metals, to use the coordination of an atom as the variable controlling the energy, Tersoff empirical potential is used for describing the interaction between Si-Si in Chap. 3, 4 and C-C in Chap. 5. This potential has been successfully used to investigate the structural, thermal vibration and surface properties of Si and C. The form of Tersoff interatomic potential involving both two- and three-body terms is written as:

$$E = \sum_i E_i = \frac{1}{2} \sum_{i \neq j} V_{ij} \quad (\text{E-2.26})$$

Where V_{ij} is the interaction energy between atoms i and j being a combination of repulsive and attractive terms.

$$V_{ij} = f_C(r_{ij})[f_R(r_{ij}) + b_{ij}f_A(r_{ij})] \quad (\text{E-2.27})$$

$$f_R(r_{ij}) = A_{ij} \exp(-\lambda_1^{i,j} r_{ij}) \quad (\text{E-2.28})$$

$$f_A(r_{ij}) = -B_{ij} \exp(-\lambda_2^{i,j} r_{ij}) \quad (\text{E-2.29})$$

$$f_C(r_{ij}) = \begin{cases} 1, & r_{ij} < R_{ij} \\ \frac{1}{2} + \frac{1}{2} \cos[\pi(r_{ij} - R_{ij})/(S_{ij} - R_{ij})], & R_{ij} < r_{ij} < S_{ij} \\ 0, & r_{ij} > S_{ij} \end{cases} \quad (\text{E-2.30})$$

Here i and j are labels for the atoms. The term with f_R represents a repulsive pair potential, which includes the orthogonalization energy when atomic wave functions overlap and f_A represents an attractive pair potential associated with bonding. The function f_C is merely a smooth cutoff function which limits the range of the potential. The coefficient b_{ij} (bond order) corresponds to a many-body interaction of the form:

$$b_{ij} = \chi_{ij} (1 + \beta_i^{n_i} \xi_{ij}^{n_i})^{-1/2n_i} \quad (\text{E-2.31})$$

with $\xi_{ij}^{n_i} = \sum_{k \neq i, j} f_C(r_{ik}) g(\theta_{ijk})$ characterizing the bond order, with:

$$g(\theta_{ijk}) = 1 + \frac{c_i^2}{d_i^2} - \frac{c_i^2}{d_i^2 + (h_i - \cos \theta_{ijk})^2} \quad (\text{E-2.32})$$

The constants χ_{ij} , β_i , n_i , c_i , d_i and h_i depending on the atomic species and θ_{ijk} is the angle between an ij bond and an ik bond.

The further mixed parameters for a binary system can be defined as:

$$\lambda_1^{i,j} = \frac{1}{2}(\lambda_1^i + \lambda_1^j) \quad (\text{E-2.33})$$

$$\lambda_2^{i,j} = \frac{1}{2}(\lambda_2^i + \lambda_2^j) \quad (\text{E-2.34})$$

$$A_{i,j} = (A_i A_j)^{1/2} \quad (\text{E-2.35})$$

$$B_{i,j} = \chi_{ij} (B_i B_j)^{1/2} \quad (\text{E-2.36})$$

$$R_{i,j} = (R_i R_j)^{1/2} \quad (\text{E-2.37})$$

$$S_{i,j} = (S_i S_j)^{1/2} \quad (\text{E-2.38})$$

Table 2.3 – Tersoff potential parameters

	C	Si
A(eV)	1.3936×10^3	1.8308×10^3
B(eV)	3.4674×10^2	4.7118×10^2
$\lambda(\text{\AA}^{-1})$	3.4879	2.4799
$\mu(\text{\AA}^{-1})$	2.2119	1.7322
β	1.5724×10^{-7}	1.1000×10^{-6}
n	7.2751×10^{-1}	7.8734×10^{-1}
c	3.8049×10^4	1.0039×10^5
d	4.3484	1.6217×10^1
h	-5.7058×10^{-1}	-5.9825×10^{-1}
R(\AA)	1.8	2.7
S(\AA)	2.1	3.0

There exist other potential functions for describing C and Si (REBO, ReaxFF). Nevertheless, these ones are relevant for pure C and Si and in a first attempt; there is no need for using more sophisticated functions.

2.2 The setup model in plasma environment

2.2.1 Plasma environment in MD simulations

Considering plasma sputter deposition, particles sputtered from solid targets, will lose energy and slowdown in collisions with the gas phase, typically argon. We use a simple model of particle slowing down along straight-line trajectories, subject to a continuous energy loss process, which allows calculating the energy distributions of the particle flux as a function of

the distance to the source.

Here, we do not inject Ar ions into the system representing a plasma environment. The mean kinetic energy of incoming atoms are calculated according to the modification of Thompson formula considering the effect of travelling through a gaseous medium [28]:

$$f(E) \propto \frac{1 - \left(\frac{E_{coh} + E}{\gamma E_{Ar^+}} \right)^{\frac{1}{2}}}{E^2 \left(1 + \frac{E_{coh}}{E} \right)^3} \quad (E-2.39)$$

$$E_F = (E - k_B T_g) \exp[n \ln(E_f / E_i)] + k_B T_g \quad (E-2.40)$$

$E_f/E_i = 1-\gamma/2$ is the ratio of energies after and before a collision, [29] where $\gamma = 4 \frac{m_g m_s}{(m_g + m_s)^2}$

where m_g and m_s stand for gas atom (Argon here) and sputtered atom (Zr or Cu here) masses respectively, and $n = dp\tau/k_B T_g$. E is the energy of the sputtered particles as they leave the target, T_g is the sputtering gas temperature, n is the number of collisions that take place in the gas, d is the traveled distance, p is the sputtering gas pressure, and τ is the collision cross section assuming hard core interactions. To calculate the energy loss (E_f) of sputtered atoms with the gas atoms, a Maxwell-Boltzmann (MB) distribution at T_g is fixed for the gas (in our conditions $T_g = 300$ K). Because we search for the complete distribution of sputtered atoms, we replace $k_B T_g$ by E_g , a particular value in the gas distribution. Thus for each E_g in the MB gas distribution, the energy loss is calculated for a fixed value of the kinetic energy E of a sputtered atom. This is repeated for each E in the Thompson distribution and weighted by the collision probability, which is simply the product of $f(E)$ and the MB distribution at T_g . [28]. The velocities of the sputtered atoms are sampled from a Maxwell-Gaussian distribution with the mean kinetic energy 1 eV with randomly selected incident angles. This occurs for

sputtering experiments at Ar pressure around 1 Pa and target to substrate distance around 9 cm.

2.2.2 The MD model for deposition

In this thesis, 3 different systems are studied via MD simulation: the growth of Zr_xCu_{100-x} metallic alloy, AlCoCrCuFeNi high entropy alloy (HEA) and platinum atom deposition on nanostructured carbon substrates. All of these are performed with the same atom deposition method. Here, we use the system of ZrCu as an example to introduce the MD model of plasma sputtered atom deposition..

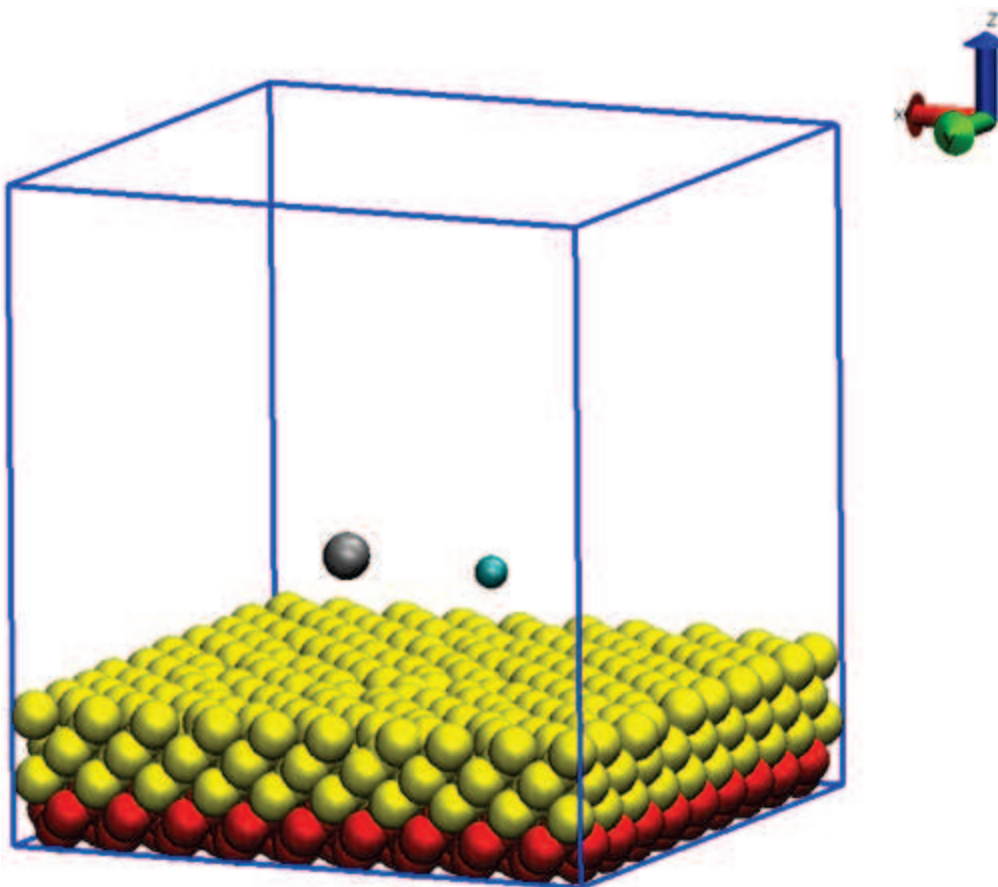


Figure 2.5 - Schematic picture of the deposition model. ● Zr, ● Cu, ● moving Si, ● fixed Si

MD simulations are carried out in a three dimensional cell, which is periodic only along x and y directions (see Figure 2.5). The size of the cell varies among the simulation discussed hereafter. The deposited atoms with the different ratios (detailed in the following chapters) are randomly released towards the substrate every 2ps. Each atom is placed in the vacuum slab at a random position from 5 to 7 Å above the surface. For the substrate, the first two bottom layers of the substrate are fixed (red atoms in Figure 2.5), while the other layers are temperature-controlled layers using a Berendsen thermostat [14]. In any thin-film growth experiment, heating of the substrate occurs by the depositing atoms. The thermal conductivity of the substrate allows its heat to be transported into the bulk of the substrate material. In our simulation we model this thermal-conduction process by monitoring the average temperature of N_1 substrate layers every m steps, m conveniently chosen to be 10 ~ 100. If the substrate temperature exceeds the desired temperature T_s , here 300K, the atoms velocity in the N_1 layers are rescaled to maintain a constant T_s with Berendsen thermostat. Details on simulation cells used in each study are given in the individual chapters.

We should notice that the incoming atom fluxes are unphysically large in MD simulation typically $0.5 \text{ at.nm}^{-2}.\text{ps}^{-1}$ while it is $10 \text{ at. nm}^{-2}.\text{s}^{-1}$ in sputtering experiments. So deposition rates are not accessible. But using an appropriate thermostat relaxation time consistent with the energy dissipation time scale in the experiments can lead to correct structure and morphologies of the growing thin films. This also requires that long time diffusion is not present in the simulation. The systems examined here are not known to exhibit long range/time diffusion.

The LAMMPS MD package [10] is used to simulate the deposition atoms. The whole depositing process is divided into several periods. During each of period (20 ps), 10 atoms are released freely from top the substrate. The high energy of the deposited atoms can be

dissipated on the surface of substrate with Berendsen thermostat in the course of simulation to keep the whole temperature around 300K (room temperature) corresponding to the value in the experiment. A BASH shell script driving the LAMMPS code was written for automating the deposition of the system until the desired atoms are deposited ($N_{atom_{max}}$). This is shown in the schematic diagram in Figure 2.6.

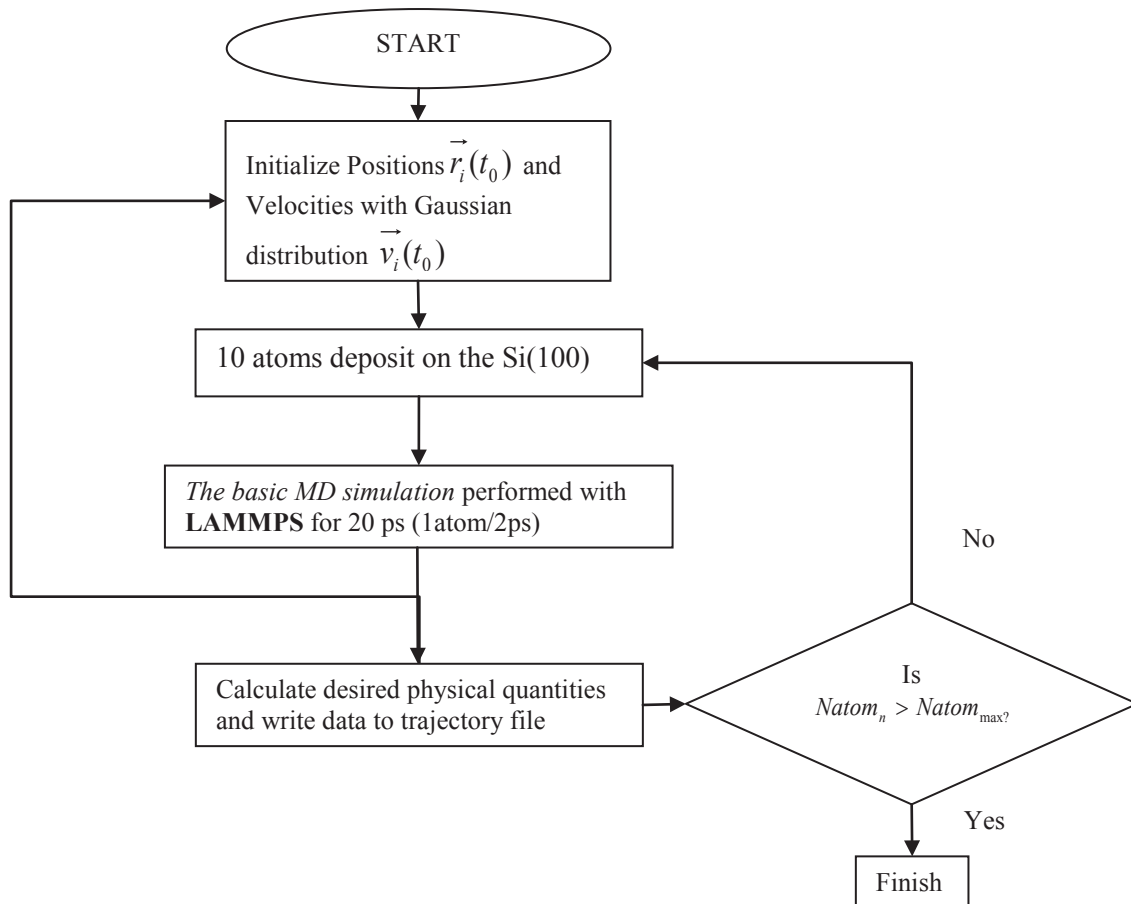


Figure 2.6 – Schematic diagram of atom deposition model

2.3 The analysis method

Radial distribution function

In statistical mechanics, the radial distribution function (RDF), also called pair correlation function, $g(r)$ of a system of particles (atoms, molecules, colloids, etc.), describes how particle density varies as a function of distance from a reference particle. It gives a measure of the

probability that, given the presence of an atom at the origin of an arbitrary reference frame, there will be an atom with its center located in a spherical shell of infinitesimal thickness at a distance, r , from the reference atom.

The RDF can be expressed as:

$$\mathbf{g}(\mathbf{r}) = \frac{\mathbf{n}(\mathbf{r})}{\rho \cdot 4\pi r^2 \Delta r} \quad (\text{E-2.41})$$

Where $g(r)$ is the RDF, $n(r)$ is the mean number of atoms in a shell of width Δr at distance r , i.e. at a distance between r and $r + \Delta r$, ρ being the mean atom density.

The pair correlation function was used in structural investigations of both solid and liquid packing (local structure), in studying specific interactions such as hydrogen bonding, in statistical mechanical theories of liquids and mixtures.

Simulation of X-ray diffraction patterns

In this work, the simulation of X-Ray diffraction (XRD) is also carried out to analyze the crystal phases for direct comparison with available experimental data. In most radiation scattering experiments, the objective is to obtain information that characterizes either intramolecular or intermolecular structure. In such cases, variation of the scattered intensity with angle is the quantity of main interest, whereas the absolute intensity is not necessarily of concern. Thus, ignoring all intensity scale factors and correction factors appropriate for the geometry of the scattering apparatus, the amplitude and intensity of radiation scattered coherently from an arbitrary set of n atoms may be written as:

$$F(\mathbf{Q}) = \sum_{j=1}^n f_j \exp(\mathbf{Q} \cdot \mathbf{r}_j) \quad (\text{E-2.42})$$

$$I(\mathbf{Q}) = F(\mathbf{Q}) * F(\mathbf{Q}) = \sum_{j=1}^n \sum_{k=1}^n f_j f_k \cos(\mathbf{iQ} \cdot \mathbf{r}_{jk}) \quad (\text{E-2.43})$$

$$Q = \frac{2\pi}{d} = \frac{4\pi \sin \theta}{\lambda} \quad (\text{E-2.44})$$

$$f_i = \int \rho_i \mathbf{r} \exp(-2\pi i \mathbf{Q} \cdot \mathbf{r}) d^3 \mathbf{r} \quad (\text{E-2.45})$$

Where ρ is the density of atom i , \mathbf{r} is the position vector, i is the complex unit and \mathbf{Q} is the scattering vector (Bragg's Law), f is the atomic scattering factor for the radiation used, and \mathbf{r}_{jk} denotes the vector connecting atoms j and k . λ is x-ray wavelength, chosen to be 1.542 Å as in the experiments.

Solid-solution formation rules

According to Zhang Y. et al [30], two parameters can be used to characterize the collective behavior of the constituent elements in the multi-component (more than 4 elements) alloys: δ , describing the comprehensive effect of the atomic-size difference in the n -element alloy and Ω , parameter considering the effect of ΔH_{mix} (enthalpy of mixing) and ΔS_{mix} (entropy of mixing). By calculating parameters δ and Ω for multi-component alloys, a solid-solution formation rule has been proposed.

Figure 2.7 taken from [30] shows the relationship between parameters δ and Ω for multi-component alloys. “Solid Solutions” indicates that the alloy only contains solid solution; “Intermetallics” indicates the alloy mainly contains intermetallic compounds and other ordered phases; “S + I” indicates that not only the solid solution could form, but also the ordered compounds could precipitate; and “BMGs” indicates the alloy can form amorphous phases.

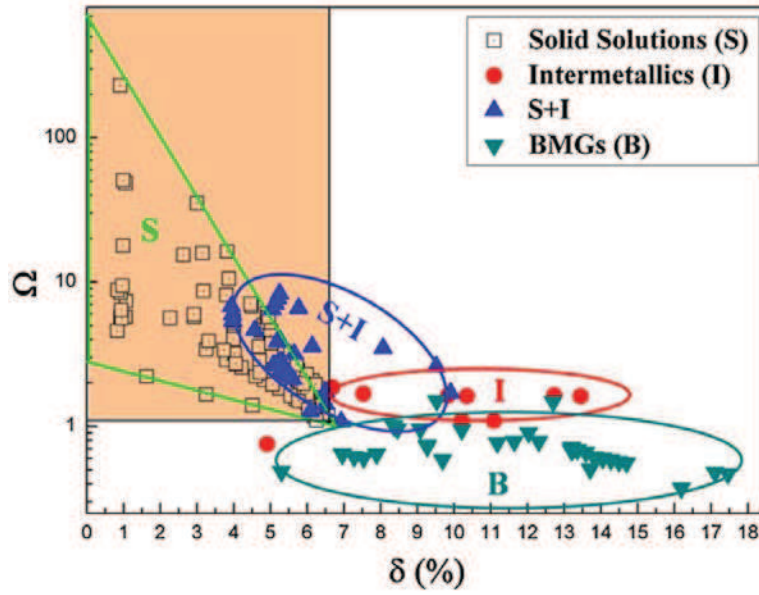


Figure 2.7 - The relationship between parameters δ and Ω for multi-component alloys [30]

Both parameters were defined in Eqs. (2.48-2.49), respectively

$$\Delta H_{mix} = \sum_{i=1, i \neq j}^n \Omega_{ij} c_i c_j \quad (\text{E-2.46})$$

$$\Delta S_{mix} = -R \sum_{i=1}^n (c_i \ln c_i) \quad (\text{E-2.47})$$

Where $\Omega_{ij} = 4\Delta H_{AB}^{mix}$ is the regular solution interaction parameter between the i th and j th elements, c_i or c_j is the atomic percentage of the i th or j th component, and ΔH_{AB}^{mix} is the enthalpy of mixing of binary liquid alloys presented in table 2.4 [31], R ($=8.314\text{JK}^{-1}\text{mol}^{-1}$) is the gas constant.

Table 2.4 - value of ΔH_{AB}^{mix} (kJ/mol) calculated by Miedema's model for atomic pairs between elements with Al, Co, Cr, Cu, Fe, Ni and Zr [31]

Element	Al	Co	Cr	Cu	Fe	Ni	Zr
Al	-	-19	-10	-1	-11	-22	-44
Co	-19	-	-4	6	-1	0	-41
Cr	-10	-4	-	12	-1	-7	-12
Cu	-1	6	12	-	13	4	-23

Fe	-11	-1	-1	13	-	-2	-25
Ni	-22	0	-7	4	-2	-	-49
Zr	-44	-41	-12	-23	-25	-49	-

$$\Omega = \frac{T_m \Delta S_{mix}}{|\Delta H_{mix}|} \quad (E-2.48)$$

$$\delta = \sqrt{\sum_{i=1}^n c_i (1 - r_i / \bar{r})^2} \quad (E-2.49)$$

Where c_i is the atomic percentage of the i th component and $\bar{r} = \sum_{i=1}^n c_i r_i$ is the average atomic radius and r_i is the atomic radius shown in table 2.5 [32] .

Table 2.5 Radius (Å) for the elements of Al, Co, Cr, Cu, Fe, Ni and Zr

Elements	Al	Co	Cr	Cu	Fe	Ni	Zr
Radius (Å)	1.43	1.25	1.3	1.28	1.26	1.24	1.6

$$T_m = \sum_{i=1}^n c_i (T_m)_i \quad (E-2.50)$$

T_m is the average melting temperature of n-elements alloy and $(T_m)_i$ is the melting point of the i^{th} component of the alloy. This is only valid for systems with more than 4 elements (see ref. 30).

Chapter 3: Molecular dynamics simulation of Zr_xCu_{100-x} thin film growth

Récemment, il y a eu un énorme intérêt pour l'étude de la structure atomique et de la relation structure-propriété des verres métalliques (MSG). Ces matériaux ont été étudiés depuis 40 ans en raison de leurs propriétés prometteuses à la fois de métaux (conductivité électronique et thermique, la ductilité ...) et de verres (dureté ...). Pour stabiliser une phase amorphe dans les alliages métalliques, la diffusion atomique doit être évitée. Cela peut se contrôler en jouant sur la composition chimique (mélange d'éléments de différentes tailles atomiques) ou par trempe pendant le procédé de synthèse [3]. Il a été démontré que le dépôt de couches minces par condensation sur des substrats à froid permet de stabiliser des structures faiblement ordonnées de ces systèmes.

À titre d'exemple, les alliages ZrCu ont suscité beaucoup d'intérêt au cours des dernières années, en raison de leurs propriétés de verre métallique à l'état massif, et pour leur propriétés mécaniques de films d'alliage amorphe et la supraconductivité propriétés. Par exemple Dudonis et al. A préparé des couches minces avec la composition dans la gamme de ($5 \leq x \leq 95$) et dont les propriétés dépendent des conditions de sythèse par pulvérisation cathodique magnétron.

Les couches minces Zr_xCu_{100-x} produites par magnétron ont été étudiées par simulations de dynamique moléculaire utilisant des conditions initiales similaires à celles d'investigations expérimentales. La cristallinité des films a été analysée par RDFs et XRD calculées. Les résultats montrent que les films contenant une grande quantité d'un des deux éléments (proportion supérieure à 80%) sont cristallisés, alors que pour les compositions intermédiaires une phase faible ordonnée est mise en évidence. Cette tendance est due au désordre chimique, puisque les deux atomes semblent être incorporés dans le même réseau (solution solide) qui induit une distorsion du paramètre de maille. La valeur de ce dernier s'avère être comprise entre celui des deux métaux purs. Les résultats des simulations de dynamique moléculaire ont été comparés avec les analyses DRX des films minces déposés expérimentalement. Les résultats expérimentaux montrent aussi des changements de structure cristalline à une teneur élevée ou faible en Zr et amorphe pour des compositions intermédiaires de Zr, allant de 20 à 75%.

Les résultats montrent également que la morphologie des films est fortement corrélée avec l'énergie cinétique moyenne des atomes incidents. A énergie cinétique plus élevée, un film compact et homogène. Avec une énergie inférieure, la morphologie est en agrégats ou en film selon la composition atomique. Il se forme également, dans certains cas, des macles.

3.1 Introduction

Recently, there has been a huge interest in the atomic-level structure and structure-property relationship in metallic glasses (MGs). These materials have been studied for 40 years because of their promising properties belonging to both metals (electron, heat conductivity, ductility...) and glasses (hardness...) [33, 34]. To stabilize an amorphous phase in metallic alloys, atomic diffusion must be prevented. This could be achieved by playing with the chemical composition (mixing of elements with different atomic sizes) or by freezing a low ordered phase during the synthesis process [35]. It has been shown that deposition of thin

films by condensation onto cold substrates allows stabilizing low ordered structure in such systems.

As an example, ZrCu alloys have attracted interest in recent years, due to their bulk metallic glass properties [36-40], and as amorphous alloy films for their mechanical [41-43] and superconductivity properties [44]. For example Dudonis et al. [45] prepared thin films with composition in the range of ($5 \leq x \leq 95$) by using high working power (490 W and 1380 W on Cu and Zr targets, respectively) during magnetron sputter deposition.

Numerous theoretical studies have also been conducted on ZrCu systems. Sha et al. [46, 47] employed atomistic methods for studying ZrCu MGs forming conditions. Almyras et al. investigated the microstructure of $Zr_{35}Cu_{65}$ and $Zr_{65}Cu_{35}$ MGs and found that these systems consist of small touching and/or interpenetrating icosahedral-like clusters which results in “supercluster” (SCs) satisfying the system composition [48]. They thus claimed that seeking the equilibrium configuration for interpenetrating ICO-like clusters allows the prediction of the MG microstructure. While bulk amorphous structure is known to be formed under specific synthesis conditions, the growth of ZrCu amorphous thin film has not been so much studied. A better understanding of thin film growth can be achieved via simulations and compared to available experimental data as X-ray diffraction patterns.

In this chapter we report on results of MD simulations and on a structural study of Zr_xCu_{100-x} metal alloy thin films grown by magnetron plasma sputter deposition. Evolutions of morphology and structure of the thin film in function of the composition and the depositing atom kinetic energies were investigated. A specific focus on comparisons with selected available experimental data is highlighted.

3.2 Experimental part

The Zr_xCu_{100-x} alloy films were prepared by DC magnetron sputter deposition in Ar atmosphere at room temperature. Two targets, pure Cu (purity, 99.999%) and pure Zr (purity, 99.999%), were used at the same time for co-deposition of the alloy films.

In this chapter three different experimental conditions of plasma sputter deposition are simulated, involving a more detailed composition analysis. This is intended for determining the role of both the composition and the deposited atom kinetic energy on the formation of the amorphous phase.

The first simulation corresponds to conditions that the pressure in the chamber is at 0.25 Pa, the distance between the target and the substrate was set to 9 cm and target bias of both targets of 300 V. The second experiment is according to Dudonis et al [45] with the same deposition method, the pressure was 0.03 Pa, the distance between the target and the substrate was set to 7 cm and the target biases was 460 V on Zr cathode and 490 V on Cu cathode. The third experiment was also built from Dudonis et al but with a larger pressure 3 Pa [45].

By altering the sputtering power of both targets, Zr_xCu_{100-x} thin films with different compositions were synthesized on Si (100) wafers. Typical deposited thickness was 600 nm. In order to study the structure of the Zr_xCu_{100-x} metallic films, X-ray diffraction analysis (Cu K_α radiation, $\lambda = 0.15405$ nm, Breg-Brentano geometry) was performed. Microstructure of the deposits was observed on SEM images (Carl Zeiss-Supra40- FEG-SEM)

3.3 MD Model configuration

In the experiment of plasma sputter deposition, particles sputtered from solid targets under typical vacuum conditions, will lose energy and slow down by collisions with the gas phase. We use a simple model of particle slowing down along straight-line trajectories, subject to a continuous energy loss process, which allows calculating the energy distributions of the non-thermalized component of the particle flux as a function of the distance to the source [28, 29]. Here, we use the modified Thompson formula (detailed in Chap 2.) to calculate the mean kinetic energy of the incoming Zr and Cu atoms shown in table 3.1.

Table 3.1 - the mean kinetic energy of incoming atoms in three different conditions.

Experiment	Zr (eV)	Cu (eV)	Experiment Condition
1	7.65	6.67	$d_{T-S} = 9$ cm, $P = 0.25$ Pa, Target bias = 300 V
2	12.6	9.61	$d_{T-S} = 7$ cm, $P = 0.03$ Pa, Target bias (Zr) = 460 V, Target bias (Cu) = 490 V
3	0.13	0.34	$d_{T-S} = 7$ cm, $P = 3$ Pa, Target bias (Zr) = 460 V, Target bias (Cu) = 490 V

The deposition model is described in section 2.2 where the setup model of atom deposition takes Zr_xCu_{100-x} as an example.

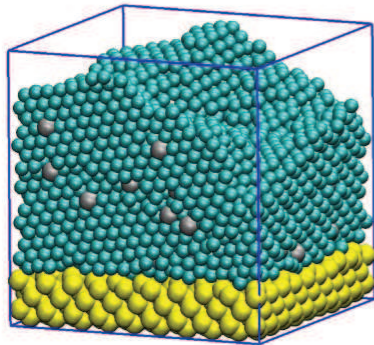
3.4 Result and discussion

3.4.1 Zr_xCu_{100-x} ($3 \leq x \leq 95$) thin films deposited on a silicon (100) substrate: effect of the chemical composition

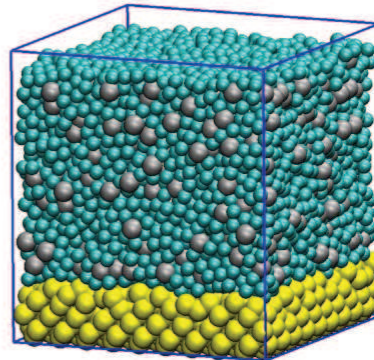
In this subdivision, we employed classical molecular dynamics simulations model to study Zr_xCu_{100-x} ($3 \leq x \leq 95$) metallic glass films deposited on a silicon (1 0 0) substrate. Input data were chosen to fit with the first experimental operating conditions of a magnetron sputtering deposition system.

The films grew to approximately 5 ~ 7.5 nm thickness. Snapshots of the deposited layers on the Si(100) substrate are presented in figure 3.1. The film composition was found to be close to that of the vapor composition, which in turn means that sticking coefficients are close to each other. Because of the larger radius of Zr atoms, the thickness of the deposited films varies depending on the Zr/Cu ratio. For example, Zr_3Cu_{97} exhibits a thickness around 5 nm, whereas $Zr_{95}Cu_5$ is 7.5 nm thick.

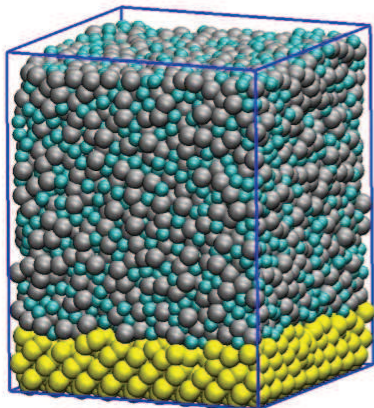
Zr₃Cu₉₇ (280/8617 at.)



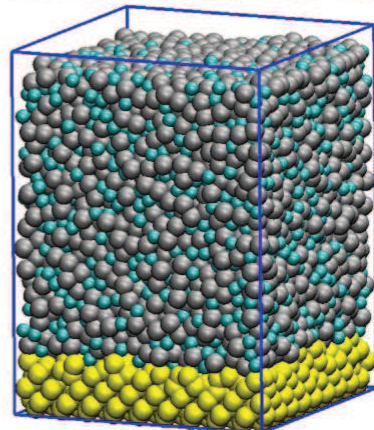
Zr₂₀Cu₈₀ (1769/7174 at.)



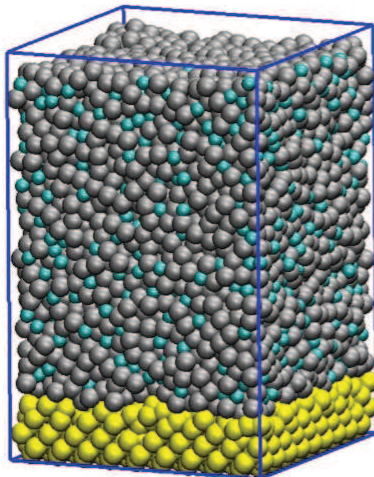
Zr₄₆Cu₅₄ (4180/4955 at.)



Zr₅₅Cu₄₅ (5102/4089 at.)



Zr₇₃Cu₂₇ (6733/2523 at.)



Zr₉₅Cu₅ (8864/437 at.)

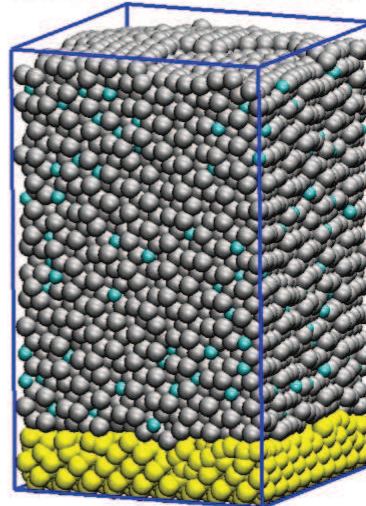


Figure 3.1 - Snapshots of Zr-Cu coatings deposited on Si(100) substrate at different ratios of Zr and Cu atoms (the numbers in brackets are the Zr and Cu atom numbers respectively). Zr, ●Cu, ●Si

In this set of simulations, RDFs for the system Zr_xCu_{100-x} was also calculated for each case. The all-all, Zr-Zr and Cu-Cu RDFs at 3%, 20%, 46%, 55%, 73% and 95% Zr metal contents are presented in figures 3.2-3.4 respectively.

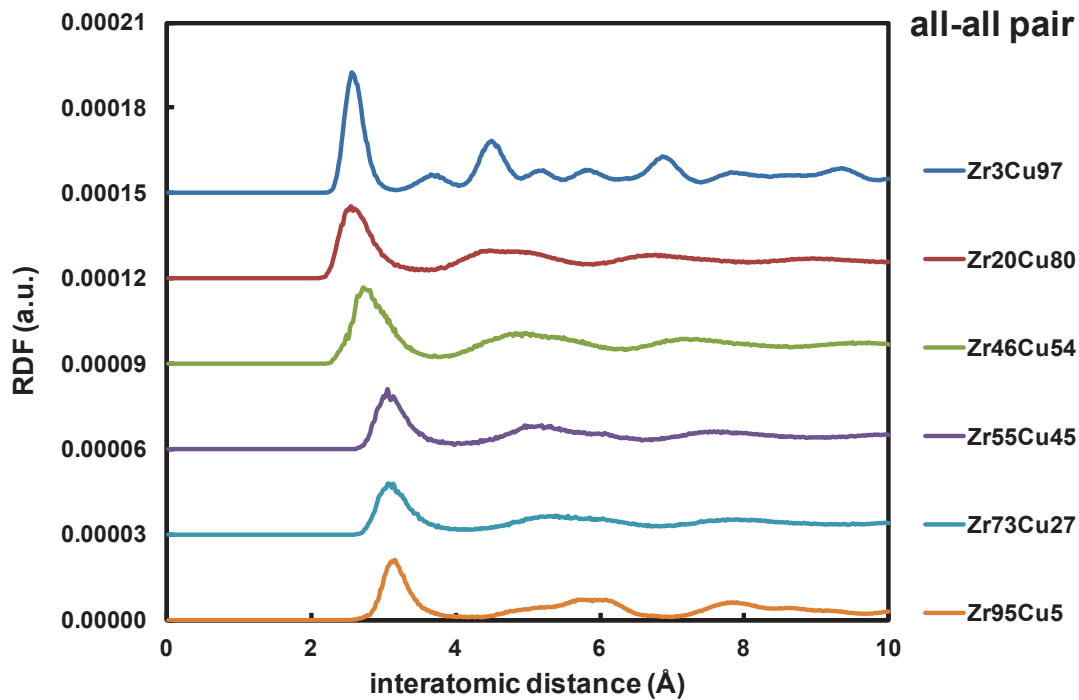


Figure 3.2 - Total RDFs for Zr_xCu_{100-x} alloys, individual curves corresponding to different alloy compositions are displaced vertically for clarity.

At low or high concentrations of Zr, i.e. Zr_3Cu_{97} or $Zr_{95}Cu_5$, the calculated RDFs show outstanding peaks which can be assumed as crystalline structure of Cu and Zr, separately. Indeed, the intensity and position of the peaks are very similar to those of Cu and Zr crystals (table 3.1). The ordered structure are also evidenced on the snapshots of the films at the corresponding Zr concentrations presented in figure 3.1 where the cross-sections of Zr_3Cu_{97} and $Zr_{95}Cu_5$ exhibit well crystallized structure. On the contrary, for the Zr contents between 3% and 95%, an amorphous structure with a well-defined first peak and a split second peak in the RDFs pattern, are shown in figure 3.2. The higher-order peaks, however, fade away quickly. This is representative of the disorder in amorphous state, and shall be taken as the reference for other simulations. This is also agreeing with the visual observation in figures 3.1 (from

Zr₂₀Cu₈₀ to Zr₇₃Cu₂₇). Besides, the RDF of the system exhibits a distinct first peak indicating that there exists a strong short-range order (SRO). We also observe that the first peak shifts toward larger radial distance values when increasing Zr concentrations. This was expected since the Zr-Zr first neighbor distance is larger than for Cu (see table 3.2).

Table 3.2- The four nearest neighbor distances in Zr and Cu bulk crystals, lattice constants for Zr and Cu are respectively $a_{Zr} = 3.23 \text{ \AA}$, $c_{Zr} = 5.15 \text{ \AA}$ and $a_{Cu} = 3.61 \text{ \AA}$.

Crystal name	Structure	First neighbor (Å)	Second neighbor (Å)	Third neighbor (Å)	Fourth neighbor (Å)
Zr	hcp	$a_{Zr} = 3.23$	$\sqrt{2} a_{Zr} = 4.53$	$c_{Zr} = 5.15$	$\sqrt{2} c_{Zr} = 5.57$
Cu	fcc	$\frac{a_{Cu}}{\sqrt{2}} = 2.55$	$a_{Cu} = 3.61$	$\sqrt{\frac{3}{2}} a_{Cu} = 4.42$	$\sqrt{2} a_{Cu} = 5.10$

As illustrated in figure 3.2, like bonds exhibit strong sensitivity to atomic concentrations. For example, in Zr-Zr RDFs, at low Zr concentration (Zr₃Cu₉₇), no specific feature is observed showing Zr atoms are well randomly dispersed in Cu background, without correlations. This is confirmed when looking at the corresponding snapshots. When the Zr concentration increases, the third and fourth peak slowly appears and become “higher and narrower” indicating the Zr-Zr’s phase changing from amorphous state to crystalline. On the contrary, the Cu-Cu RDF shows a stronger SRO in the Cu-rich film and a progressive change from crystal to amorphous when the % of Cu decreases. In summary, the RDFs show that an amorphous structure of the films is formed in a wide composition range i.e. when $20 \leq x \leq 73$.

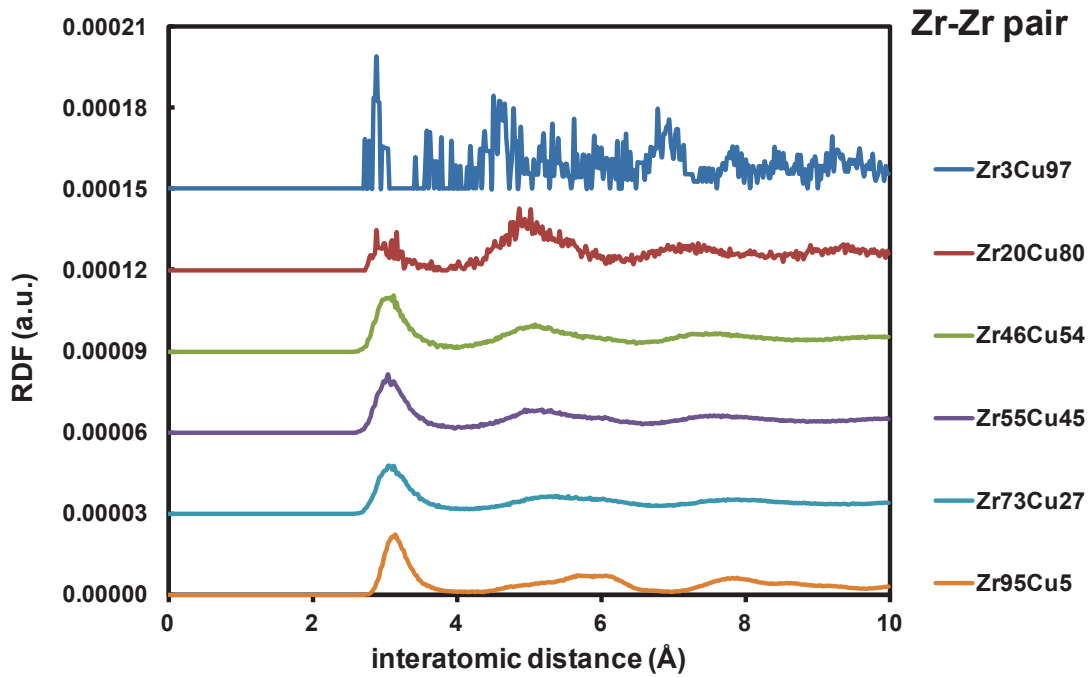


Figure 3.3- RDFs for Zr-Zr for Zr_xCu_{100-x} alloys, individual curves corresponding to different alloys are displaced vertically for clarity.

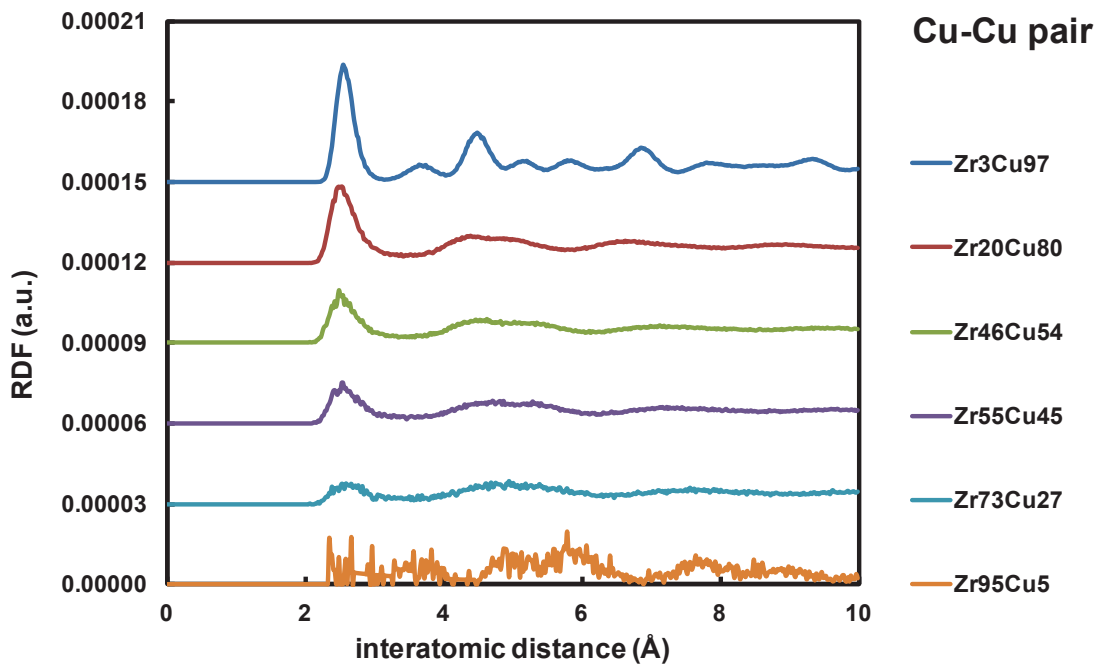


Figure 3.4 - RDFs for Cu-Cu for Zr_xCu_{100-x} alloys, individual curves corresponding to different alloys are displaced vertically for clarity.

For comparison with simulations, figure 3.5 shows the intensity and position of the XRD θ - 2θ peaks as a function of the Zr metal content. At the Zr concentration of 3% and 95%, Zr_xCu_{100-x}

x films are crystalline which agrees with the present RDF calculations. As the Zr concentration increases from 20% to 73%, a shift of the peak towards small angles ($2\theta = 41.8^\circ, 38.7^\circ, 37.4^\circ,$ and 35.9°) is observed. Meanwhile, all of these patterns consist of a broad halo peak, indicating a low ordered structure. It seems that Zr and Cu atoms are inserted in the main element matrix and form a solid solution. Distortion of the lattice parameter due to the different atomic size leads to a lowering of the crystallinity.

Three of the experimentally deposited films, i.e. at 3%, 72% and 95% Zr metal content, were observed by SEM. The corresponding images of the films (surface and cross-section) are presented in figures 3.7(a)-(c), respectively. The films at 3% Zr and 95% (figure 3.7(a), (b), (e), (f)) exhibit grains of about 50 nm and columnar structure is visible on the cross-section micrographs. On the contrary $Zr_{73}Cu_{27}$ film (figure (c), (d)) seems relatively dense and featureless, which could correspond to an amorphous structure. SEM observations are thus in agreement with XRD results.

The calculated X-ray intensities vs. 2θ of Zr_xCu_{100-x} simulated films are shown in figure 3.6. Ignoring all intensity scale factors and correction factors related to the geometry of the scattering apparatus, they can be compared to the experiment patterns. It can be observed in table 3.3 that the peak positions in the simulated XRD are close to that detected in the experimental XRD patterns. Even for “crystalline” conditions the peaks are broader due to the finite size of the simulations. The shift also evidenced between experimental and simulated positions is certainly due to the same effect, and possibly to some layer strain in the experimental films. The peak intensities are very different between simulations and experiments. This is due to the difference in layer thickness, thus in the total atom number. At this stage, the comparison can only be qualitative.

Table 3.3 - the 2θ -position of the main XRD peak for ZrCu alloys in the experiment and the simulation

Experiment							Unit: $2\theta(^{\circ})$
Zr-Cu	Zr ₃ Cu ₉₇	Zr ₂₀ Cu ₈₀	Zr ₄₆ Cu ₅₄	Zr ₅₅ Cu ₄₅	Zr ₇₃ Cu ₂₇	Zr ₉₅ Cu ₅	
main peak	43.2	41.8	38.7	37.4	35.9	34.5	

Simulation							Unit: $2\theta(^{\circ})$
Zr-Cu	Zr ₃ Cu ₉₇	Zr ₂₀ Cu ₈₀	Zr ₄₆ Cu ₅₄	Zr ₅₅ Cu ₄₅	Zr ₇₃ Cu ₂₇	Zr ₉₅ Cu ₅	
main peak	42.2	41.7	38.65	37.7	36.1	35.55	

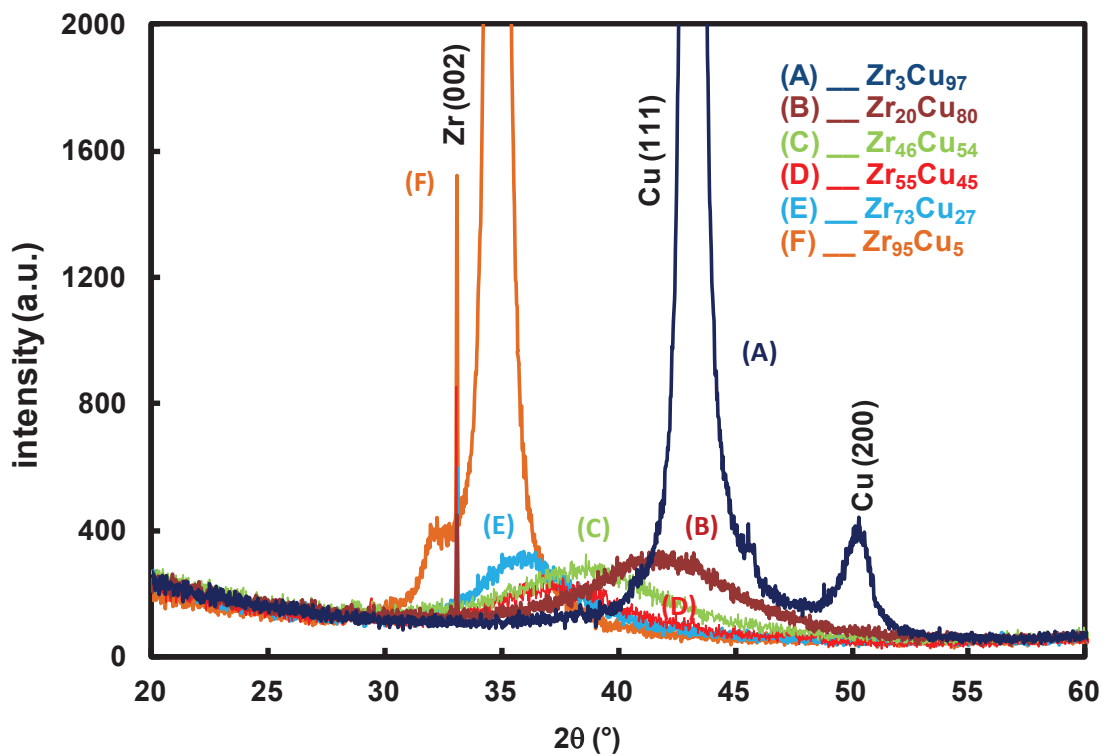


Figure 3.5 – Experimental XRD patterns of Zr_xCu_{100-x} film sputtered at 300 K with different compositions.

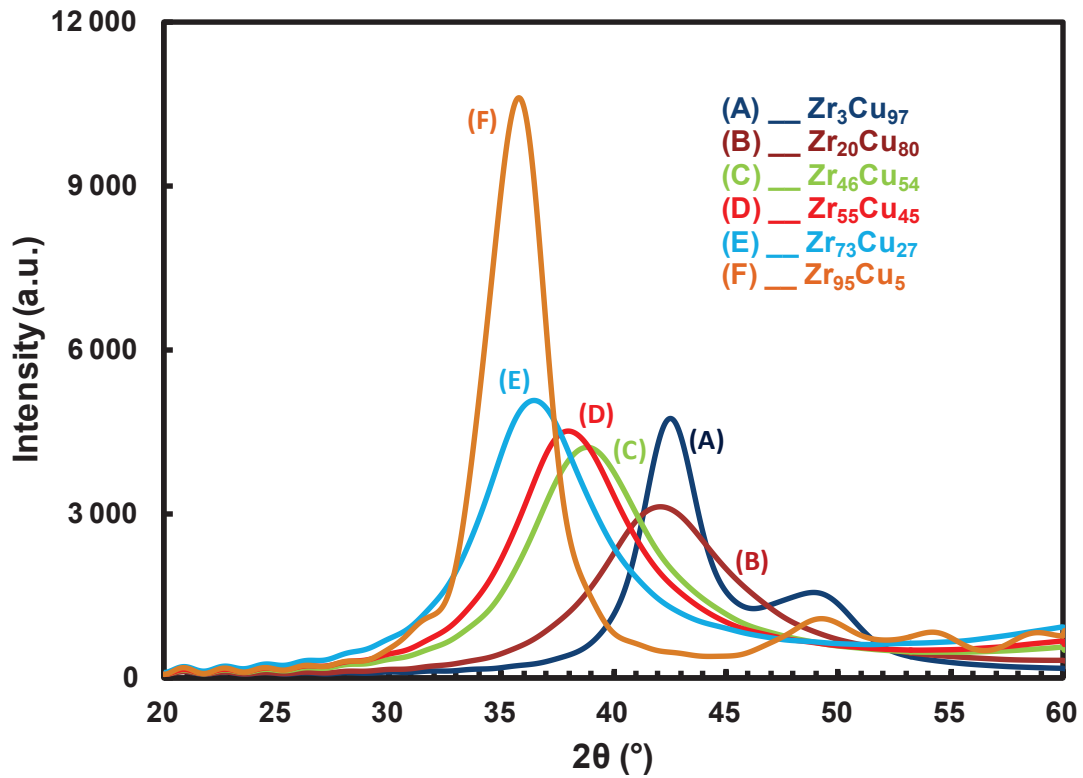


Figure 3.6 – Simulated X-Ray intensity vs. 2θ of Zr_xCu_{100-x} film with different compositions.

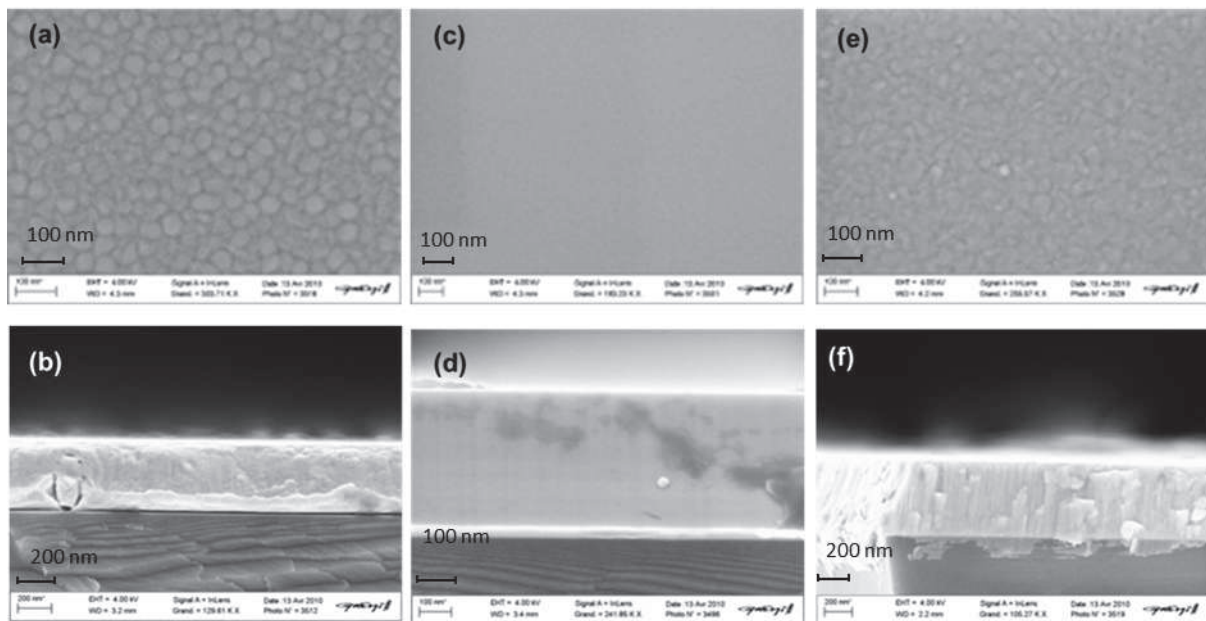


Figure 3.7 - SEM images of Zr-Cu films deposited on Si(100) at 3% (a, b), 73% (c, d) and 95% (e, f) Zr metal content; image (a), (c), (e) is about surface, image (b), (d), (f) is about cross section.

3.4.2 Zr_xCu_{100-x} ($10 \leq x \leq 90$) thin films deposited on a silicon (100) substrate: effect of the deposited atom kinetic energy

In this part three different experimental conditions of plasma sputter deposition are simulated, involving a more detailed composition analysis. This is intended for determining the role of both the composition and the deposited atom kinetic energy on the formation of the amorphous phase.

3.4.2.1 Result and discussion in condition 1

Condition 1 was already treated in the previous section. To more precisely study the appearance of the amorphous phase, the range of composition has been extended. The films grew to approximately 4 ~ 9 nm, the thickness of the films varies depending on the Zr/Cu ratio similar as section 3.3.2, The morphology of films deposited on the Si(100) are displayed in figures 3.16.

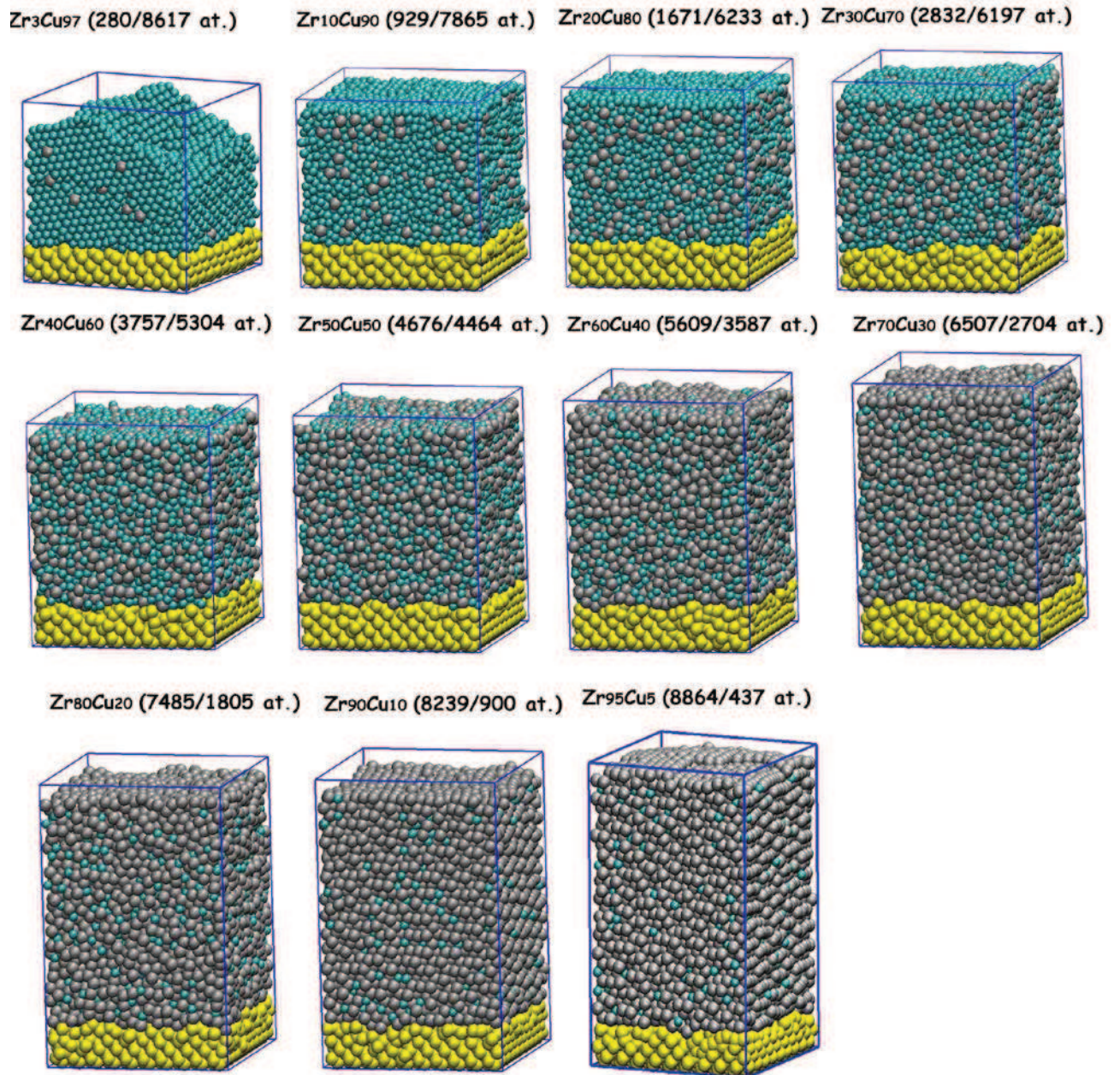


Figure 3.8 - Snapshots of Zr-Cu coatings deposited on Si(100) substrate at different Zr/Cu ratios (the numbers in brackets are the Zr and Cu atom numbers respectively). ●Zr, ●Cu, ●Si

Based on these simulations, the RDFs of all-all, Zr-Zr and Cu-Cu for Zr metal contents varied from 3% to 95% are presented in figures 3.9-3.11. As mentioned above the first peak shifts towards large radial distance as the concentration of Zr increases from 3% to 95%, because the first neighbor distance of Zr (3.23 Å) is larger than that of Cu (2.55 Å). With the increase of Zr concentration, the structure of the system changed from Cu predominant film to Zr

predominant film. Meanwhile, in the RDFs of $Zr_{10}Cu_{90}$ to $Zr_{80}Cu_{20}$, the peak becomes broad and split comparing with Zr_3Cu_{97} , $Zr_{90}Cu_{10}$ and $Zr_{95}Cu_5$ which have outstanding peaks typical of a crystalline structure. Again the amorphous nature of these alloys is clearly shown on the snapshots presented in Figure 3.8.

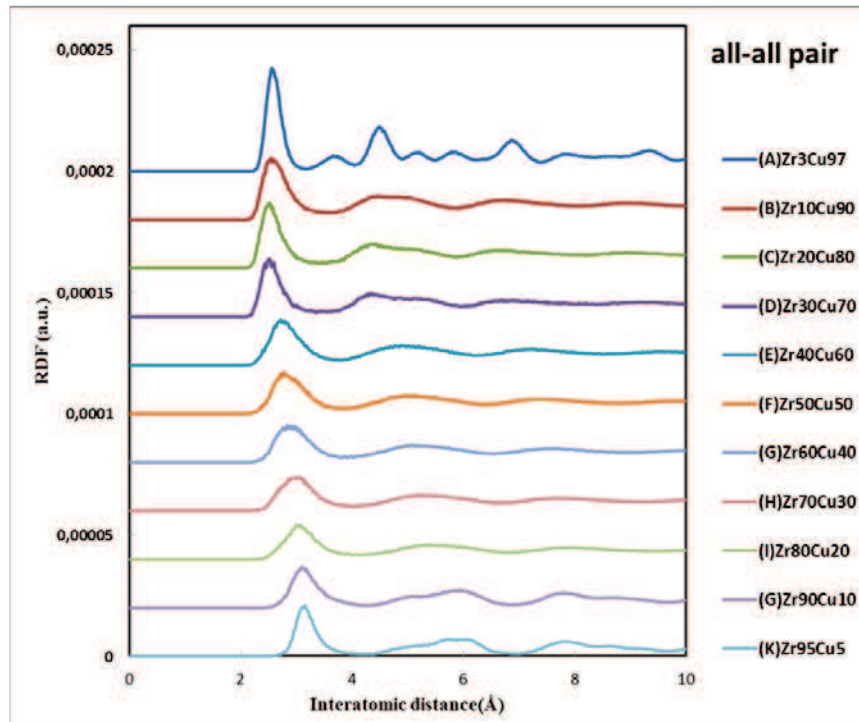


Figure 3.9 - Total RDFs for amorphous Zr_xCu_{100-x} alloys, Individual curves corresponding to different alloy compositions are displaced vertically for clarity.

When the Zr or Cu concentration increases in RDFs of Zr-Zr pair and Cu-Cu pairs respectively, the third and fourth peak slowly appears and become clear and sharp, which means the phase of Zr- Zr or Cu-Cu in the system changed from amorphous to crystalline.

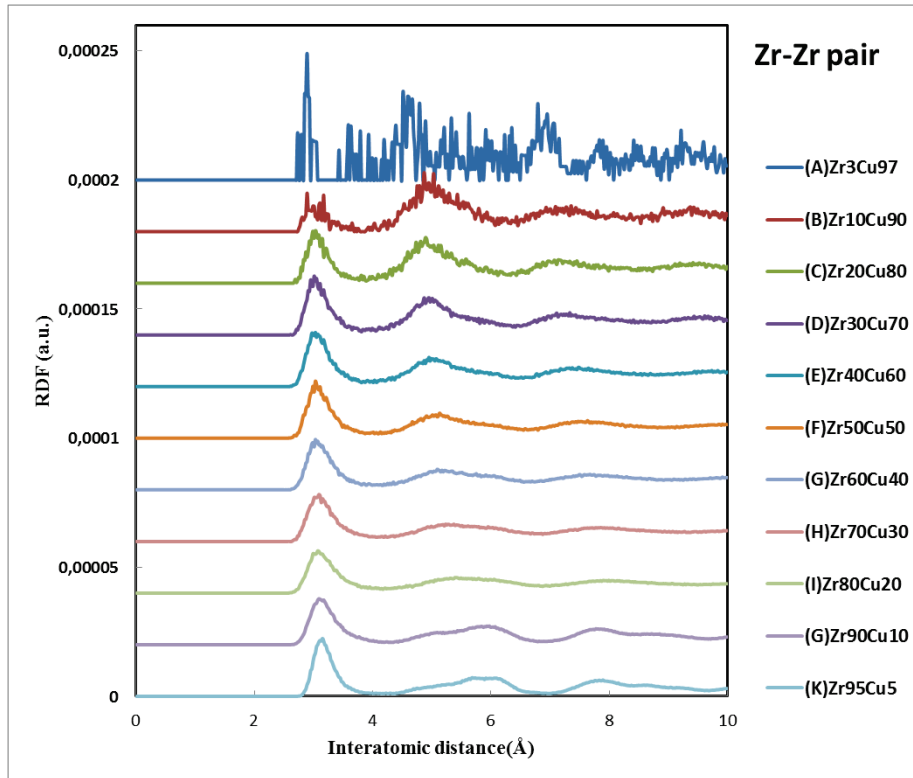


Figure 3.10 - RDFs for Zr-Zr for Zr_xCu_{100-x} alloys, individual curves corresponding to different alloys are displaced vertically for clarity.

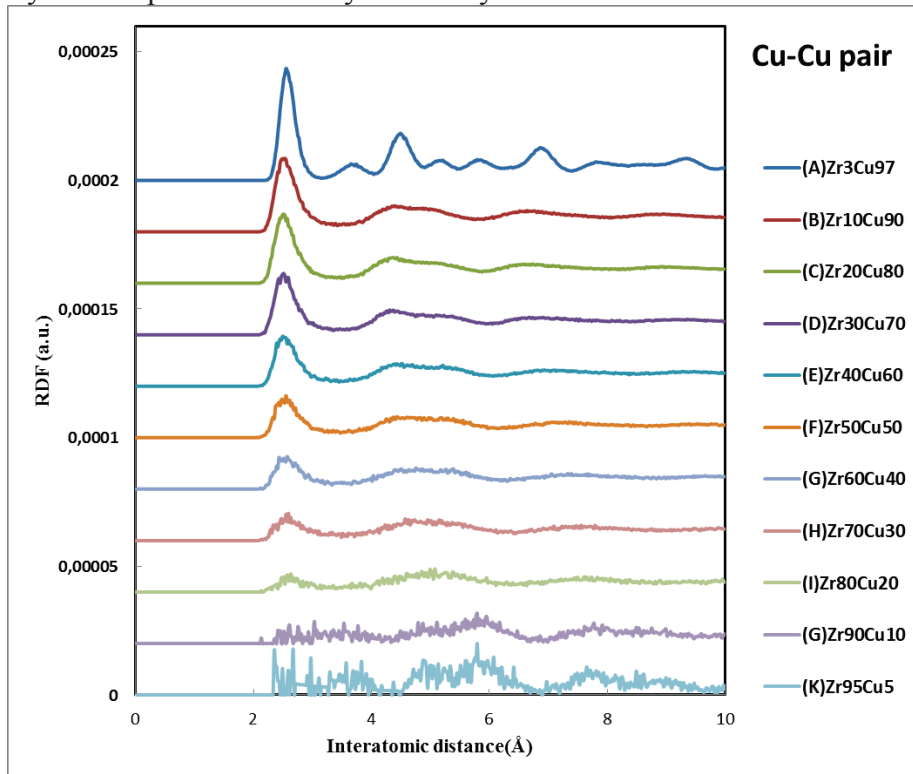


Figure 3.11 - RDFs for Cu-Cu for Zr_xCu_{100-x} alloys, individual curves corresponding to different alloys are displaced vertically for clarity.

The calculated X-ray intensities vs. 2θ of Zr_xCu_{100-x} simulated films are shown in figure 3.20. At high concentrations of Zr or Cu, for example, Zr_3Cu_{97} , $Zr_{90}Cu_{10}$ and $Zr_{95}Cu_5$, films show a crystalline XRD pattern which agrees with the present RDFs calculations reported in figure 3.9-3.11. However, $Zr_{10}Cu_{90}$ can be considered as an exception to this. With the same concentration, $Zr_{90}Cu_{10}$ has a crystalline structure, but $Zr_{10}Cu_{90}$ is amorphous which is clearly shown from the snapshots of the films presented in Figure 3.8. This is again because of the atom size difference between Zr and Cu. In $Zr_{90}Cu_{10}$, Cu atom with the small diameter can enter the gap between the Zr-Zr, which has no or only little effect on the overall structure. While for $Zr_{10}Cu_{90}$, the small content of Zr, with the large diameter, disorders the crystalline structure of Cu.

Table 3.4 Position of the main XRD peak for ZrCu alloy in the simulation

Simulation		Unit: 2θ ($^\circ$)				
Zr-Cu	Zr_3Cu_{97}	$Zr_{10}Cu_{90}$	$Zr_{20}Cu_{80}$	$Zr_{30}Cu_{70}$	$Zr_{40}Cu_{60}$	$Zr_{50}Cu_{50}$
main peak	42.1	42.1	41.7	40.35	39.4	38.4
Zr-Cu	$Zr_{60}Cu_{40}$	$Zr_{70}Cu_{30}$	$Zr_{80}Cu_{20}$	$Zr_{90}Cu_{10}$	$Zr_{95}Cu_5$	
main peak	37.5	36.8	35.95	35.75	35.7	

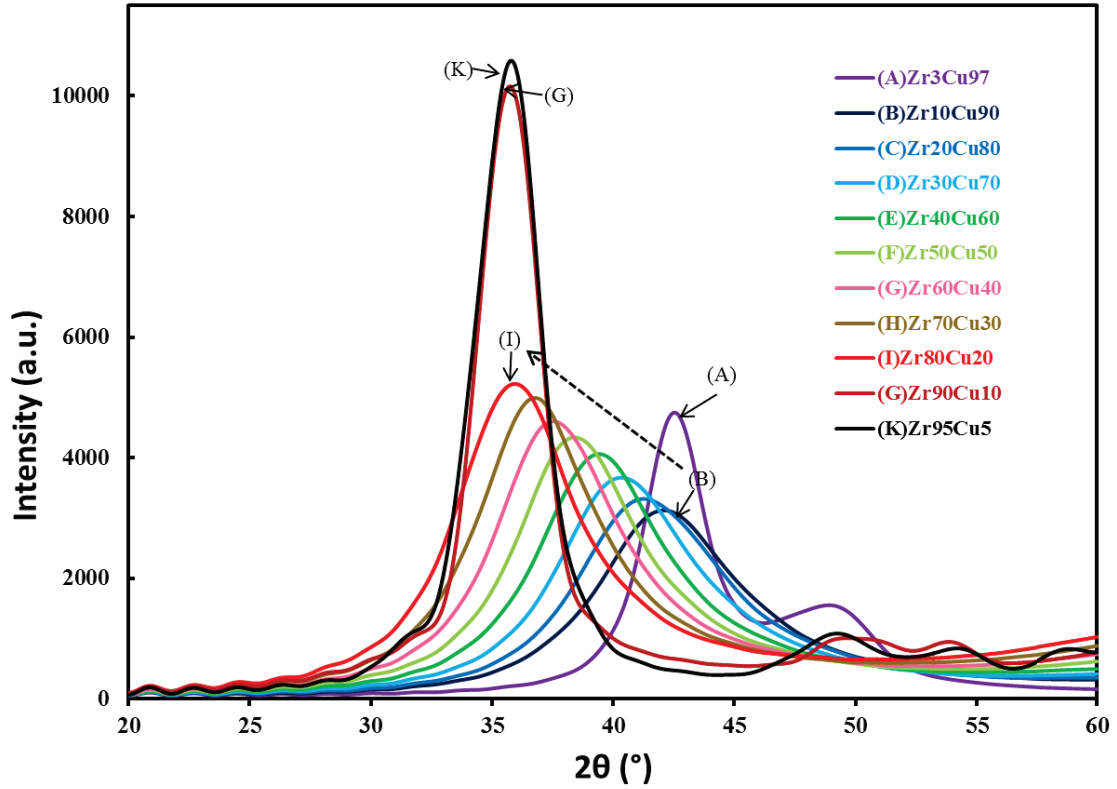


Figure 3.12 - X-Ray intensity vs. 2θ of Zr_xCu_{100-x} film with different compositions.

3.4.2.2 Result and discussion in Condition 2

In this simulation, the mean kinetic energy of incoming atoms is the largest among the three studied conditions with Zr 12.6 eV and Cu 9.61 eV. The films exhibit a more compact structure with a thickness of approximately 4 ~ 7.5 nm. Snapshots of the films deposited on the Si (100) are displayed in figures 3.13.

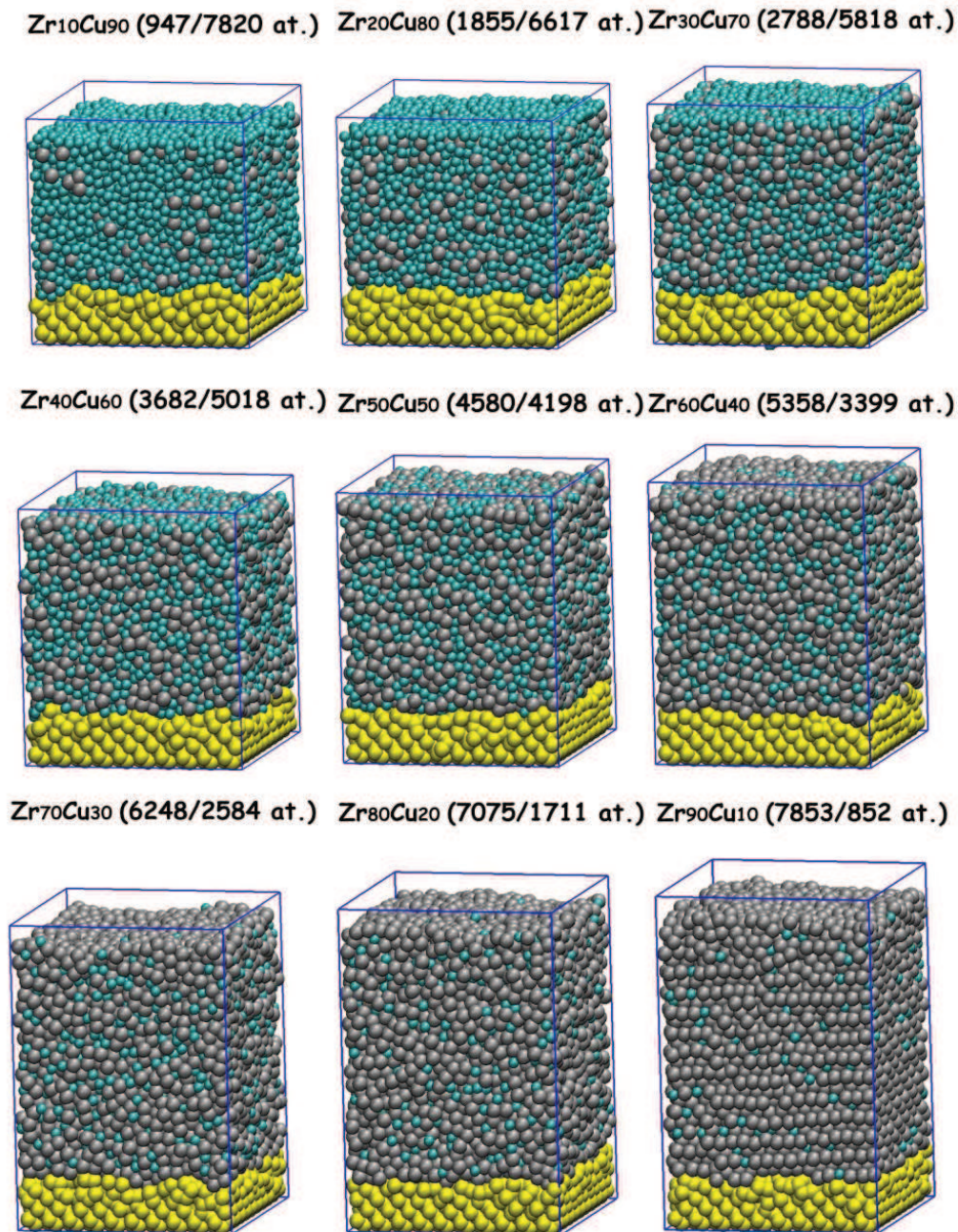


Figure 3.13 - Snapshots of Zr-Cu coatings deposited on Si(100) substrate at different ratios of Zr and Cu atoms (the numbers in brackets are the Zr and Cu atom numbers respectively). ●Zr, ●Cu, ●Si

Based on these simulations, RDF is calculated for each case and is presented in figures 3.14-3.16. In figure 3.14, the same trends as previously reported are observed when increasing Zr concentrations. This was the same as in previous simulations. In the Zr-Zr RDFs of Zr₉₀Cu₁₀, four peaks arise up, evidencing a well crystalline structure, which can be clearly seen from figure 3.14. From Zr₁₀Cu₉₀ to Zr₈₀Cu₂₀, the peaks become broad and split comparing with

Zr₉₀Cu₁₀ evidencing amorphous structures. Like in experiment 1, when the Zr concentration increases in RDFs of Zr-Zr pair, the third and fourth peak slowly appears indicating that the phase of Zr-Zr in the system change from amorphous state to crystalline.

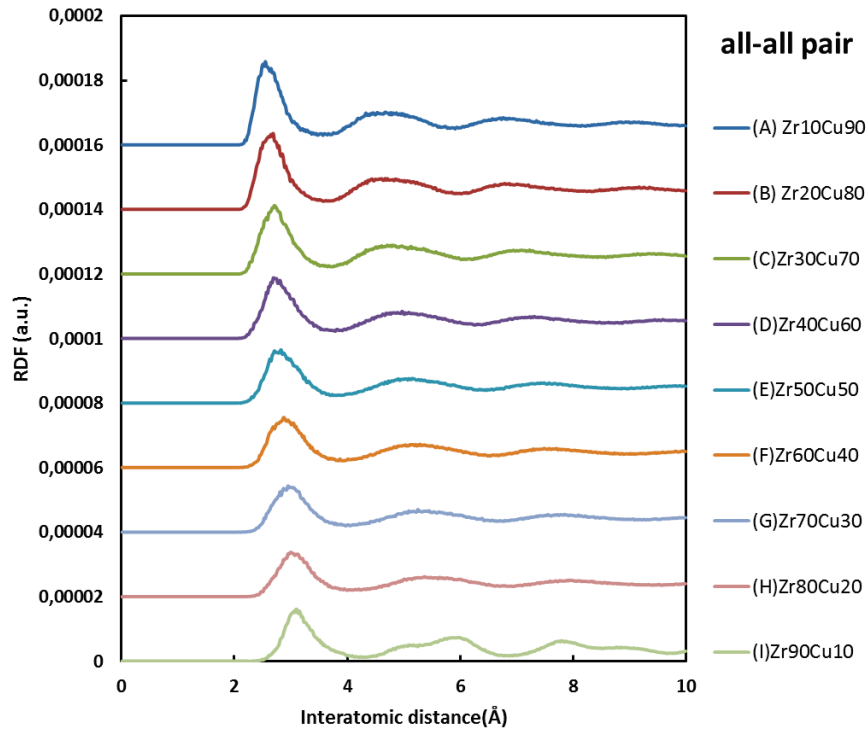


Figure 3.14 - Total RDFs for Zr_xCu_{100-x} alloys, individual curves corresponding to different alloy compositions are displaced vertically for clarity.

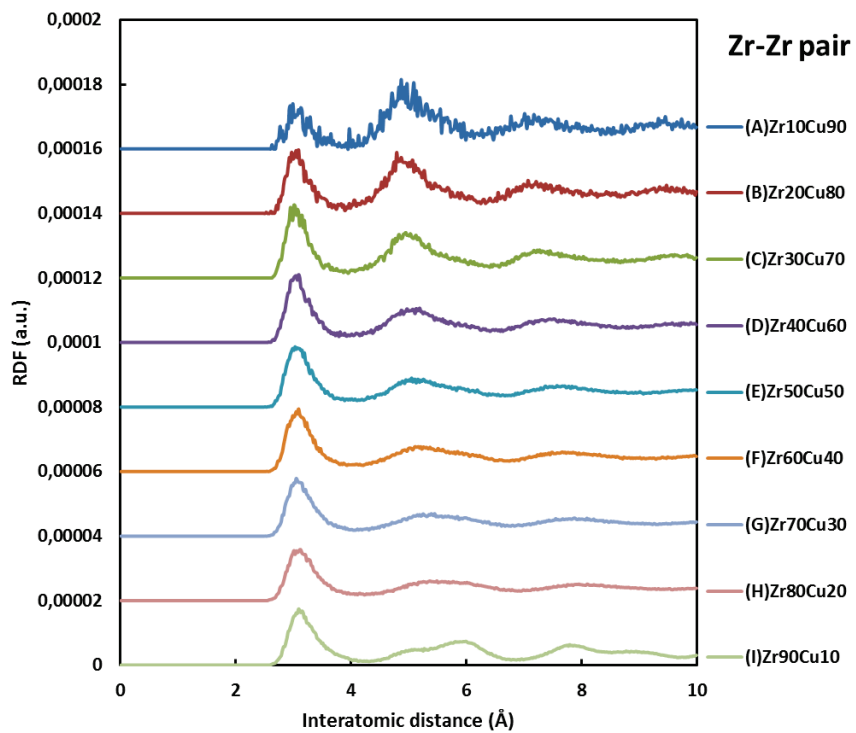


Figure 3.15 - RDFs for Zr-Zr for Zr_xCu_{100-x} alloys, individual curves corresponding to different alloys are displaced vertically for clarity.

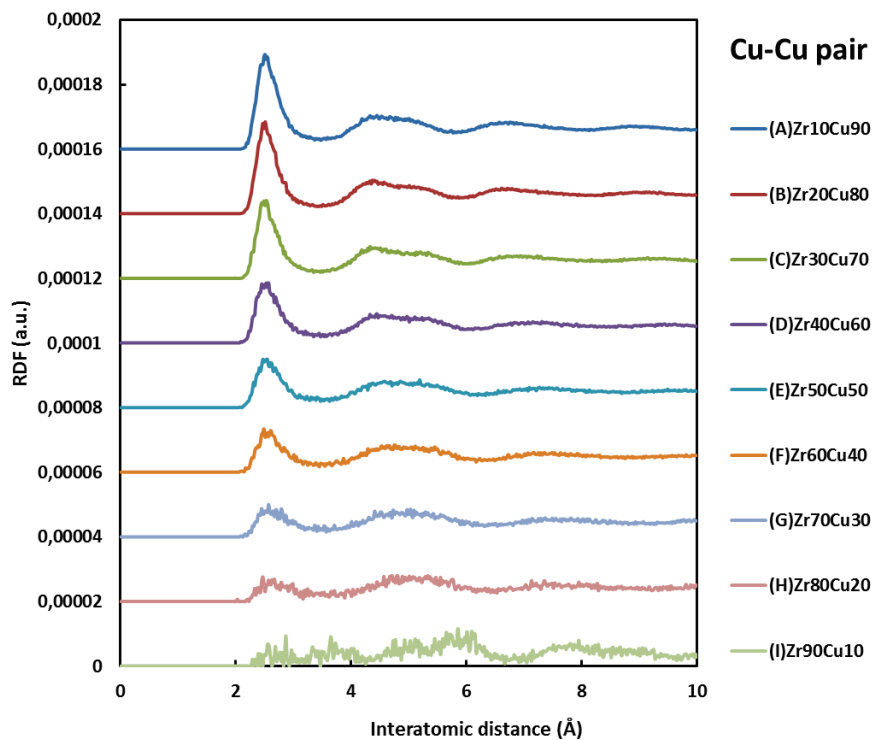


Figure 3.16 - RDFs for Cu-Cu for Zr_xCu_{100-x} alloys, individual curves corresponding to different alloys are displaced vertically for clarity.

Figure 3.17 shows the intensity and position of the XRD θ -2 θ peaks as a function of the Zr metal content. In this simulation, at the Zr concentration of 90%, the XRD peak is sharp showing the well crystalline state, which agrees with the RDFs presented in figure 3.14-3.16. As the Zr concentration increases from 10% to 80%, the peak is broad indicating the amorphous structure and the peak position shifts towards small angles (table 3.5). When comparing calculated XRD pattern with lower depositing energy in section 3.3.3, it was seen that $Zr_{90}Cu_{10}$ in both sets show a crystallized structure, while for the other ratios an amorphous structure is formed. This indicates the phase and structure of alloy is not much affected by the metal atom kinetic energy in the “high energy” domain. Figure 3.18 shows the specific orientation of the crystal structure of $Zr_{90}Cu_{10}$ in experiment 1 (A) and experiment 2 (B) deposited on Si(100). It can be seen that A present well crystallize structure, while B exhibits both crystalline and amorphous structure (1.5nm on the top).

During deposition, the deposit atoms make near normal impact with the growth surface. The kinetic energy of deposit atoms is transferred to the atoms near the impact site and the temperature of the system will rise. In order to mimic isothermal growth conditions, Berendsen thermostat was used in an intermediate region above the fixed Si(100) substrate, for energy dissipating and maintaining the substrate at a desired temperature. If the energy of an incoming atom is so large (experiment 2) and is not dissipate in time, this will introduce a higher temperature at the top surface and this will introduce amorphous structure. While with lower energy (experiment 1), the larger kinetic energy of deposit atoms can be properly dissipate, facilitating the deposit atoms hop to the sites of stronger binding and forming crystalline.

Table 3.5 - Position of the main XRD peak for ZrCu alloy in the simulation.

Simulation	Unit: 2θ(°)				
Zr-Cu	Zr ₁₀ Cu ₉₀	Zr ₂₀ Cu ₈₀	Zr ₃₀ Cu ₇₀	Zr ₄₀ Cu ₆₀	Zr ₅₀ Cu ₅₀
main peak	41.85	41.3	40.2	39.15	38.2
Zr-Cu	Zr ₆₀ Cu ₄₀	Zr ₇₀ Cu ₃₀	Zr ₈₀ Cu ₂₀	Zr ₉₀ Cu ₁₀	
main peak	37.55	36.75	35.7	35.65	

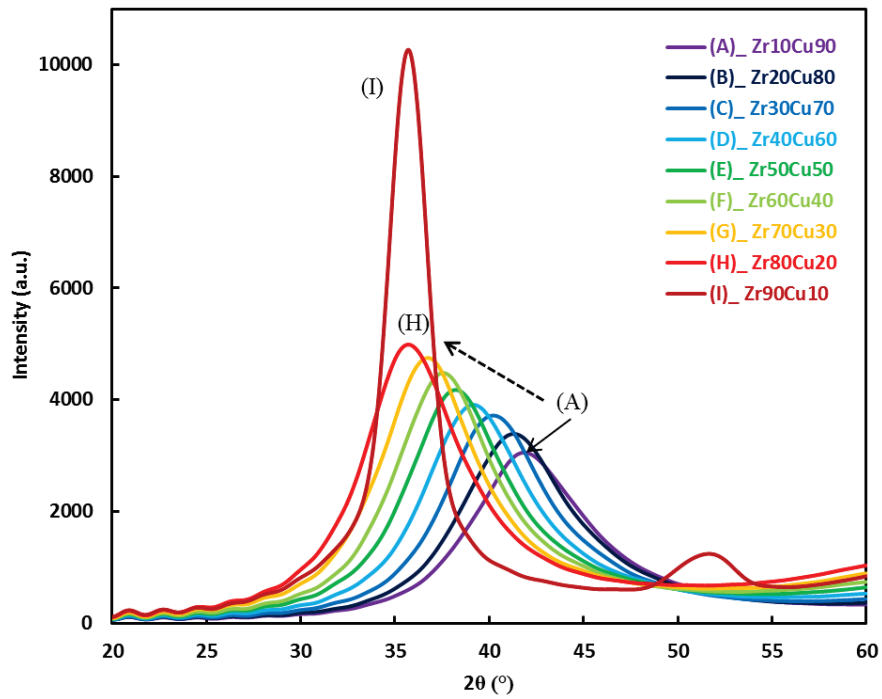


Figure 3.17 – Calculated X-Ray intensity vs. 2θ of Zr_xCu_{100-x} film with different compositions.

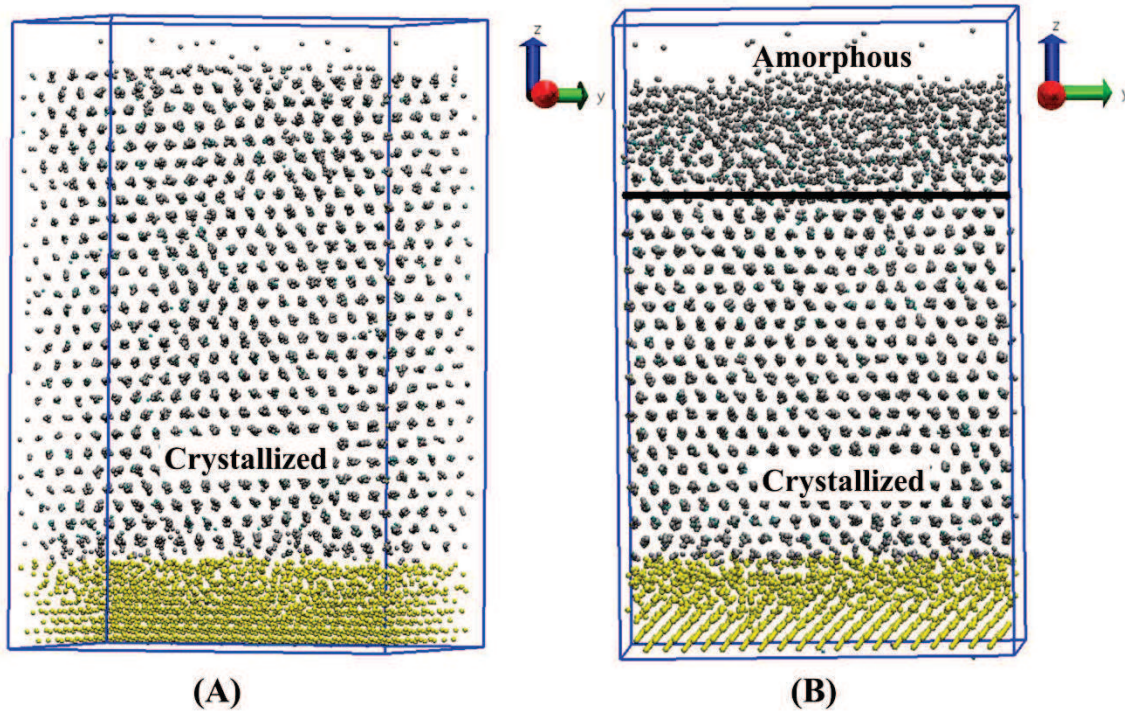
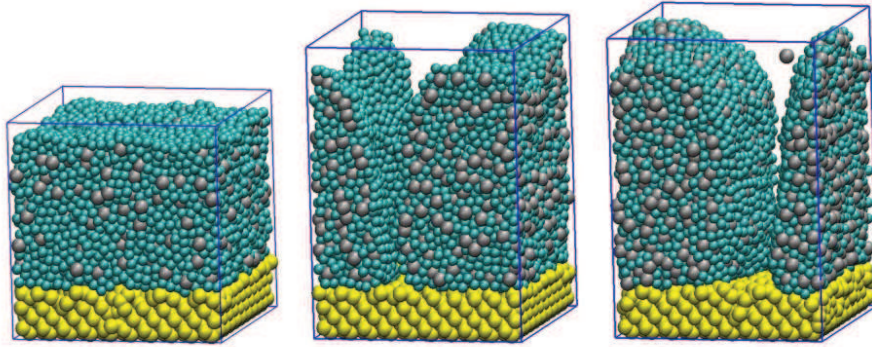


Figure 3.18 - Snapshots of $Zr_{90}Cu_{10}$ in experiment 1 (A) and experiment 2 (B) deposited on Si(100) substrate with their specific orientation showing the crystal structure. Solid line in B is used to separate the amorphous and crystalline structures.

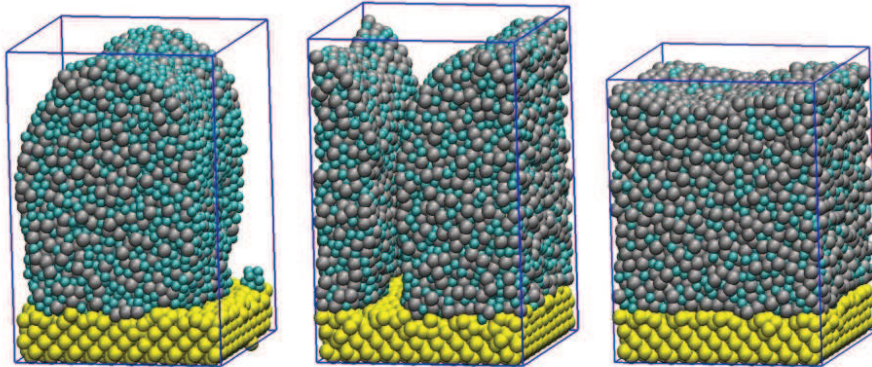
3.4.2.3 Result and discussion in condition 3

In this simulation, the mean kinetic energy of incoming atoms is very low: Zr 0.13eV and Cu 0.34 eV. Snapshots of the films deposited on the Si(100) are displayed in figures 3.19. It is interesting to see that, as the Zr concentration increases, the morphology goes through three different stages: film – cluster – film. As we can see from figure 3.19, $Zr_{10}Cu_{90}$ is deposited as a film with a thickness around 4 nm. Then from $Zr_{20}Cu_{80}$ to $Zr_{50}Cu_{50}$, the deposit atoms grow as clusters with height ranging from 6.5 nm ~ 7.5 nm. Finally, for $Zr_{60}Cu_{40}$ to $Zr_{90}Cu_{10}$, film is formed with thickness ranging from 5 nm ~ 7.5 nm.

Zr₁₀Cu₉₀ (873/7854 at.) Zr₂₀Cu₈₀ (1786/7136 at.) Zr₃₀Cu₇₀ (2695/6320 at.)



Zr₄₀Cu₆₀ (3573/5413 at.) Zr₅₀Cu₅₀ (4540/4506 at.) Zr₆₀Cu₄₀ (5398/3602 at.)



Zr₇₀Cu₃₀ (6138/2642 at.) Zr₈₀Cu₂₀ (7063/1751 at.) Zr₉₀Cu₁₀ (8212/908 at.)

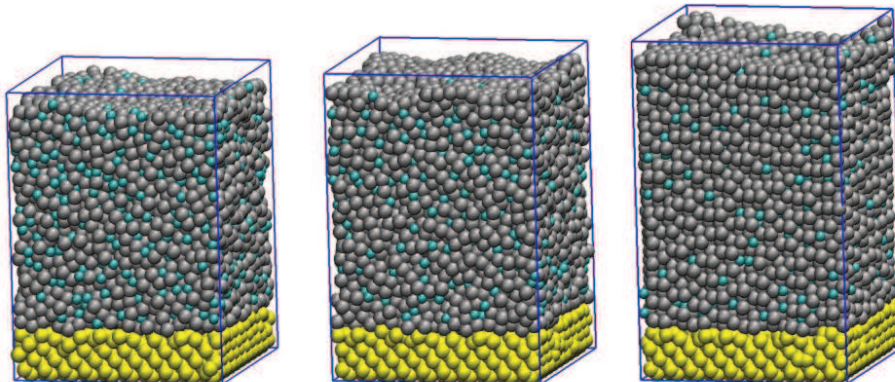


Figure 3.19 - Snapshots of Zr-Cu coatings deposited on Si(100) substrate at different ratios of Zr and Cu atoms (the numbers in brackets are the Zr and Cu atom numbers respectively). Zr, ●Cu, ●Si

Figure 3.20 shows RDFs of the all-all pair in this simulation. For the RDFs in Zr₉₀Cu₁₀, four peaks arise up in this plot showing the well crystallized structure, which can be clearly seen from figure 3.19. From Zr₁₀Cu₉₀ to Zr₈₀Cu₂₀, the peaks behave like the former simulations, showing an amorphous structure. RDFs for Zr-Zr and Cu-Cu in this system are shown in figure 3.21 and 3.22 respectively. At low Zr concentration (Zr₁₀Cu₉₀), the Zr-Zr RDF exhibit

three peaks, though blurred, which still indicates several bonds are created between Zr-Zr in their first and second nearest neighbor distance. When the Zr concentration increases, the third and fourth peaks slowly appears and in $Zr_{90}Cu_{10}$, the peaks become “higher and narrower” indicating the Zr-Zr’s phase changing from amorphous state to crystalline. In $Zr_{10}Cu_{90}$, the peak is broad and split, as discussed above, this is caused by the different atom sizes. When Cu content decreases, there is a change to amorphous.

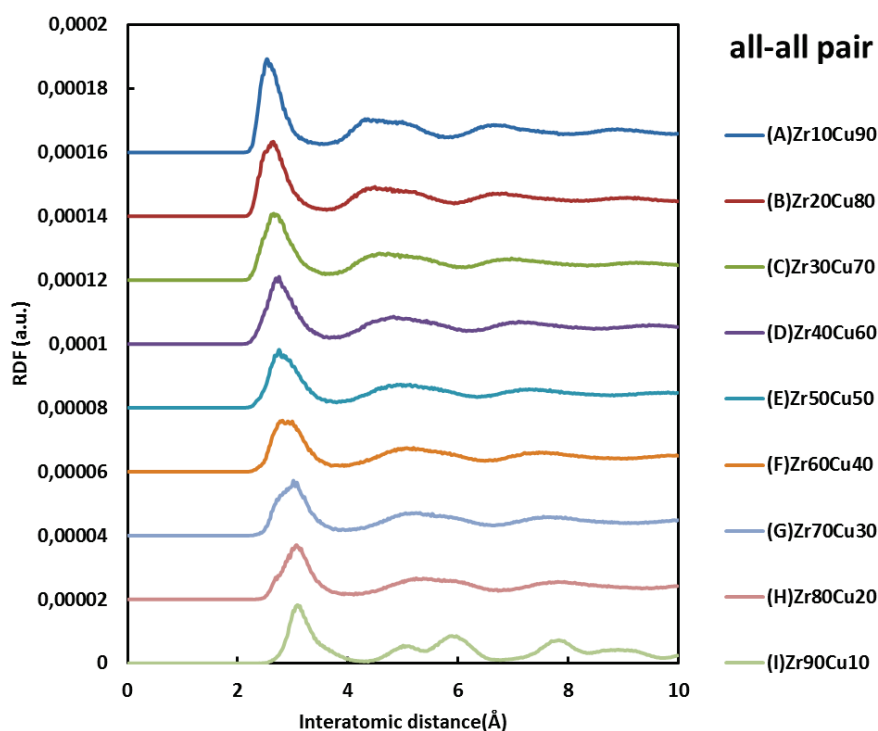


Figure 3.20 - Total RDFs for Zr_xCu_{100-x} alloys, individual curves corresponding to different alloy compositions are displaced vertically for clarity.

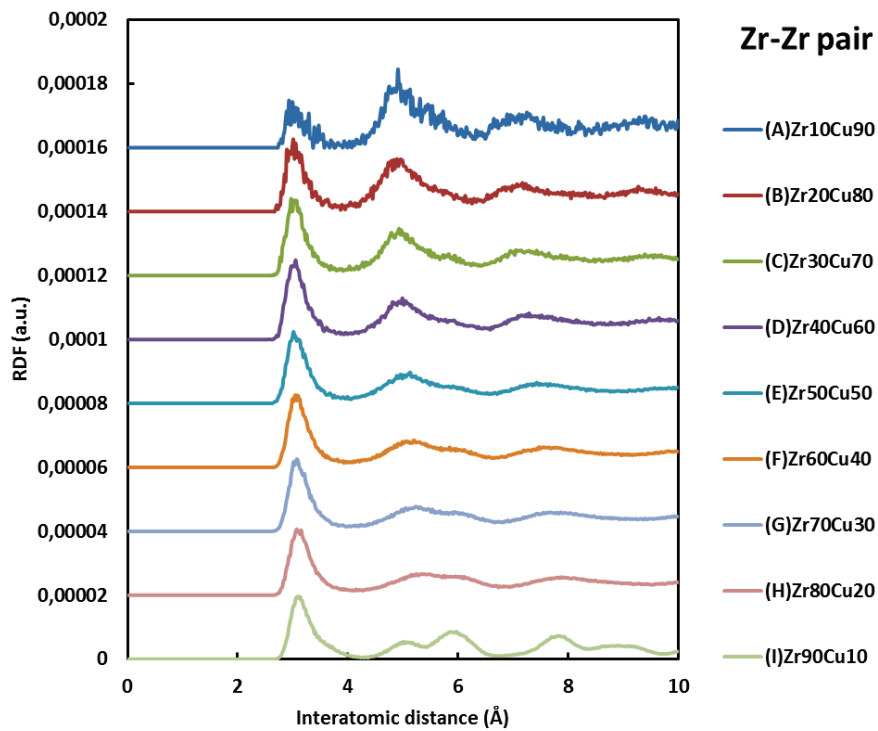


Figure 3.21 - RDFs for Zr-Zr for Zr_xCu_{100-x} alloys, individual curves corresponding to different alloys are displaced vertically for clarity.

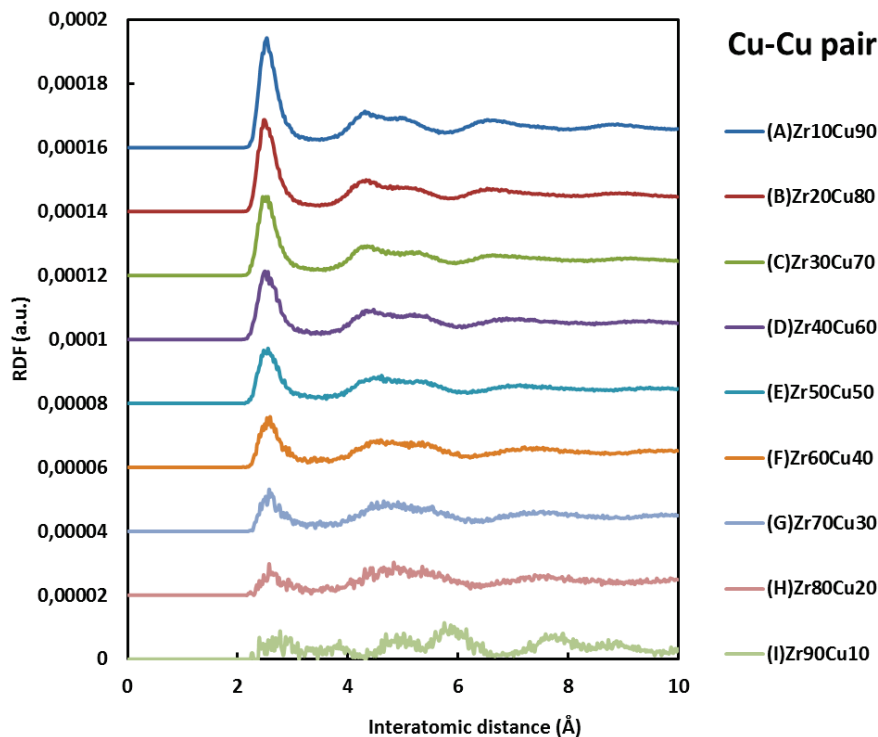


Figure 3.22 - RDFs for Cu-Cu for Zr_xCu_{100-x} alloys, individual curves corresponding to different alloys are displaced vertically for clarity.

Figure 3.23 shows the intensity and position of the XRD θ - 2θ peaks as a function of the Zr metal content. Again at the Zr concentration of 90%, Zr_xCu_{100-x} films are crystalline which agrees with snapshot in figure 3.19. As the Zr concentration increases from 10% to 80%, a shift of the peaks towards small angles (table 3.6) is observed. At the same time, all of these patterns consist of broader peaks, indicating a low ordered structure.

Table 3.6 Position of the main XRD peak for ZrCu alloy in the simulation

Simulation		Unit: $2\theta(^{\circ})$			
Zr-Cu	$Zr_{10}Cu_{90}$	$Zr_{20}Cu_{80}$	$Zr_{30}Cu_{70}$	$Zr_{40}Cu_{60}$	$Zr_{50}Cu_{50}$
main peak	42.45	41.6	40.5	39.7	38.65
Zr-Cu	$Zr_{60}Cu_{40}$	$Zr_{70}Cu_{30}$	$Zr_{80}Cu_{20}$	$Zr_{90}Cu_{10}$	
main peak	37.8	37.0	36.25	35.7	

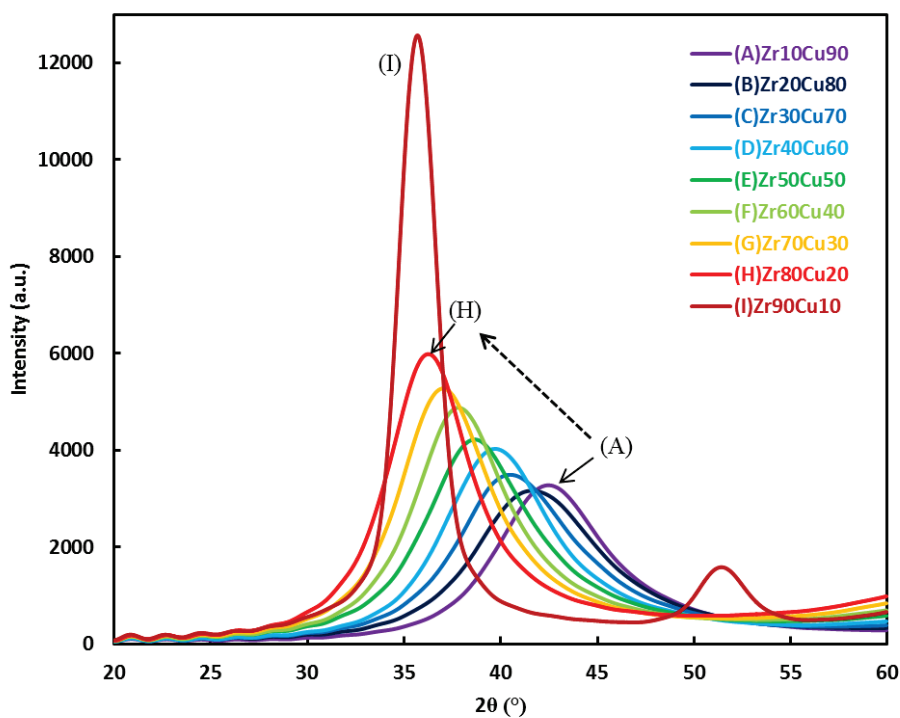


Figure 3.23 - Calculated X-Ray intensity vs. 2θ of Zr_xCu_{100-x} film with different compositions.

In order to study the mechanism of film growth of $Zr_{90}Cu_{10}$, snapshot of $Zr_{90}Cu_{10}$ with lower deposit energy (experiment 3) is shown in figure 3.24. The black solid line shows the crystal lattice orientation. Clearly, the film exhibits two grains: one in orientation marked as “A” and the other in orientation marked as “B”. One interesting discovery is that only the simulation with lower energy contained the two orientations.

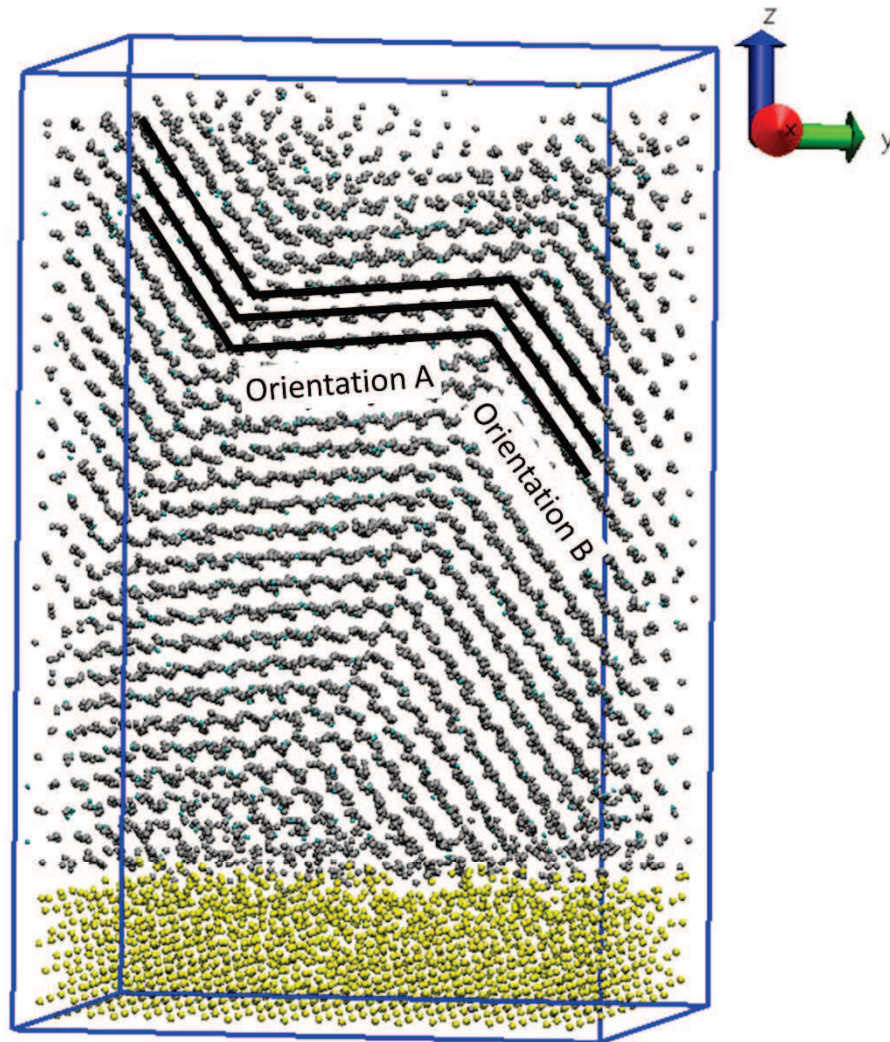


Figure 3.24 – Snapshot of $Zr_{90}Cu_{10}$ with lower energy (experiment 3), blue outline show its original cell in MD simulation and solid line show the crystal lattice orientation.

At the beginning of the deposition process, the formed stable nuclei are crystalline with a random orientation distribution. As a result, the growth and coalescence of small cluster leads to its coarsening. In this simulation the energy of deposited atom is not high enough to overcome the activation energy for diffusion and restructuration between clusters cannot

occur. Therefore the boundary is immobile through all the film thickness. As the depositions goes on, the clusters have a similar growth rate but with different growing direction, as a result, it formed the two gain cluster with different lattice orientations.

3.5 Solid-solution formation rules for the system Zr_xCu_{100-x}

According to reference of ZHANG et al [17, 30, 49, 50], the solid-solution formation rules can be used to characterize the collective behavior of the constituent elements in the multi-component alloys. Though this semi-empirical theory is applied on the multi-components with at least 4 elements, but the parameters of δ and Ω values can be used to indicate the trend of this binary alloy. So T_m cannot be considered as the true averaged melting temperature but some reference average parameter scaling as a temperature. The parameters of Zr_xCu_{100-x} defined for MD simulations were calculated and are listed in table 3.7 and mapped in figure 3.23 [30]. As we can see in figure 3.25, the δ and Ω values of the alloys are located in the area for bulk metal glasses (B). When the binary alloy has the equal or near equal atomic composition of Zr and Cu, e.g. $Zr_{50}Cu_{50}$, $Zr_{40}Cu_{60}$, or $Zr_{60}Cu_{40}$, it stayed in the center of BMGs indicating amorphous structure of the system. This is also evidenced by the three sets of MD simulation in section 3.3.3-3.3.5. As the high concentration of single element increases, samples enter the area of BMGs to solid-solutions, this corresponds to the result in the simulation, with high concentration of single element, and the system prefers to form crystalline structure. Besides, the solid-solution forming ability is not symmetric, for example, the δ and Ω of $Zr_{90}Cu_{10}$ is closer to the S zone than those of $Zr_{10}Cu_{90}$ showing a more pronounced tendency to form an amorphous compound, as evidenced before.

These rules are very useful for trying to predict the phase of multi component alloys. Even if these rules proposed by ZHANG applied for the equilibrium synthesis techniques, e.g. bulk

metal synthesis techniques, it is hard to get exact predictions for non-equilibrium synthesis techniques, like magnetron sputter deposition. Nevertheless, it can be used for qualitative predictions and for studying the expected materials when the chemical composition is varied .

Table 3.7 the microstructure and the parameters, δ , ΔH_{mix} , ΔS_{mix} , T_m , Ω and structure for $\text{Zr}_x\text{Cu}_{100-x}$ alloys.

	δ (%)	$\Delta H_{\text{mix}}(\text{KJmol}^{-1})$	$\Delta S_{\text{mix}}(\text{KJ}^{-1}\text{mol}^{-1})$	$T_m(\text{K})$	Ω	Structure
Zr10Cu90	7,32%	-8,28	2,703	1434,52	0,4683	BMGs(B)
Zr20Cu80	9,52%	-14,72	4,160	1511,24	0,4271	BMGs(B)
Zr30Cu70	10,66%	-19,32	5,079	1587,96	0,4174	BMGs(B)
Zr40Cu60	11,13%	-22,08	5,595	1664,68	0,4219	BMGs(B)
Zr50Cu50	11,11%	-23	5,763	1741,4	0,4363	BMGs(B)
Zr60Cu40	10,65%	-22,08	5,595	1818,12	0,4607	BMGs(B)
Zr70Cu30	9,75%	-19,32	5,079	1894,84	0,4981	BMGs(B)
Zr80Cu20	8,33%	-14,72	4,160	1971,56	0,5572	BMGs(B)
Zr90Cu10	6,12%	-8,28	2,703	2048,28	0,6686	BMGs(B)

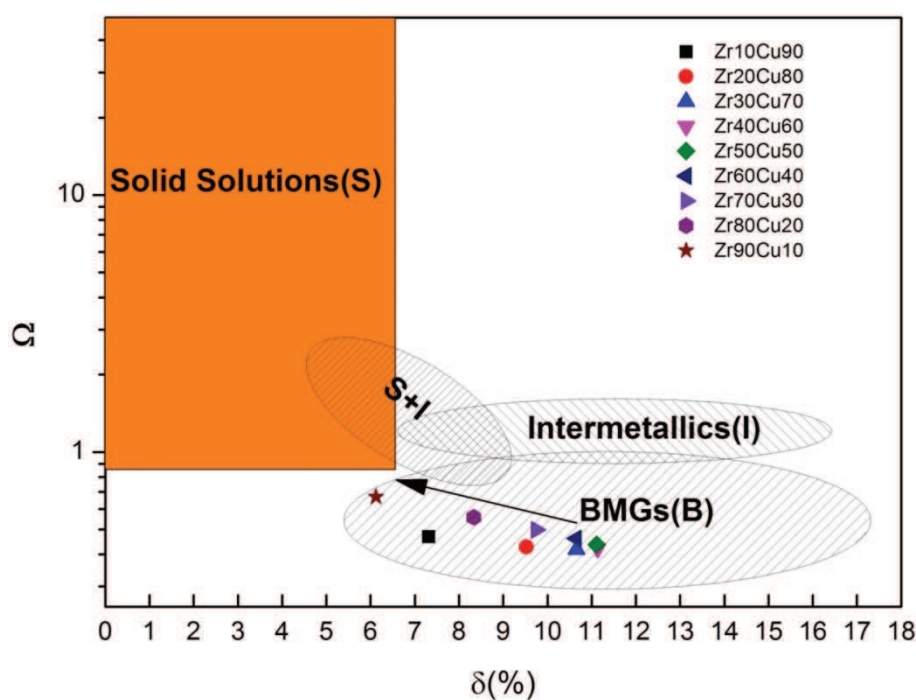


Figure 3.25 - The relationship between parameters δ and Ω for multi-component alloys

3.6 Conclusions

Zr_xCu_{100-x} thin films grown by magnetron co-sputtering process were studied by MD simulations using initial conditions similar to the experimental operating ones. The crystallinity of the films was analyzed by calculated RDFs and XRD. The results show that films containing large amount of one of the element (higher than 80%) are crystallized, whereas for intermediate compositions low ordered phase is evidenced. This trend is due to chemical disorder, since both atoms seem to be incorporated in the same lattice (solid solution) which induces distortion of the parameter. The results from the MD simulations were compared with XRD analyses of the experimentally deposited thin films. The experimental results also show that the structure of the films changes from crystalline at a high or low Zr content to amorphous at intermediate Zr contents, ranging from 20 to 75%.

Results also show that the morphology of the films has much correlation with mean kinetic energy of the incoming atoms. With higher depositing energy, it is likely to form a compact and uniform film. With lower energy, the morphology will be clusters or film depending on the atomic composition.

The good agreement between experimental results and simulation is of particular interest: it proves that modeling at the atomic level allows predicting the structure of hundreds of nanometer thick films grown by magnetron sputter deposition. MD may thus be a helpful tool for designing of new alloys.

Chapter 4: Molecular dynamics simulation of AlCoCrCuFeNi high entropy alloy thin film deposition and annealing onto silicon

Dans ce chapitre, nous étudions le dépôt et les propriétés de recuit de AlCoCrCuFeNi, alliage à haute entropie (HEA) en film mince, sur Si (100) substrats. Les alliages à haute entropie (HEA) sont des composés métalliques contenant de six à 13 éléments, avec une concentration dans la gamme de 5 à 35% pour chaque élément. Dans ces alliages, en raison de la forte entropie de mélange, la formation de phases intermétalliques fragiles sont évitées et des solutions solides multi-éléments sont plutôt stabilisés (FCC et / ou BCC). La combinaison de nombreux éléments métalliques de tailles différentes induit une diffusion atomique lente, conduisant à des structures nanocristallines ou amorphes.

Les films de HEA obtenus par simulation MD possèdent la structure fcc/bcc selon la composition, ce qui correspond également aux résultats expérimentaux. En analysant l'évolution des paramètres δ et Ω , une tendance à évoluer vers une structure de solution solide de verres métalliques massifs a été trouvée. Cette méthode peut donc aider à prédire qualitativement de phase pour les HEA dont la composition chimique varie.

L'étude du recuit simulé par MD montre des agrégats de AlCoCrCuFeNi qui évoluent de 200K à 1500K. La coalescence induite des agrégats s'accompagne d'un processus de fusion partielle. Il démarre vers 1050 K où les atomes individuels se déplacent à l'intérieur et en surface des agrégats, se traduisant par un saut dans le déplacement quadratique moyen (RMSD) total. Par ailleurs, les calculs XRD à différentes températures de recuit montrent la transition entre la phase bcc à la phase fcc en accord avec l'expérience. En outre, la composition du HEA est un facteur critique qui affecte la structure et cela a été démontré et comparé à l'expérience

4.1 Introduction

In this chapter, we study the deposition and annealing properties of AlCoCrCuFeNi high entropy alloy (HEA) thin film on Si(100) substrates. High Entropy Alloys (HEA) are metallic compounds containing six to 13 elements with a concentration in the range 5 to 35% for each element [51]. In these alloys, because of the high entropy of mixing, formation of brittle intermetallic phases are avoided and multielement solid solutions are rather stabilized (FCC and/or BCC) [30]. The combination of numerous metallic elements with different sizes induces a sluggish atomic diffusion, leading to nanocrystalline or amorphous structures.

Bulk HEAs have been extensively studied for their excellent properties and performance, including outstanding strength and resistance to oxidation at high temperatures, anti-adhesion, corrosion resistance, high temperature stability, hydrophobicity, high stiffness, strength and toughness, high hardness and high-strain-rate superplasticity [52-54].

However, HEAs are quite difficult to synthesize as bulk materials and, for many applications, transferring their exceptional properties to a bare material may be of interest. Few studies on HEA thin films deposited by magnetron sputtering have been published [55-61] starting from alloyed targets formed by melting or casting, or from mosaic ones [60, 61]. HEAs can be viewed as atomic-scale composites. Their final properties come from 1) the combination of properties of their constituting elements and 2) the stabilized solid solutions and structures. Thus for the design of new alloys dedicated to a given application, prediction of structural features of the thin film would be of particular interest. Despite this applicative goal, understanding of the growth mode of such complex multielement films is a challenging research subject.

Available literature on metallic alloy thin film growth allows carrying out simulation of the process at the atomic level. The present study is concerned with molecular dynamics simulations for studying growth and thermal stability of HEA thin films. The HEA chosen as a reference has already been studied by many groups [52, 53, 56, 57].

For comparison with simulations, we are considering previously published results on AlCoCrCuFeNi HEA thin films and recent experiments carried out at GREMI. The HEA thin films are deposited by magnetron sputtering from three mosaic targets and this has been used for easily tailoring the film composition. By tuning the ratio of the powers applied to the magnetron targets, samples with various chemical compositions have been obtained. X-ray diffraction (XRD), Energy Dispersive Spectroscopy (EDS) and Scanning Electron Microscopy (SEM) were carried out to show the chemical composition, surface morphologies and crystalline phase transformation during deposition. We also study the stability of

AlCoCrCuFeNi thin films at temperatures in the range 383-1083 K by the process of annealing. From XRD performed during annealing, modifications of the film structure have been evidenced above 783 K, depending on the initial structure (or chemical composition) of the as-deposited HEA [61].

Based on the experiment, molecular dynamics simulations are carried out for describing deposition and annealing of AlCoCrCuFeNi HEA thin films. The simulation was done using molecular dynamics with EAM potential and the Verlet algorithm, taking into consideration the difference in crystal structure and atomic size of the constituent elements.

4.2. Experiments

To synthesize HEA thin films, DC magnetron sputtering technique is carried out with mosaic targets (patent no.WO/2008/028981). Three targets are placed in the chamber in front of rotating Si(100) substrates in order to ensure large overlapping of the sputtered atom fluxes of pure elements (99.99%). The six chemical elements are arranged on the targets (Figure 4.1): Fe, Co and Ni are on target 1, Cu and Cr on target 2 and Al on target 3.

To adjust the stoichiometry of AlCoCrCuFeNi alloy, the relative surface fraction of each element on the target is calculated, taking into account the difference in sputtering yields estimated with TRIM software. All experiments are performed at room temperature and at the Ar pressure of 0.2 Pa. The distance between target and substrate is 9 cm. A deposition time of 25 min is chosen to synthesize thin films of more than 1 μm thick on Si(100) substrates. To determine the morphology, grain size, film thickness and chemical composition, SEM (Carl Zeiss supra-40 FEG-SEM) is used with EDS (BruckerXFlash Detector 4010). X-ray diffraction (XRD) experiments are performed in vacuum (1.7×10^{-2} Pa) with a Brucker D8 diffractometer using the Cu $K\alpha$ radiation and with a scanning speed of $40 \text{ }^\circ\text{C min}^{-1}$ [58].

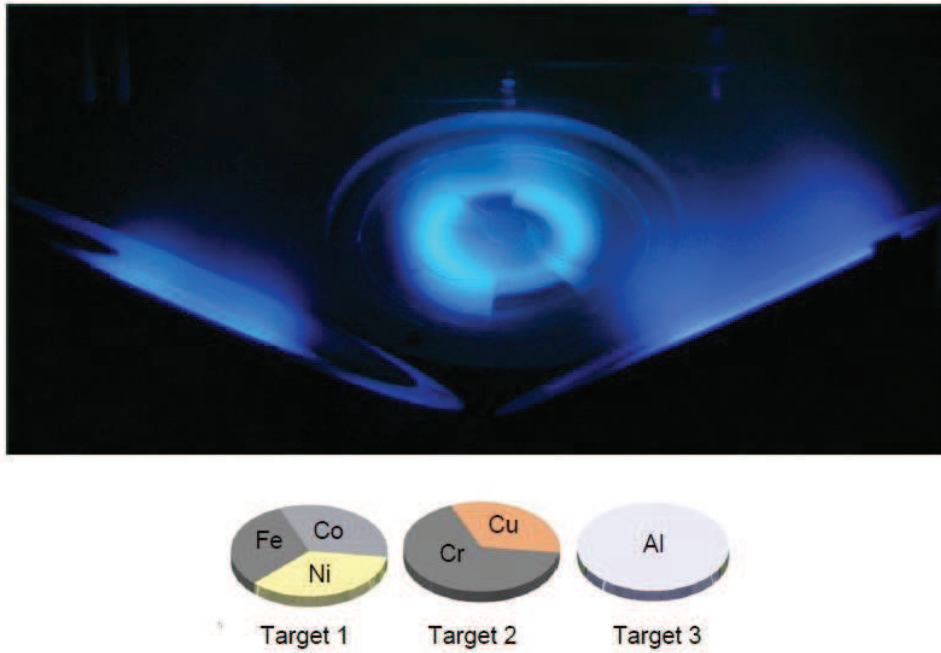


Figure 4.1 – Image of the magnetron sputtering chamber showing the three targets used to deposit high entropy alloys, and the schematic of the three mosaic targets oriented towards the substrate.

4.3 MD simulation of magnetron sputtering deposition

MD simulation is carried out using the procedures in section 2.2.2. The integration time-step is chosen to be 1fs. The HEA atoms deposit on Si(100) substrate with an incident energy of 1eV, which was calculated according to the experiment condition described in section 2.2.1. Two substrates are chosen for the subsequent simulations: 1) Si(100) with dimensions (100×100×20) Å in section 4.4.1 and 4.4.2), 2) Si(100) with dimensions (17×17×20) Å in section 4.2.3. The deposition model of the six atoms is shown in Figure 4.2.

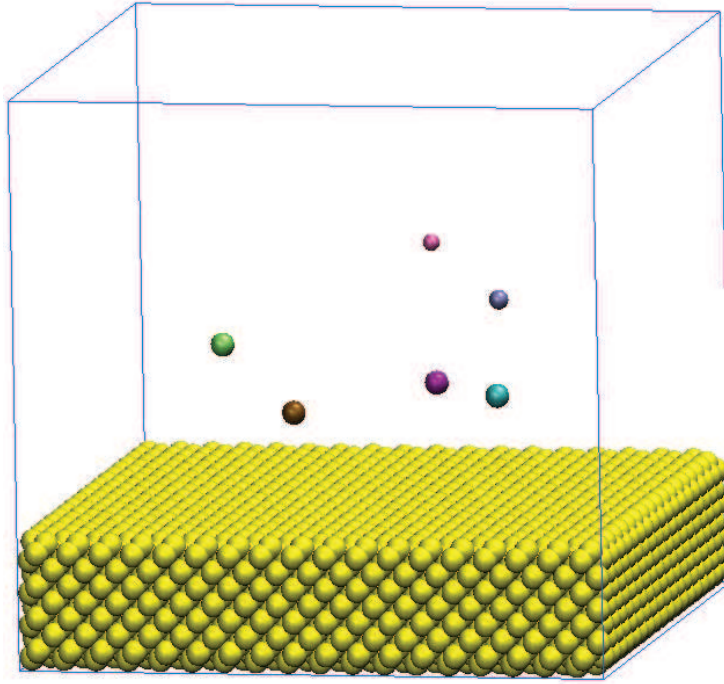


Figure 4.2 - Schematic picture of the initial HEA atoms deposition model. ●Al, ●Co, ●Cr, ●Cu, ●Fe, ●Ni, ●Si

In section 4.4.1, we presented the growth of HEA clusters based on three different HEA atoms compositions. For describing the interaction between Al-Co-Cr-Cu-Ni-Fe, we use EAM potential [6, 21, 23, 62]. Silicon Tersoff [4, 24-27] empirical potential is used for describing the interaction between Si-Si. In section 4.4.2, aiming to study the structure of HEA films in thickness, we reduce the size of the simulation box, the length in x and y direction is around 1/6 of those in section 4.4.1. The other settings in 4.4.2 are the same as 4.4.1. In section 4.4.3, we present the growth of HEA film with equimolar composition and its annealing behavior. In this case, we use Lennard-Jones potential for the interactions of the Si – (AlCoCrCuFeNi) and Cr - (AlCoCuFeNiSi), Silicon Tersoff empirical potential for describing the interaction between Si – Si and EAM potential for Al-Co-Cu-Fe-Ni.

4.4 Results and discussion

4.4.1 AlCoCrCuFeNi clusters growth onto silicon using potential of EAM

In this section, three MD simulations of AlCoCrCuFeNi HEA thin films with different element composition are made, according to the experiment. During MD simulation, 10000 atoms are released to the Si surface for realizing three deposition sets. A random number ζ is generated for selecting the nature of the atom to be released, where $0 \leq \zeta \leq 100$. Taking $\text{Al}_2\text{Co}_9\text{Cr}_{32}\text{Cu}_{39}\text{Fe}_{12}\text{Ni}_6$ as an example, Al is chosen if $0 \leq \zeta < 2$, Co if $3 \leq \zeta < 11$, Cr if $11 \leq \zeta < 43$ and so on. With this method the desired number of different atom types can be properly chosen according to the expected film composition. The output of simulation will inform about whether targeted composition is reached. Table 4.1 gives the number of atoms really living in the simulated film and its composition according to the experiment. The sticking coefficient is found close to 0.85 and the compositions of the simulated samples are close to the targeted ones.

Table 4.1 - Simulated deposited alloy composition

Atoms	Al	Co	Cr	Cu	Fe	Ni
Sample 1	$\text{Al}_2\text{Co}_9\text{Cr}_{32}\text{Cu}_{39}\text{Fe}_{12}\text{Ni}_6$ (8630/10000)					
Deposited number	151	956	2835	3211	1023	454
Simulation composition	1,7%	11,1%	32,9%	37,2%	11,9%	5,3%
Experiment composition	2%	9%	32%	39%	11%	6%
Sample 2	$\text{Al}_3\text{Co}_{26}\text{Cr}_{15}\text{Cu}_{18}\text{Fe}_{20}\text{Ni}_{18}$ (8466/10000)					
Deposited number	237	2154	1214	1550	1692	1619
Simulation composition	2,8%	25,4%	14,3%	18,3%	20,0%	19,1%
Experiment composition	3%	26%	15%	18%	20%	18%
Sample 3	$\text{Al}_{39}\text{Co}_{10}\text{Cr}_{14}\text{Cu}_{18}\text{Fe}_{13}\text{Ni}_6$ (8680/10000)					
Deposited number	2977	1084	1222	1688	1146	563
Simulation composition	34,3%	12,5%	14,1%	19,4%	13,2%	6,5%
Experiment composition	39%	10%	14%	18%	13%	6%

Sample simulation snapshots for $\text{Al}_2\text{Co}_9\text{Cr}_{32}\text{Cu}_{39}\text{Fe}_{12}\text{Ni}_6$, $\text{Al}_3\text{Co}_{26}\text{Cr}_{15}\text{Cu}_{18}\text{Fe}_{20}\text{Ni}_{18}$ and $\text{Al}_{39}\text{Co}_{10}\text{Cr}_{14}\text{Cu}_{18}\text{Fe}_{13}\text{Ni}_6$ thin films are reported in figure 4.3. In all cases, there is no continuous film growth and the deposits grow as various sizes clusters, more or less meandering, due to the limited number of impinging atoms and to the large cell size. The cluster mean height is around 3 ~ 3.5 nm for 10000 deposited atoms.

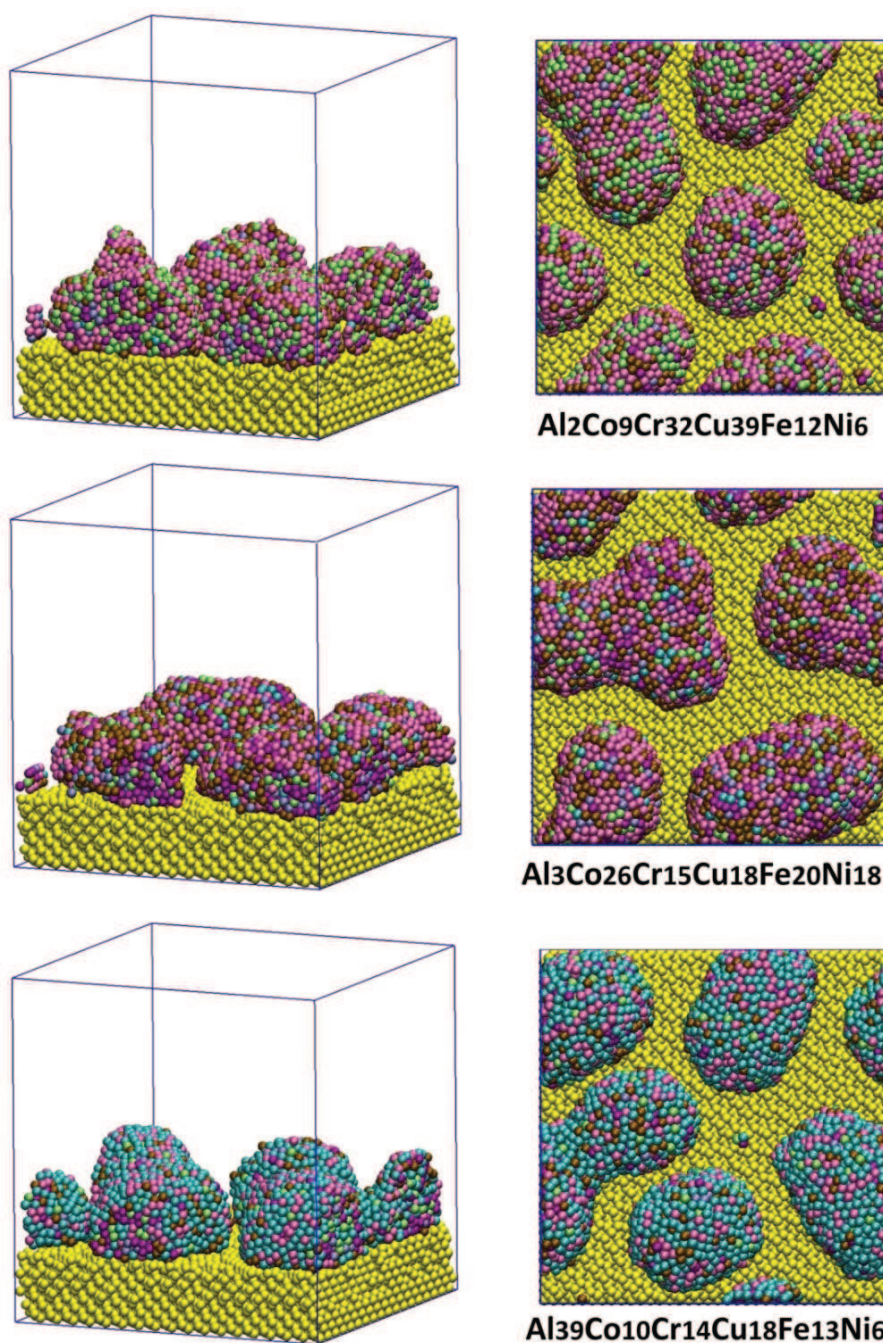


Figure 4.3 - snapshots of HEA films deposited on Si(100) substrate with large substrate ●Al, ●Co, ●Cr, ●Cu, ●Fe, ●Ni, ●Si

The RDF for the three samples was then calculated and plotted in Figure 4.4. The peaks represent the successive neighbor distances of the atoms, which can be compared with the corresponding values in crystalline phases of each element (see in table 4.2).

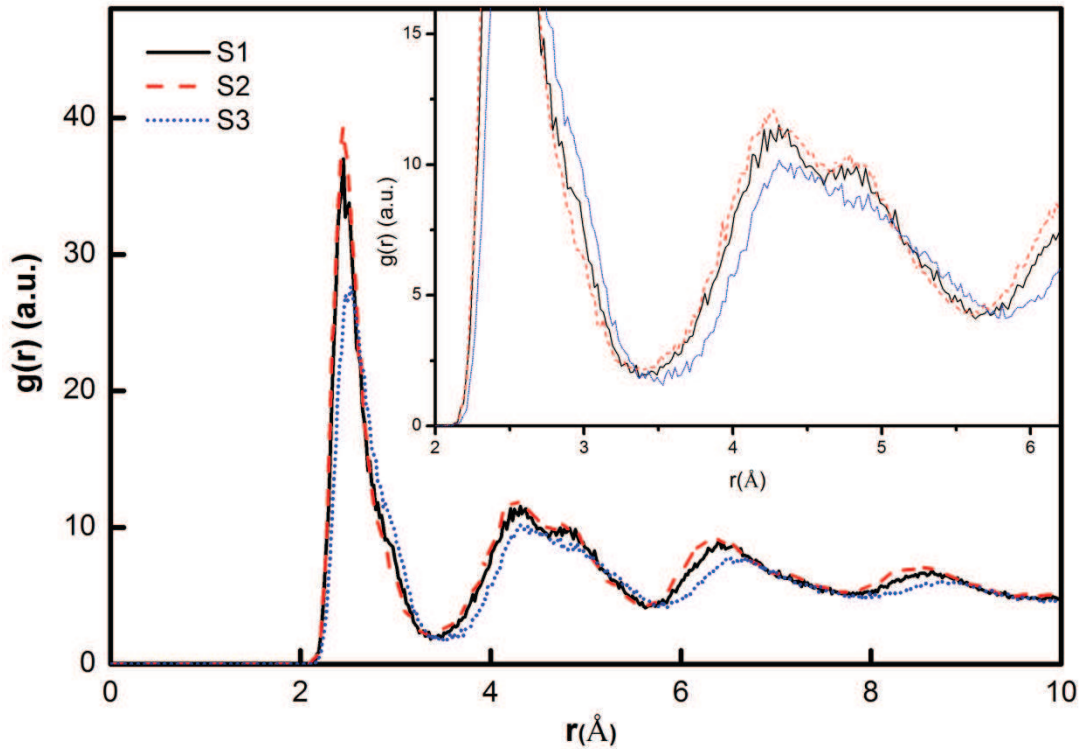


Figure 4.4 - Total RDF of the HEA deposit at different compositions.

Table 4.2 - the neighbor distances of HEA element crystal values.

Elements	Lattice parameter (Å)	1 st neighbor (Å)	2 nd neighbor (Å)	3 rd neighbor (Å)	4 th neighbor (Å)
Al (fcc)	$a_{Al} = 4.05$	$\frac{a_{Al}}{\sqrt{2}} = 2.86$	$a_{Al} = 4.05$	$\sqrt{\frac{3}{2}} a_{Al} = 4.96$	$\sqrt{2} a_{Al} = 5.73$
Co (hcp)	$a_{Co} = 2.51$ $c_{Co} = 4.07$	$a_{Co} = 2.51$	$\sqrt{2} a_{Co} = 3.09$	$c_{Co} = 4.07$	$\sqrt{2} c_{Co} = 5.76$

Cu (fcc)	$a_{Cu} = 3.61$	$\frac{a_{Cu}}{\sqrt{2}} = 2.55$	$a_{Cu} = 3.61$	$\sqrt{\frac{3}{2}} a_{Cu} = 4.42$	$\sqrt{2} a_{Cu} = 5.10$
Cr (bcc)	$a_{Cr} = 2.88$	$\frac{\sqrt{3}}{2} a_{Cr} = 2.49$	$a_{Cr} = 2.88$	$\sqrt{2} a_{Cr} = 4.07$	$\sqrt{\frac{11}{4}} a_{Cr} = 4.78$
Fe (bcc)	$a_{Fe} = 2.87$	$\frac{\sqrt{3}}{2} a_{Fe} = 2.49$	$a_{Fe} = 2.87$	$\sqrt{2} a_{Fe} = 4.06$	$\sqrt{\frac{11}{4}} a_{Fe} = 4.76$
Ni (fcc)	$a_{Ni} = 3.52$	$\frac{a_{Ni}}{\sqrt{2}} = 2.49$	$a_{Ni} = 3.52$	$\sqrt{\frac{3}{2}} a_{Ni} = 4.31$	$\sqrt{2} a_{Ni} = 4.98$

Table 4.3 - Average neighbor distances in the HEA.

Elements	1 st neighbor	2 nd neighbor	3 rd neighbor	4 th neighbor
$Al_2Co_9Cr_{32}Cu_{39}Fe_{12}Ni_6$ (average)	2.52	3.19	4.32	4.99
Sample1	2.44	-	4.27	4.79
$Al_3Co_{26}Cr_{15}Cu_{18}Fe_{20}Ni_{18}$ (average)	2.52	3.19	4.19	5.14
Sample2	2.45	-	4.30	4.83
$Al_{39}Co_{10}Cr_{14}Cu_{18}Fe_{13}Ni_6$ (average)	2.64	3.49	4.48	5.3
Sample3	2.46	-	4.35	-

As can be seen in table 4.3 the average values are calculated by $\overline{r_{neighbour}} = \sum_{i=1}^n c_i R_i$ according to the element crystal values presented in table 4.2, where c_i is the atomic percentage of the i^{th} component and R_i is the neighbor distances of i^{th} HEA element in pure crystal. By analyzing the average neighbor distances value of HEA in table 4.3, we can see that the first neighbor is almost constant in these three samples around 2.45 Å, the expected 2nd neighbor distance does not appear in the simulated thin film. This can be explained by the hard ball model [63] and attributed to the effect of mixing numerous elements with different atomic sizes as depicted in Figure 4.5. The circles represent the first, second, third, fourth and fifth shells, respectively. Because of the most compact system, the first shell will be stable or only change a little bit due to the presence of neighbor atoms with different atom radius.

However the second and third shells are indistinguishable because of the large fluctuation in occupation of different sites. This introduces the disappearance of the second peak in RDFs.

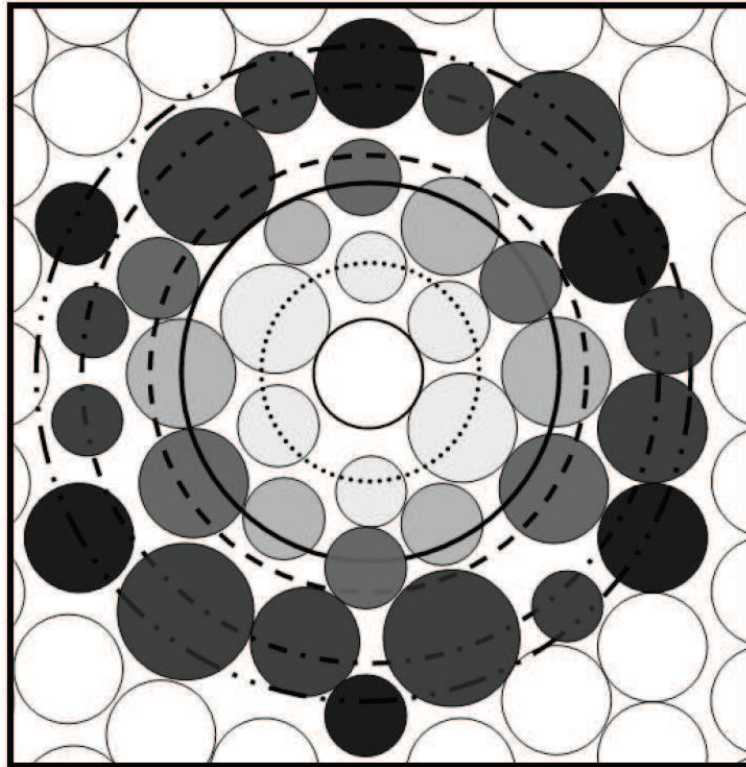


Figure 4.5 - Hard ball model for HEA

A further insight can be achieved by comparing the recorded XRD patterns with those calculated in the simulation. The experimental XRD θ - 2θ peaks are shown in figure 4.6 where the corresponding diffraction spectra (limited to the θ - 2θ range where the main peak of FCC and BCC phases lies) are given. The following peak positions are observed: $2\theta = 43.77^\circ$ for sample 3 and $2\theta = 43.81^\circ$ for sample 1 attributed to the $\text{fcc}(111)\beta$ structure, $2\theta = 44.41^\circ$ for sample 2 attributed to the $\text{bcc}(110)\alpha$ structure. However, the broad and low intensity sample 2 peaks could indicate a mixture of both solid solutions and a less ordered phase.

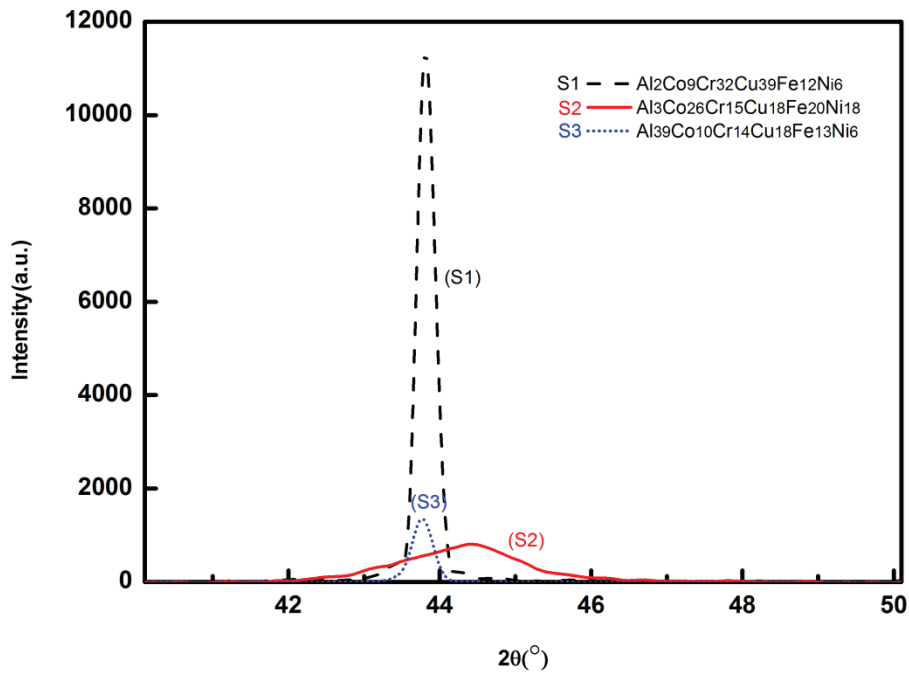


Figure 4.6 - Experimental XRD patterns of HEA film sputtered at 300 K with different compositions

The calculated X-ray intensities vs. 2θ of HEA samples are shown in figure 4.7. By comparing both XRD plot sets, it can be observed that the peak positions in the simulated XRD are close to that detected in the experimental XRD patterns (see table 4.4).

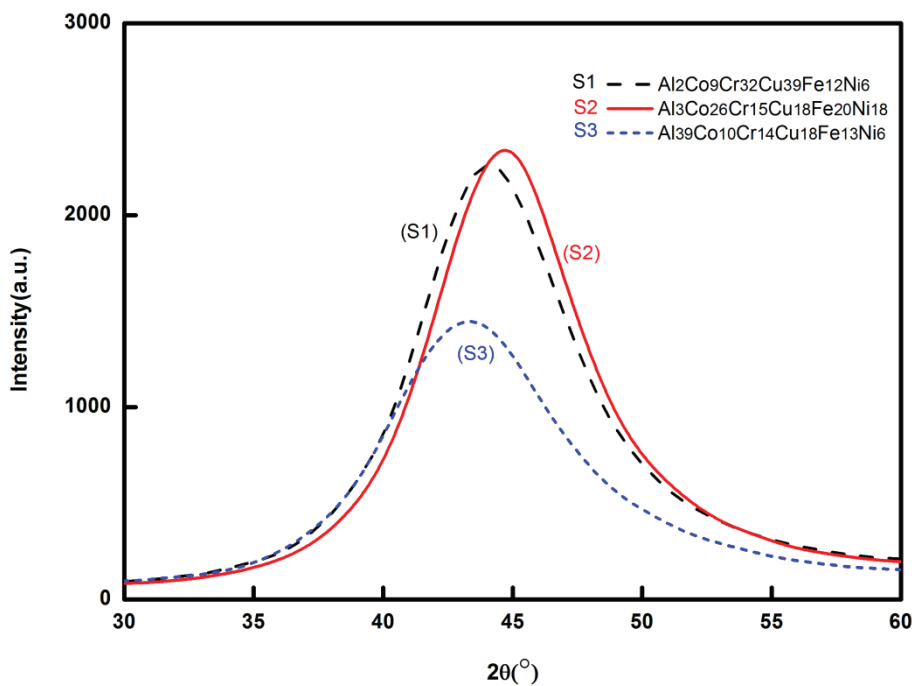


Figure 4.7 - The simulated XRD patterns at different compositions.

Table 4.4 - the 2θ position of first XRD peak for HEA in the experiment and simulation

Experiment		Unit: $2\theta(\text{deg})$	
HEA	$\text{Al}_{39}\text{Co}_{10}\text{Cr}_{14}\text{Cu}_{18}\text{Fe}_{13}\text{Ni}_6$	$\text{Al}_2\text{Co}_9\text{Cr}_{32}\text{Cu}_{39}\text{Fe}_{12}\text{Ni}_6$	$\text{Al}_3\text{Co}_{26}\text{Cr}_{15}\text{Cu}_{18}\text{Fe}_{20}\text{Ni}_{18}$
Main peak	43,77	43,81	44,41
Simulation		Unit: $2\theta(\text{deg})$	
HEA	$\text{Al}_{39}\text{Co}_{10}\text{Cr}_{14}\text{Cu}_{18}\text{Fe}_{13}\text{Ni}_6$	$\text{Al}_2\text{Co}_9\text{Cr}_{32}\text{Cu}_{39}\text{Fe}_{12}\text{Ni}_6$	$\text{Al}_3\text{Co}_{26}\text{Cr}_{15}\text{Cu}_{18}\text{Fe}_{20}\text{Ni}_{18}$
Main peak	43,95	44,1	44,7

As can be seen from figure 4.6 and 4.7, peak intensities are very different between simulations and experiments. This is due to the difference in layer thickness, thus to the total atom number. As already mentioned in chapter 3, the comparison can only be qualitative.

4.4.2 AlCoCrCuFeNi thin film deposition onto silicon with small size cell

In Section 4.4.1, we found that HEA clusters are formed after 10000 HEA atoms being released on the substrate. As we can expect, if we increase the number of the deposit atoms, we can get the morphology of a continuous film. It could be very interesting to study the feature of HEA films. While, with large size simulation box, more atoms are needed to be deposit in order to get the morphology of a continuous film, this will cost too much calculation time. Another method is to reduce the width of the box. In this section, based on the model in section 4.4.1, we reduce the width of the substrate cell to dimensions $(17 \times 17 \times 120)$ Å. The length in x and y direction is 1/6 of the previous size in section 4.4.1. In other words, if the same height is reached, the volume of the new simulation box is 1/36 of the previous size box.

The cutoff for both short and long range interactions is set to 8Å . The width of the system was chosen in a way that each dimension would be at least twice the cutoff. So boundary effects are expected to be limited. With this smaller width, if the velocity of deposited atom is too

large along x and y directions, it will pass through the periodic boundary several times. This will affect the whole system and may introduce artifact in the morphology. Figure 4.8 displays the trajectory of a typical Cu atom in the process of deposition in sample 1. The small blue balls and the blue line represent the history position of the Cu atom and trajectory separately. Each position has a small width 4ps and Cu atom can be captured by the nearby surface atoms with a fast relaxation. This trajectory shows that the model can be used for the MD simulation of HEA film growth without any effect of the periodic boundary condition for the smallest width.

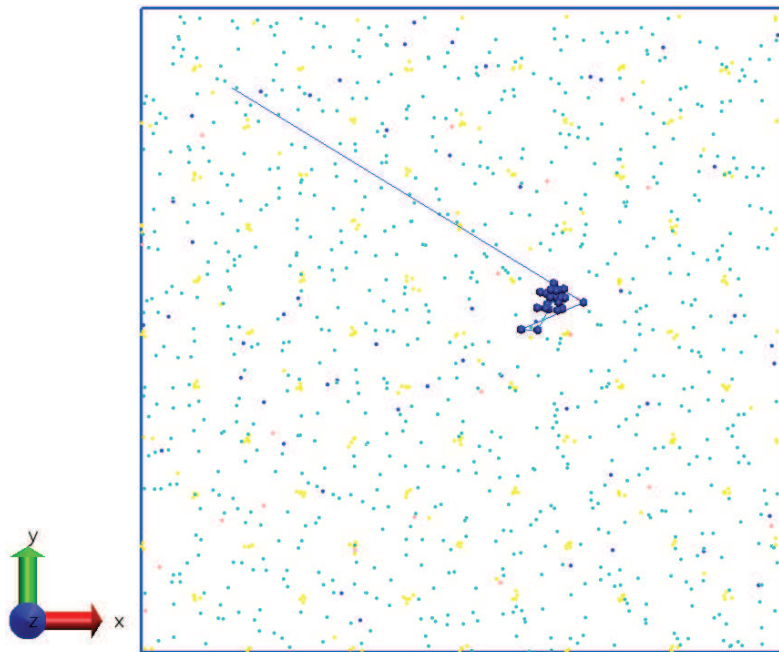


Figure 4.8 – projected Cu atom during deposition (cross section of the cell along z). Trajectory time elapsed between each position with a small width 4ps.

During MD simulation, 2000 atoms are released for realizing three deposition sets with the same compositions than in the experiment illustrated in section 4.4.2. These sets of calculation are equivalent to releasing 70000 atoms to the larger surface, so it is equivalent to observing the film at a deposition time approximately seven times larger. Table 4.5 gives the real composition of HEA thin film in the experiment (analyzed by EDS), the number of atoms really living in the simulated films and its composition.

Table 4.5 - Simulated deposited alloy composition in a small size cell

Atoms	Al	Co	Cr	Cu	Fe	Ni
Sample 1	$\text{Al}_2\text{Co}_9\text{Cr}_{32}\text{Cu}_{39}\text{Fe}_{12}\text{Ni}_6$ (1660/2000)					
Deposited number	37	165	523	643	189	103
Simulation composition	2,2%	9,9%	31,5%	38,7%	11,4%	6,2%
Experiment composition	2%	9%	32%	39%	11%	6%
Sample 2	$\text{Al}_3\text{Co}_{26}\text{Cr}_{15}\text{Cu}_{18}\text{Fe}_{20}\text{Ni}_{18}$ (1670/2000)					
Deposited number	59	456	250	282	313	310
Simulation composition	3,5%	27,3%	15,0%	16,9%	18,7%	18,6%
Experiment composition	3%	26%	15%	18%	20%	18%
Sample 3	$\text{Al}_{39}\text{Co}_{10}\text{Cr}_{14}\text{Cu}_{18}\text{Fe}_{13}\text{Ni}_6$ (1656/2000)					
Deposited number	634	186	218	305	208	105
Simulation composition	38,3%	11,2%	13,2%	18,4%	12,6%	6,3%
Experiment composition	39%	10%	14%	18%	13%	6%

The films grew to approximately 10 nm. Snapshots of the films with three different compositions deposited on Si (100) are presented in figures 4.9. It is clearly seen that a crystalline structure is formed in sample 1 and sample 2, which grow on a previously deposited amorphous HEA layer in section 4.4.1. While for sample 3, an amorphous structure is formed on the overall thickness.

Actually, throughout the process of atom deposition, there exist a competition between the dense packing (for lowering enthalpy) and the randomness of atoms (for increasing configurational entropy and $T\Delta S$) driven by thermal energy. In each step during simulation, each jumping atom or in-situ shaking is to seek its minimum-energy position under the rule of minimizing energy. But, at the same time, the kinetic energy or momentum also drives atoms

to jump, which is against the tendency towards the minimum energy. With the same simulation conditions, the “engine” of this competition, enthalpy and entropy, is determined by the only varied parameter, the composition of the HEA. In sample 1 and 2, the dense packing becomes dominant in making the atomic configuration more ordered. In contrast, sample 3 a disordered or amorphous phase tends to stabilize. This can be interpreted as the high-entropy effect.

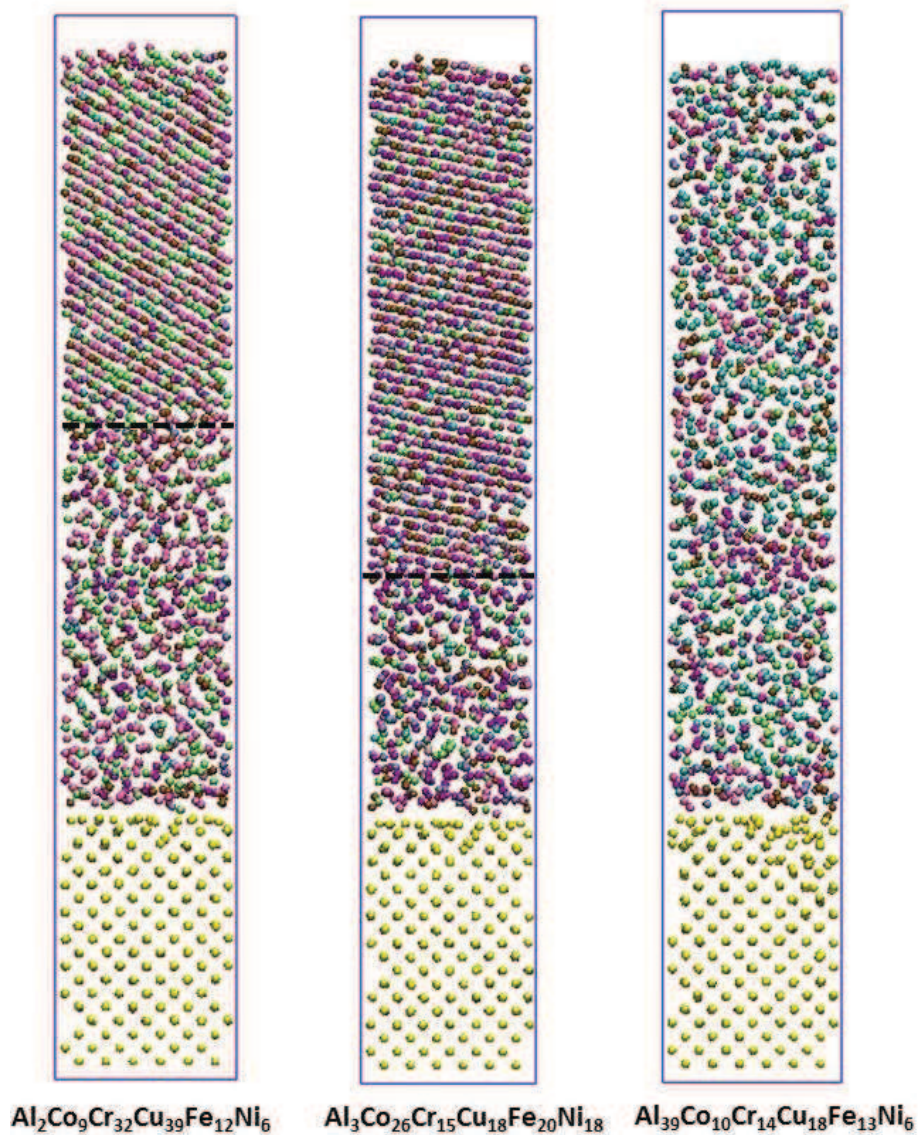


Figure 4.9 - Snapshots of HEA films deposited on Si(100) substrate with small substrate, the dashed line separate the crystalline structure and amorphous. ● Al, ● Co, ● Cr, ● Cu, ● Fe, ● Ni, ● Si

Figure 4.10 shows the RDF of the three samples and table 4.6 gives the 4 simulated neighbor distances and the corresponding average values of the element crystal. In these three samples, the disappearance of the second neighbor distance coincided with the HEA simulations given above and is introduced by the disorder arrangement of atoms preventing stacking order to grow. In sample 1 and 2, the RDFs show outstanding peaks that can be attributed to a crystalline structure, in agreement with the results presented in Figure 4.9. In sample 3, it is shown that the general intensity of RDF is lower, besides, the first and second peaks become broad and fading away quickly. All of this depicts that sample 3 exhibits a low ordered structure. This is also in agreement with the snapshot of sample 3 in Figure 4.9. From a comparison among RDF patterns in figure 4.10 versus 4.4, it is seen that, as the continuous film growth, the RDF patterns change very little for alloys of sample 3 showing amorphous state but significantly for sample 1 and 2. For the continuous film the first fourth peaks becomes clearer and narrower and the fifth peak around 7.36 Å arises, showing the crystal-like structure formed.

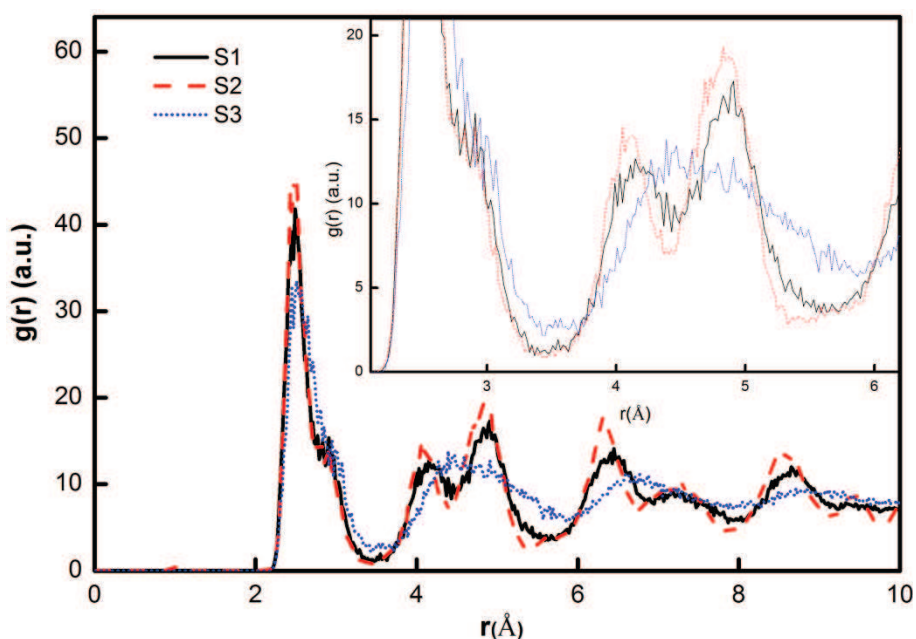


Figure 4.10 - Total RDF of the HEA deposits at the different compositions of figure 4.9

TABLE 4.6 - Average neighbor distances in the HEA compared to element crystal values.

Elements	1 st neighbor (Å)	2 nd neighbor (Å)	3 rd neighbor (Å)	4 th neighbor (Å)
Al ₂ Co ₉ Cr ₃₂ Cu ₃₉ Fe ₁₂ Ni ₆ (average)	2.52	3.19	4.32	4.99
Sample1	2.48	-	4.08	4.83
Al ₃ Co ₂₆ Cr ₁₅ Cu ₁₈ Fe ₂₀ Ni ₁₈ (average)	2.52	3.19	4.19	5.14
Sample2	2.49	-	4.15	4.88
Al ₃₉ Co ₁₀ Cr ₁₄ Cu ₁₈ Fe ₁₃ Ni ₆ (average)	2.64	3.49	4.48	5.3
Sample3	2.52	-	4.42	-

Figure 4.11 shows the intensity of the calculated X-ray intensities vs. 2-θ of HEA samples. The number of atoms in this set of simulation is low, thus it is hard to get XRD pattern corresponding to the experiment. To circumvent this, we have repeated 25 times the original HEA, according to the periodic boundary condition in x and y direction. A system with around 50000 atoms was built for calculating more precisely the XRD patterns. The peak positions are shown in table 4.7.

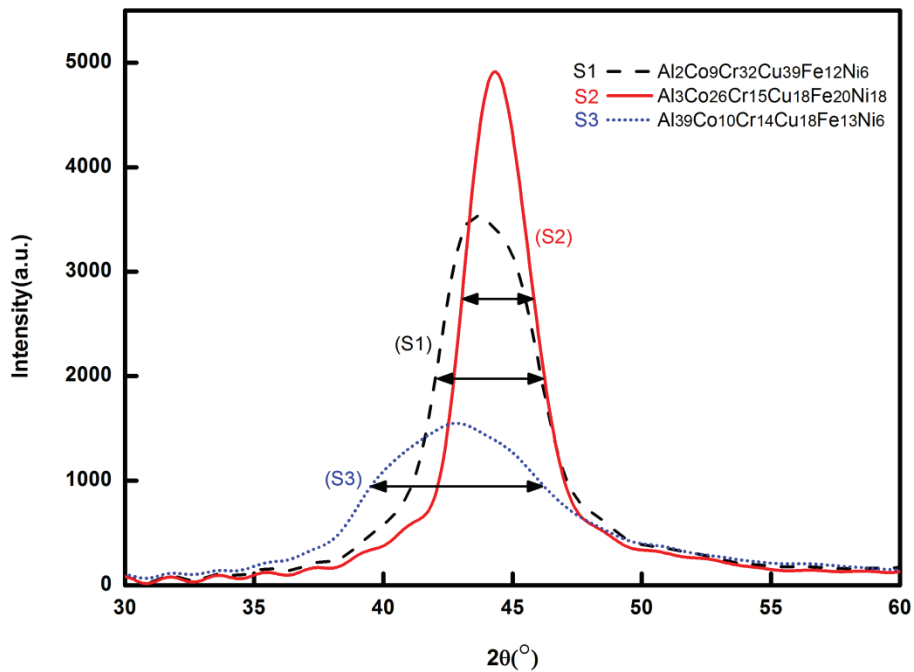


Figure 4.11 - the simulated XRD patterns at different compositions.

The simulated peaks at position $2\theta = 42.85^\circ$, 43.6° and 44.3° correspond to sample 3, 1 and 2, respectively. These values are close to the experiment, with a small shift towards smaller angles. That may be caused by the limited size of the simulation box. Besides, with the same number of the deposited atoms, the peak of sample 3 is broader than the others. This corresponds to the amorphous structure shown in figure 4.7. On the contrary, sample 1, 2 have the thin and narrower peaks and the well crystallized structure arises with thickness around 4 nm and 5 nm respectively in figure 4.7. It seems that the width of the simulated XRD peak is proportional to the amorphous or crystallized phase in the simulation. Due to limited number of atoms in the simulation compared to experiment, the comparison can only be qualitative.

One has to keep in mind that the other atoms in the expanded film are just the duplication of the same unit, this is the limitation of this model. Nevertheless, we can use this procedure to get some information about the crystalline or amorphous nature of the films, depending on the composition of the HEA and to compare with the experiment. What is interesting in using small cells is to study the structure in the thickness.

Table 4.7 - the 2θ position of main XRD peak for HEA alloy in the experiment and simulation

Experiment		Unit: $2\theta(\text{deg})$		
HEA	$\text{Al}_{39}\text{Co}_{10}\text{Cr}_{14}\text{Cu}_{18}\text{Fe}_{13}\text{Ni}_6$	$\text{Al}_2\text{Co}_9\text{Cr}_{32}\text{Cu}_{39}\text{Fe}_{12}\text{Ni}_6$	$\text{Al}_3\text{Co}_{26}\text{Cr}_{15}\text{Cu}_{18}\text{Fe}_{20}\text{Ni}_{18}$	
main peak	43,77	43,81	44,41	

Simulation		Unit: $2\theta(\text{deg})$		
HEA	$\text{Al}_{39}\text{Co}_{10}\text{Cr}_{14}\text{Cu}_{18}\text{Fe}_{13}\text{Ni}_6$	$\text{Al}_2\text{Co}_9\text{Cr}_{32}\text{Cu}_{39}\text{Fe}_{12}\text{Ni}_6$	$\text{Al}_3\text{Co}_{26}\text{Cr}_{15}\text{Cu}_{18}\text{Fe}_{20}\text{Ni}_{18}$	
main peak	42,85	43,6	44,3	

Furthermore, we use solid-solution formation rules detailed in section 2.5 referred to ZHANG et al [17, 30, 49, 50] to characterize the collective behavior of the constituent elements in the multi-component alloys. The parameters of the three samples defined for MD simulations

were calculated and are listed in table 4.8 and mapped in figure 4.12 [30]. Figure 4.12 shows the relationship between parameters δ and Ω for these three samples according to figure 2.5 in chapter 2. As shown in figure 4.12 and table 4.8, the values of δ (2.28%, 2.89%) and Ω (2.794, 38.986) of sample 1 and 2 lies in the scope of “Solid Solutions” where the formation of solid solutions is predicted. Sample 3 with $\delta = 5.94\%$ and $\Omega = 2.595$, stays in the overlap area of “Solid Solutions” and “Intermetallics”, which indicates both solid solutions and intermetallics are likely to be formed. From sample 2, 1 to sample 3, it can be seen that there is a tendency to them from solid solution to bulk metallic glasses. This is in agreement with figure 4.9 where the crystallized part of the film is the highest for sample 2, decreases for sample 1 and completely disappears in sample 3. Even if these rules proposed by ZHANG applied for the equilibrium synthesis techniques, e.g. bulk metal synthesis techniques, it is hard to get exact predictions for non-equilibrium synthesis techniques, like magnetron sputter deposition. Nevertheless, it can be used for qualitative predictions .

Table 4.8 - the microstructure and the parameters, δ , ΔH_{mix} , ΔS_{mix} , T_m and Ω for investigated HEAs

	δ (%)	$\Delta H_{\text{mix}}(\text{KJmol}^{-1})$	$\Delta S_{\text{mix}}(\text{KJ}^{-1}\text{mol}^{-1})$	$T_m(\text{K})$	Ω	Structure
Sample 1	2.28%	7.445	12.188	1706.835	2.794	S
Sample 2	2.89%	0.619	13.994	1723.433	38.986	S
Sample 3	5.94%	-7.415	13.525	1423.049	2.595	S+I

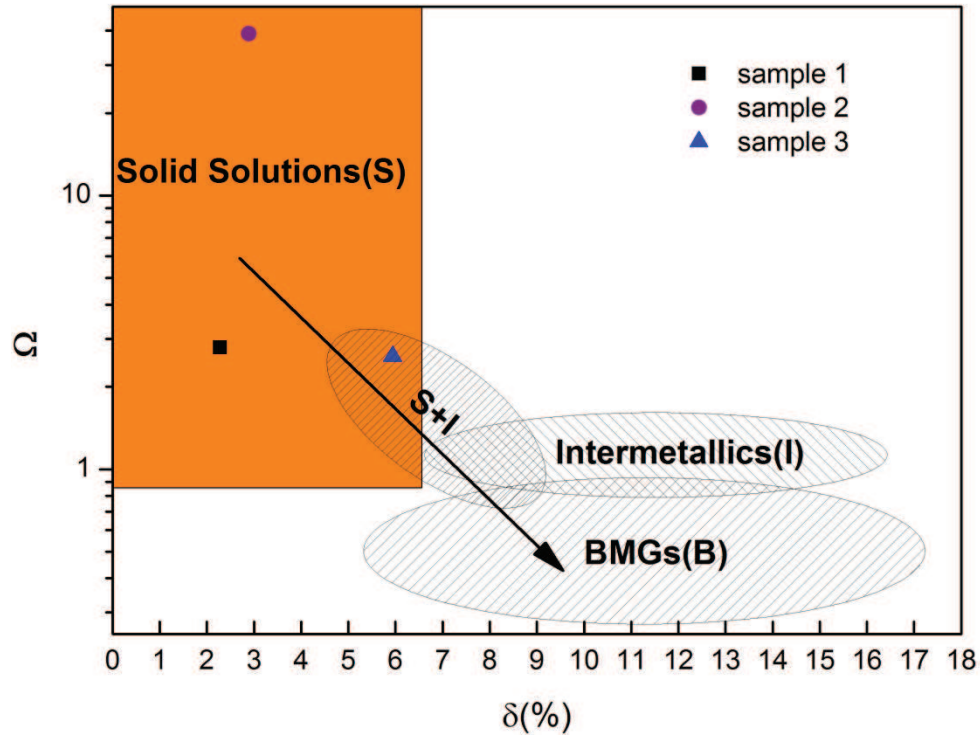


Figure 4.12 - The relationship between parameters δ and Ω for three samples with small substrate

4.4.3 AlCoCrCuFeNi thin film deposition and annealing onto silicon using hybrid of EAM and Lennard-Jones potentials

In this section, we use MD simulation studying growth and thermal stability, in the range 300-1500 K, of a AlCoCrCuFeNi high entropy (HEA) alloy thin film. It contains an equal molar ratio of Al, Co, Cu, Cr, Fe and Ni. In this simulation, 10000 atoms are released for realizing the deposition of equimolar HEA clusters. A random number ζ is generated for selecting the nature of the atom to be released. Al is chosen if $0 \leq \zeta < 1/6$, Co if $1/6 \leq \zeta < 2/6$, and so on. This means 1666 atoms of each kind of element are launched. Table 4.9 gives the number of atoms really living on the surface. The total number of deposited atoms is 7866, leading to a total sticking coefficient close to 0.80. As a previous work, No EAM potential was found for Cr interactions with other metals at that time, so the Al-Co-Cu-Fe-Ni interactions are modelled with the Embedded Atom Method (EAM) force field, the Cr-(AlCoCuFeNiSi) and Si-(AlCoCrCuFeNi) interactions are modeled with Lennard-Jones (12-6) potential and the Si-Si interaction with the Tersoff potential.

TABLE 4.9 – Simulated deposited alloy composition

Atoms	Al	Co	Cu	Cr	Fe	Ni
Deposited number	1309	1205	1293	1357	1348	1354
Sticking coefficient	0.78	0.72	0.77	0.81	0.81	0.81
The ratio of the element (ζ)	16.6%	15.3%	16.4%	17.3%	17.1%	17.2%

The final composition is thus $\text{Al}_{16.5}\text{Co}_{15.5}\text{Cu}_{16.5}\text{Cr}_{17.2}\text{Fe}_{17.1}\text{Ni}_{17.2}$, which is close to equimolarity where atomic percentage of each element should be 16.67%. The configuration of the deposited HEA cluster is shown in figure 4.13.

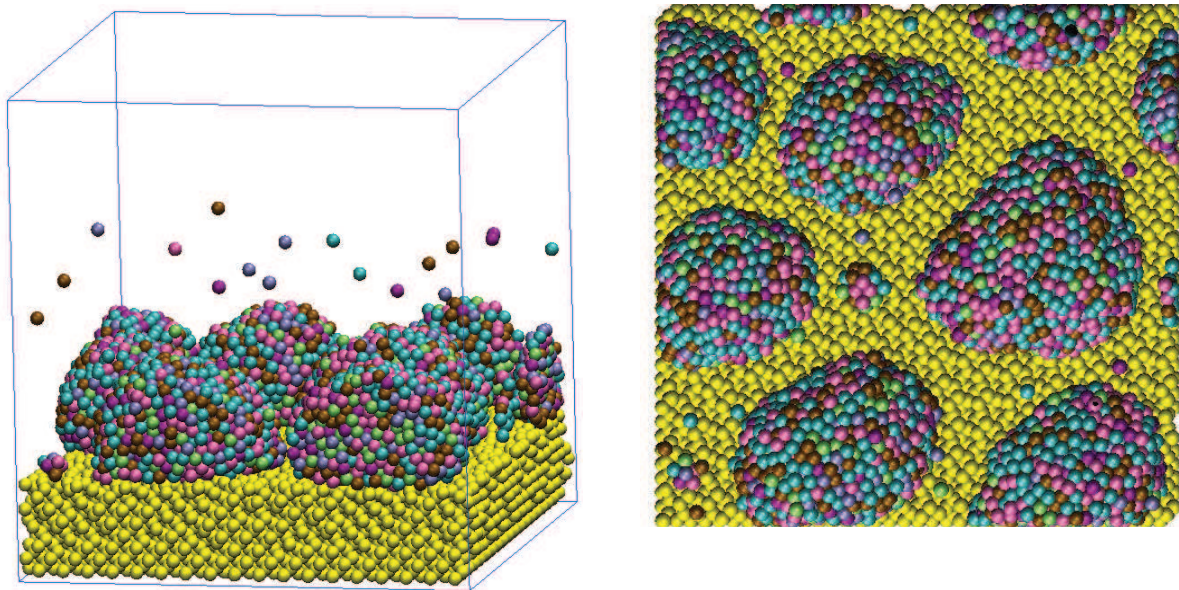


Figure 4.13 Side and top views of snapshot of the simulated deposited HEA film. ● Al, ● Co, ● Cr, ● Cu, ● Fe, ● Ni, ● Si

The film grows as clusters of various sizes: single atoms and very small clusters lie between larger ones with sizes 25-30 Å. Due to the limited number of impinging atoms (10000) a continuous film is not reached. Nevertheless, this brings the opportunity to explore the behavior under annealing of this cluster assembly.

The annealing process of AlCoCrCuFeNi high-entropy alloy being the second stage of the whole process, it is performed in the same simulation box. Once HEA thin film was deposited

on the Si (100) surface of Silicon substrate, the annealing simulation was started. The bottom two layers of the substrate remain fixed as for the deposition step, while the others are temperature-controlled layers at temperature (from 300K to 1500K), as well as the supported HEA clusters. The important parameter is the temperature increase rate. We have run simulations with 2K/ps, 1K/ps and 1K/3ps annealing rates. The resulting root mean square displacements (RMSD) of these three different rates are plotted in figure 4. 14. At a rate 1K/3ps, the lowest one, we do not observe any change on the RMSD of the deposited atoms as compared to 1K/ps. It means that further decreasing the annealing rate, i.e. increasing the time to reach the targeted temperature, does not change the cluster dynamics. So using 1K/3ps will reflect the correct annealing behavior. RMSD evolution at 1K/3ps exhibits a first region up to 1050 K, with a slow increase. At 1050 K a sharp increase is observed, followed by increasing stepped evolution.

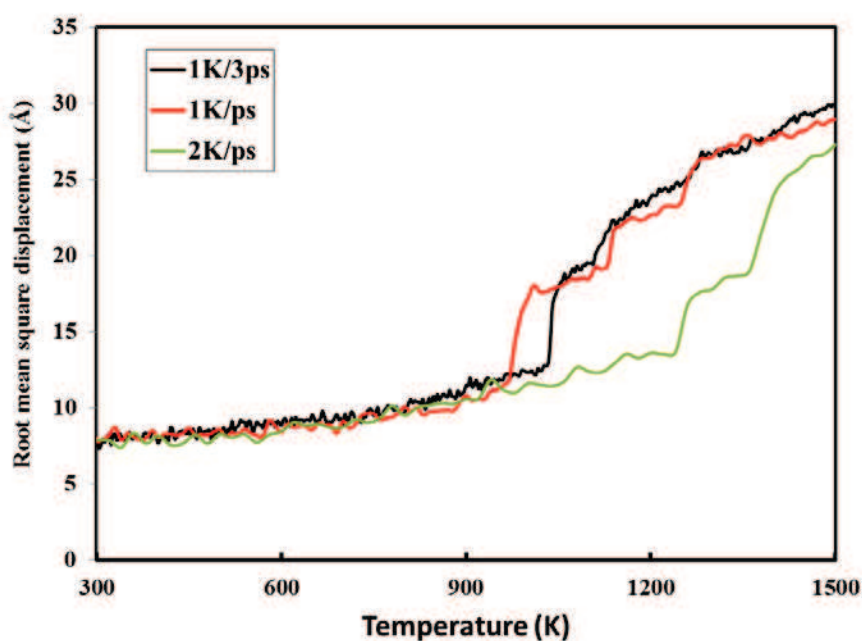


Figure 4.14 - Evolution of the total root mean square displacement against the temperatures at various annealing rates

Examination of the top snapshots, as displayed in figure 4.15, at different temperature shows a coalescence phenomenon due to temperature induced mobility; the first step is the capture of

smallest clusters (figure 4.15, images at 500K and 800K) which has almost no effect on the RMSD, since nothing is observed on Figure 4.14 in this temperature range.

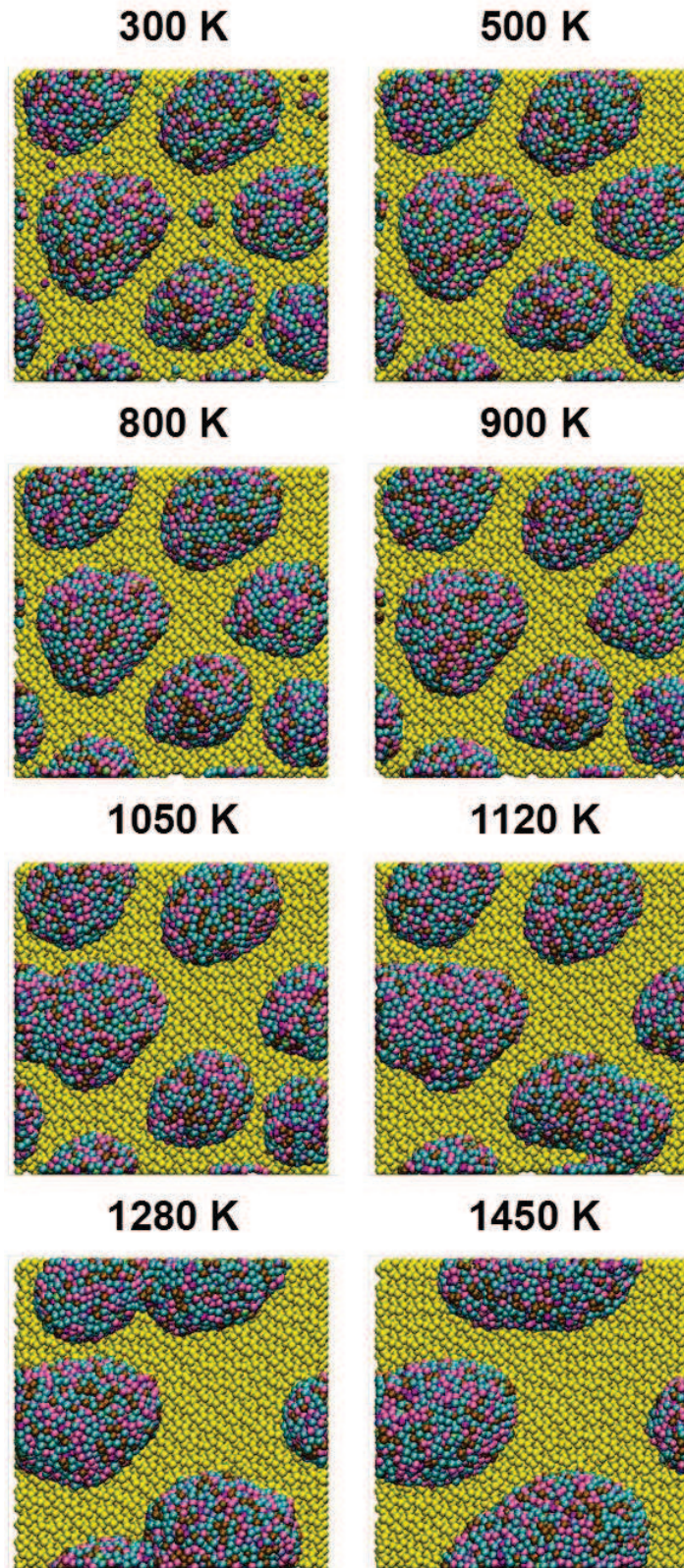


FIGURE 4.15 - Successive snapshots of simulated annealing process at different temperatures.

● Al, ● Co, ● Cr, ● Cu, ● Fe, ● Ni, ● Si

On the other hand, the first capture of a large cluster occurs at a temperature of 1050 K which corresponds to the beginning of the jump in the RMSD (figure 4.14). This is a starting step of the cluster fusion. From this temperature the individual atoms are also starting to move inside a hosting cluster, which also contributes to the jump in the RMSD. The coalescence of large clusters corresponds to the slight steps above 1050 K in the RMSD plot. Below 1050 K the atoms are only vibrating, with a more or less large magnitude.

The magnitude of vibration rises when increasing the temperature, as it can be observed on figure 4.16 which displays the trajectory of a typical Cr atom. As can be seen between 300 and 600K, the atom is locally vibrating: displacements are short and a small domain is visited. Around 600K, there is a small jump and local motion with a slightly larger magnitude up to 800K. This defines a second domain of motion but with a slightly larger size. Between 800 and 1050 K, the travelled distance continues to grow up but the motion remains local. Above 1050 K, the atom has larger displacements and between 1200 and 1380 K the local character starts to be lost. Above 1380 K the atom makes the largest displacements and a domain cannot be easily defined.

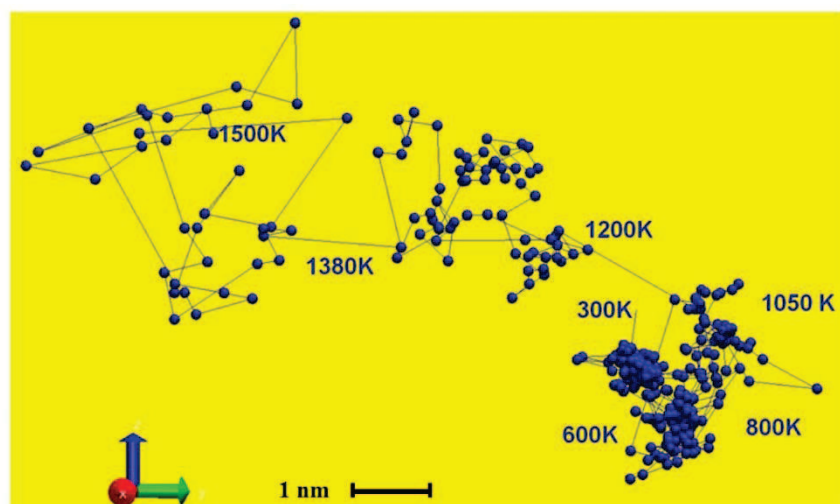


Figure 4.16 - Trajectory of typical Cr atom during annealing. Each point of the trajectory is separated by 3.3 K i.e. 10 ps.

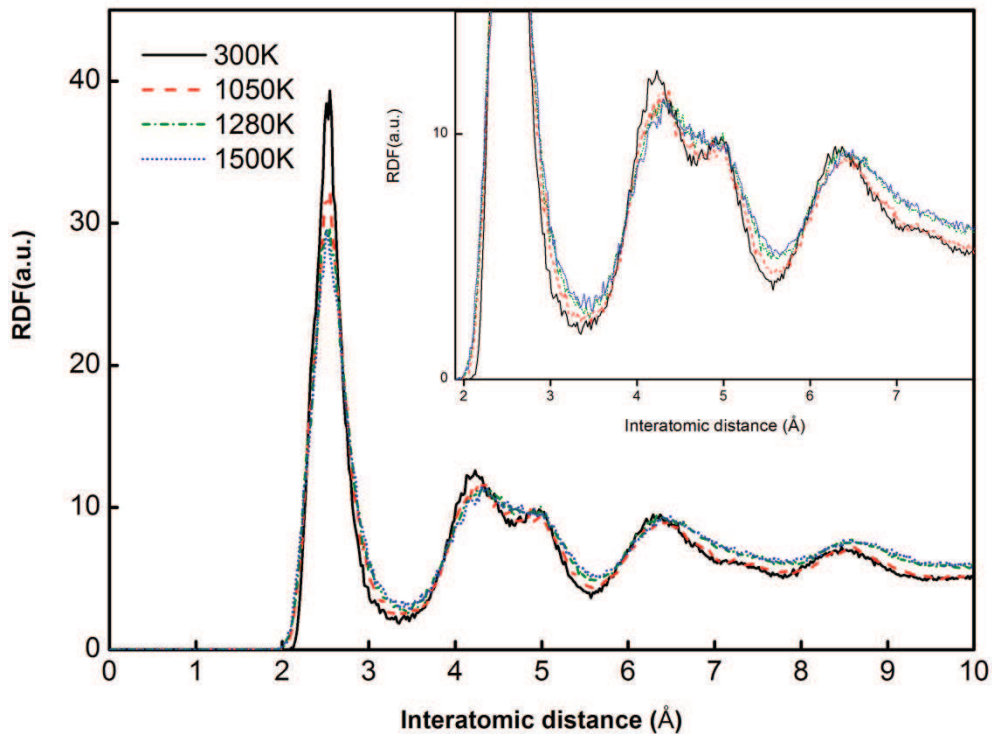


Figure 4.17 - Total RDF of the HEA deposit at different annealing temperatures.

The total RDF is plotted in figure 4.17 for four temperatures: 300, 1050, 1280, and 1500 K. The peaks represent the successive neighbor distances in the deposit film. This can be compared with the corresponding averaged values in crystalline phases of each element (see table 4.2 and table 4.10).

TABLE 4.10 - Average neighbor distances in the HEA compared to element crystal values.

Elements	1 st neighbor	2 nd neighbor	3 rd neighbor	4 th neighbor
AlCrCuFeNi (average)	2.56	3.34	4.32	5.19
HEA T = 300 K	2.525	-	4.225	4.975
HEA T = 1050K	2.525	-	4.325	5.025
HEA T = 1280 K	2.525	-	4.375	4.975
HEA T = 1500 K	2.525	-	4.275	4.925

As can be seen in table 4.10, nearest neighbor distances of the HEA are different from the element ones and from averaged values. The most important difference is the disappearance

of the expected 2nd neighbor distance. This can be explained by recalling that 2nd neighbors in such crystal structures are in the neighboring plane. Lack of this peak should be representative of some disorder preventing stacking order to grow. This is consistent with the apparent random distribution of atoms within the clusters (see figure 4.14 and 4.15). Moreover the slightly different atomic sizes can also contribute to prevent ordered stacking of parallel layers as in the perfect crystal. In the monoatomic case, this ordered layer growth only occurs on flat substrate [64]. On atomically disordered surfaces, there is no expected 2nd neighbor. This is consistent with the previously discussed hard ball model. Because the larger radius difference in the system, the second and third shells, and also the fourth and fifth shells in hard ball model become indistinguishable, which introduce the disappearance for the second peak. As the RDF gives the number of atoms located at a given distance, the global analysis of figure 4.17 shows that the first neighbor peak is reduced when increasing temperature and the tail at long distances is higher for temperatures greater than 1050 K. This is consistent with the increase of RMSD also above 1050 K. Increasing atom number located at larger interatomic distances means that the correlation distance is increased as in a more fluid state.

Examination of table 4.10 shows that interatomic distances are always contracted, whatever the temperature is, as compared to the average values of the bulk states of the elements. A relative dilatation also occurs for 1050 and 1280 K. Only the 1st peak is unchanged during annealing and lies below the average bulk value. We cannot attribute the peak position to the effect of specific elements.

Furthermore, similar as the previous section 4.4.1 and 4.4.2, we use solid-solution formation rules to characterize the collective behavior of the constituent elements in the equal-mole HEA alloy (AlCoCrCuFeNi). The parameters are calculated and listed in table 4.11 and the values of δ (4.82%) and Ω (5.06) lies in the same scope “Solid Solutions” like sample 1 sample 2 in

previous section. While, it displays similar behaviors by comparing the RDF patterns in figure 4.17 at room temperature (300K) and those of sample 1 and sample 2. The peak of expected 2nd neighbor distance also disappears and peaks of the first, third and fourth neighbor distance are clear. This implies that the usage of LJ potential of Cr-(AlCoCrCuFeNi) instead of EAM potential does not have too much effect on the whole system.

Table 4.11 - the microstructure and the parameters, δ , ΔH_{mix} , ΔS_{mix} , T_m and Ω for investigated HEAs

	δ (%)	$\Delta H_{\text{mix}}(\text{KJmol}^{-1})$	$\Delta S_{\text{mix}}(\text{KJ}^{-1}\text{mol}^{-1})$	$T_m(\text{K})$	Ω	Structure
Sample 1	4.82%	-4.78	14.90	1622.25	5.06	S

A further insight can be achieved by calculating the XRD patterns at different annealing temperatures. Figure 4.18 displays the evolution of the calculated HEA patterns. This is calculated with the same method described in section 4.4.2 by duplicating the original cell according to its boundary conditions.

It can be observed

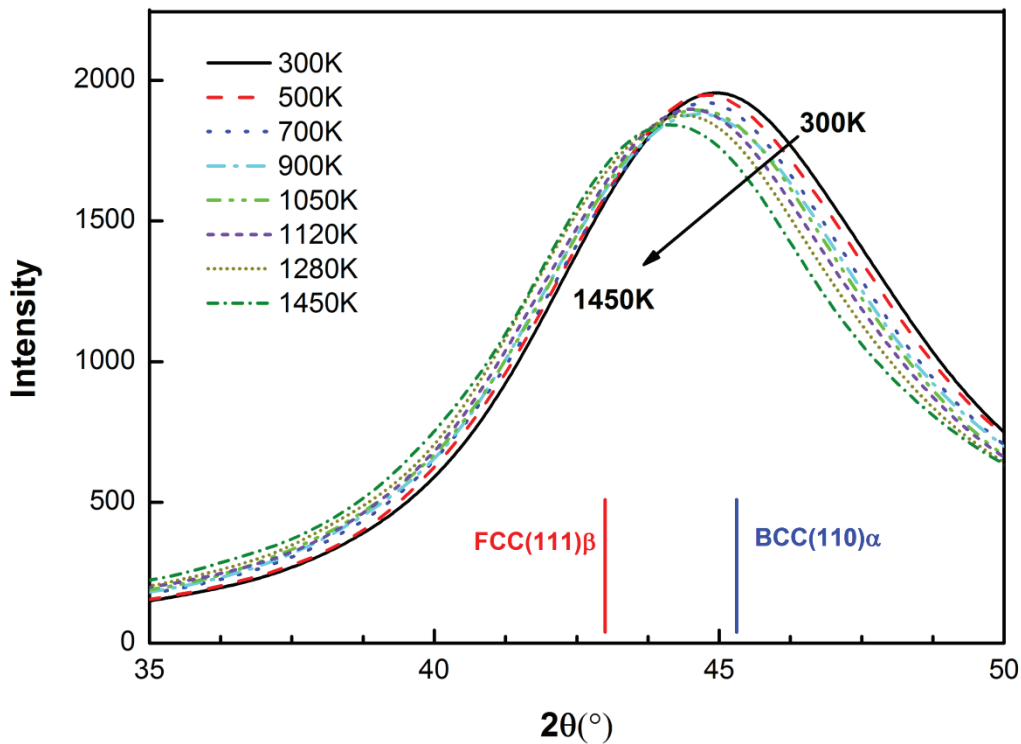


FIGURE 4.18 - The simulated XRD patterns at different annealing temperatures. The two tags at 43 and 45° refer to the experimentally observed FCC and BCC peak values (see ref. 12).

that the peak position 2θ is shifted from 45° at 300K to 44° at 1450K. As report in ref. [61], the XRD patterns are twofold at 300K: one small peak at 42.8° attributed to the fcc(111) β solid solution which coexists with a larger one located at 44.8° attributed to the bcc(110) α one. When increasing the temperature, experiment shows that the fcc peak increases in magnitude at the expense of the bcc one and moves to lower position: 43° at 1100 K, with complete disappearance of the bcc(110) α peak. Our simulated XRD patterns are consistent with these results: the peak is too large for being resolved as a two XRD peak pattern, but the shift towards lower values of simulated peak positions indicates the same trend of phase evolution, bcc towards fcc. It is difficult to have more resolution on the simulated XRD pattern due to the small sized layer/clusters, which give rise to broad peaks. The estimated fcc lattice parameter from the present MD simulations is 3.64 Å and the bcc one is 2.86 Å (see table 4.12), which compares very well with both experiment (3.66 Å and 2.86 Å, respectively) [61]

and bulk calculations (3.60 Å and 2.87 Å, respectively) [65, 66]. The mean cluster size issued from MD simulations is around 25 Å at 300K and 50 Å at 1450K. This is enough for obtaining an XRD pattern, but not for resolving fcc and bcc peaks, which are experimentally observed.

Table 4.12 - Experimental and calculated lattice parameters a. $2d_{hkl} \sin(\theta) = \lambda$ (1.54 Å) and

$$d_{hkl} = \frac{a}{\sqrt{h^2 + k^2 + l^2}}.$$

Lattice parameters a	Bulk (calculated) [65, 66]	Experiment thin films [61]	Present work
fcc phase	3.60 Å	300 K 3.66 Å 1100 K 3.64 Å	300 K 3.64 Å
bcc phase	2.86 Å	300 K 2.86 Å 1100 K none	1100 K 2.89 Å

4.5 Conclusions

In this chapter, MD simulations are carried out for describing initial growth of HEA thin films and its' annealing onto silicon. In the simulation of HEA film growth, these alloys were found to possess fcc/bcc structure affected by the composition of their elements which is corresponding to the experiment. By statistically analyzing the parameters δ and Ω for reported HEAs, a tendency to evolve from solid solution to bulk metallic glasses was found, which can be used to assist in qualitative predictions of phase for the HEAs with chemical composition varied.

MD simulation reports growth of clusters which evolve during the annealing step from 200K to 1500K. The induced cluster coalescence is observed to be accompanied by a fusion-like process. This is starting around 1050 K where individual atoms are moving inside the clusters leading to a jump in the total RMSD. Moreover XRD calculations at different annealing temperatures show the transition between HEA bcc phase to HEA fcc phase in agreement

with experiment. Besides, the composition of HEA is a critical factor affecting the structure and this was evidenced and compared to the experiment. By calculating parameters of δ and Ω for the typical multi-components HEA with different composition, a solid-solution formation relationship has been referred and evidenced. Agreement between experimental and simulated XRD patterns proves that modeling at the atomic level allows predicting the structure found in the experiment.

Chapter 5: Molecular dynamics simulations of platinum atom deposition onto nanostructured carbon

Dans ce chapitre, nous utilisons les simulations de dynamique moléculaire pour étudier l'évolution structurale et dynamique d'atomes de platine déposés sur des substrats carbonés nanostructurés (réseau de nanotubes de carbone (CNT) et de carbone poreux, respectivement). Nous examinons comment les conditions de dépôts tels que la nature du substrat de carbone nanostructuré, l'énergie cinétique des atomes incidents et le potentiel d'interaction entre le platine et le carbone, sont le moteur de la croissance des agrégats.

Le dépôt par pulvérisation cathodique d'atomes de platine sur deux substrats carbonés nanostructurés a été étudiée par simulations de dynamique moléculaire à la température ambiante (300 K) et comparée à deux ensembles de paramètres possibles du potentiel Lennard-Jones Pt-C pour trois différentes distributions d'énergie cinétique des atomes Pt incidents. Lorsque l'on considère la croissance des agrégats sur les nanotubes de carbone, l'emplacement des agrégats le long des CNT dépend de l'énergie cinétique: lorsque l'on augmente l'énergie cinétique, les agrégats sont placés de plus en plus profondément vers la base de nanotubes de carbone. La morphologie est également affectée: lorsque l'énergie augmente les agrégats sont plus cristallisés comme prévu. Il n'y a pas de différence significative entre les deux potentiels d'interaction utilisés en ce qui concerne la morphologie du cluster sur CNT. Dans les deux cas des agrégats cristallisés sont obtenus. Cela est probablement dû au substrat cristallisé qui semble piloter la croissance.

La situation est très différente sur le carbone poreux où le potentiel 1 moins liant avec la surface conduit à des agrégats mieux cristallisés. Cela provient de l'énergie de cohésion du Pt qui est assez élevée par rapport à l'énergie de liaison de surface pour "ignorer" les détails de la surface. Au contraire lors de l'utilisation du potentiel 2 plus liant avec la surface, le Pt s'adapte étroitement à la morphologie de la surface et conduit à un film plus bi-dimensionnel. La structure cristalline persiste en partie, en raison de la faible épaisseur.

5.1 Introduction

Physical and electronic properties of metal nanoparticles deposited on various substrates have recently received a great deal of attention. In catalysis, metal nanoparticles, often platinum, are used in reactions such as selective hydrogenation [67], oxidation of formic acid and formaldehyde [68], and, in reactions such as oxygen reduction occurring in fuel cells [69-71]. Usually, these nanoparticles are supported by nanostructured substrates, among them carbon nanotubes (CNTs), porous carbon or carbon nanofibers (CNF) [72]. Due to the high cost of platinum, it is necessary to keep the Pt nanoparticles well deposited and dispersed in the nanostructured carbon support to avoid the agglomeration of Pt nanoparticles over time which will lead to the loss of surface area and activity [73]. Lee et al. [74] reported that the Pt cluster size distribution was a function of Pt loading and the average cluster size increased as the Pt loading increased. Clark and Kesmodel [75] studied that very small Pt clusters migrate during scattering from one place to another to form a more stable and larger cluster. Lee et al. [74]

reported that the size mobile clusters had a maximum around the cluster diameter of 14 nm. Many efforts are directed at optimizing catalytic performances, which in turn requires a substantial understanding of the Pt-substrate interactions and of the relationships between common feature of the Pt atom deposition method, e.g. the varying controlled kinetic energy of deposit atoms and activity of the nanocatalysts.

In this chapter, we use MD simulations to investigate the structural and dynamical evolution of platinum atoms deposited on nanostructured carbon substrates (carbon nanotube array and porous carbon, respectively). By performing MD simulation, we intend to examine how deposition conditions such as the nature of the nanostructured carbon substrate, the kinetic energy of incoming atoms and the interaction potential between platinum and carbon, are driving the clusters growth.

5.2 Computational details

MD simulations were carried out in a three dimensional cell, which was periodic only along x and y directions. Two different nanostructured carbon substrates are used in these simulations. The first substrate is a Carbon Nanotube (CNTs) with height 5.5 nm and the diameter of 2 nm vertically centered on a $4 \times 4 \text{ nm}^2$ graphite support. Due to periodic boundary conditions in x and y directions, it mimics a CNT square array. The second is a realistic model of porous carbon obtained by applying a constrained reverse Monte-Carlo procedure to a set of high resolution transmission electron microscopy pictures [76]. The model substrate has $6 \times 6 \times 6 \text{ nm}^3$ dimensions, with 8520 atoms leading to a density of $0.79 \text{ g}\cdot\text{cm}^{-3}$. The porosity is thus 65%. The schematic of the substrates are presented in figure 5.1.

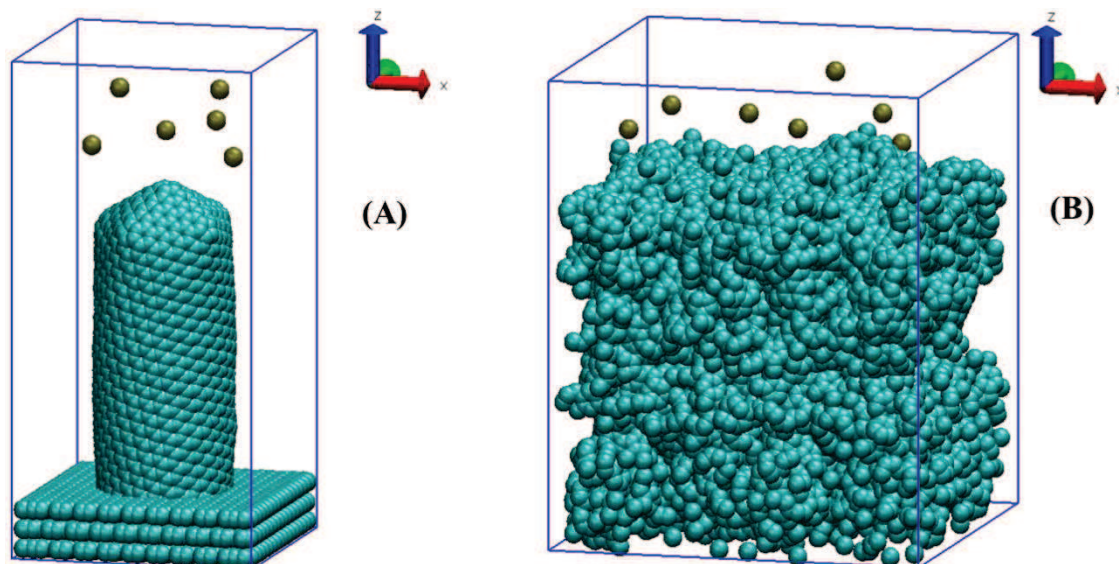


Figure 5.1 - Substrate (A) is Carbon Nanotube array; Substrate (B) is the reconstructed porous carbon piece, ●C and ●Pt

Each platinum atom are randomly released towards the substrate every $\Delta t = 2$ ps above the surface. All the Pt atoms interact with other platinum atoms and with the nanostructured carbon substrate atoms within a cutoff distance around 8 \AA . The deposition process is detailed in section 2.2.2. The velocities of the incoming Pt atoms are sampled from a Maxwell-Gaussian distribution with three most probable energies of 1 eV, 0.1 eV and 0.026 eV (300 K) with random corresponding incident angles. Carbon atoms are moving consistently with 300 K surface temperature. The mean kinetic energy of incoming atoms is calculated according to the modification of Thompson formula for atom travelling a plasma [28, 29] over a defined target to substrate distance. The mean kinetic energy being 1 eV, it simulates sputtering experiments at low argon pressure where a small amount of buffered gas only randomizes sputtered atom velocities without not too much energy loss. When at 0.1 eV, it is also consistent with resistive or e-beam evaporation, which produces a vapor at the vaporization temperature, which just lies in the range 0.1 eV and plasma sputtering at pressure around 2 Pa. The last case with the energy of 0.026 eV, it simulated a metal vapor at the temperature of 300 K which occurs when sputtered Pt atoms travel across argon plasma at pressure around 5 Pa. The temperature of the substrate in the simulation is assumed to be 300 K which

corresponds to the substrate value in temperature controlled experiments. For each considered system, a Berendsen thermostat, as described in section 2.2.1, was added to the nanostructured carbon substrate for energy dissipating to keep the film and substrate temperatures around 300K. The substrate carbon atom interactions are modeled by a Tersoff potential (see 2.1.4). For describing the interaction between Pt-Pt, we use EAM potential [18-22]. The platinum – carbon interactions were modeled using a 12-6 LJ. We use two different sets of LJ parameters in our simulations. The first set of LJ parameters (Potential 1) was derived by fitting at Pt-C using Sutton Chen Pt-Pt and Steele C-C interactions [77-79]. The Pt–C parameters were then obtained from the Pt–Pt ones using C–C parameters and the Lorentz–Berthelot mixing rules [80], which resulted in $\sigma_{\text{PtC}} = 2.905 \text{ \AA}$ and $\epsilon_{\text{PtC}} = 0.02206 \text{ eV}$. The second set of parameters (Potential 2) was obtained by Morrow and Alberto Striolo [81] from Acharya et al. [82], who performed DFT calculations to determine the binding energy of one Pt atom at various sites on graphite. The data were used to generate a potential energy surface, which was fitted by Lennard-Jones interaction potential. According to this parameterization, the LJ parameters are $\sigma_{\text{PtC}} = 1.60 \text{ \AA}$ and $\epsilon_{\text{PtC}} = 0.1365 \text{ eV}$.

In this chapter, potential 1 is used to model the interaction between Pt – C on carbon nanotube arrays. Whereas for platinum atom deposition on porous carbon, we performed the simulations with both potentials. The parameters of two sets of LJ potential for Pt – C are summarized in table 5.1.

Table 5.1 – LJ parameters used to describe Pt – C pair interaction

	ϵ (eV)	σ (Å)
Potential 1	0.02206	2.95
Potential 2	0.1365	1.60

5.3 Result and discussion

5.3.1 Platinum atom deposit on carbon nanotube array

Sample simulation snapshots for platinum atoms deposited on CNT are presented in figure 5.2 for the three Pt atom MB kinetic energy distributions of 1.0 eV, 0.1 eV and 0.026 eV. Deposition of Pt leads to cluster growth on different part of CNTs according to the kinetic energy distribution. Pt clusters are formed at the bottom of CNTs for 1eV energy. The medium energy distribution leads to the clusters formed in the middle part of CNTs while formed at the tip of CNTs with lowest energy 0.026eV. This comes from the Pt diffusion which is enhanced by increasing the incoming kinetic energy combined with the weak interaction potential between Pt and CNTs. So growth can occur at different distances from the CNT tip along the wall. Moreover, for the 1.0eV energy distribution, the Pt atoms have enough energy to migrate and merge together to form a large cluster on the bottom of CNTs. On the contrary, with the lower energy of 0.026eV, the incoming Pt atom stays at the tip of CNTs when landing. While for the medium energy of Pt depositing atoms, the Pt cluster is formed in the middle part of CNTs due the balance of the week absorption from CNTs and the limited kinetic energy leading to lower diffusion.

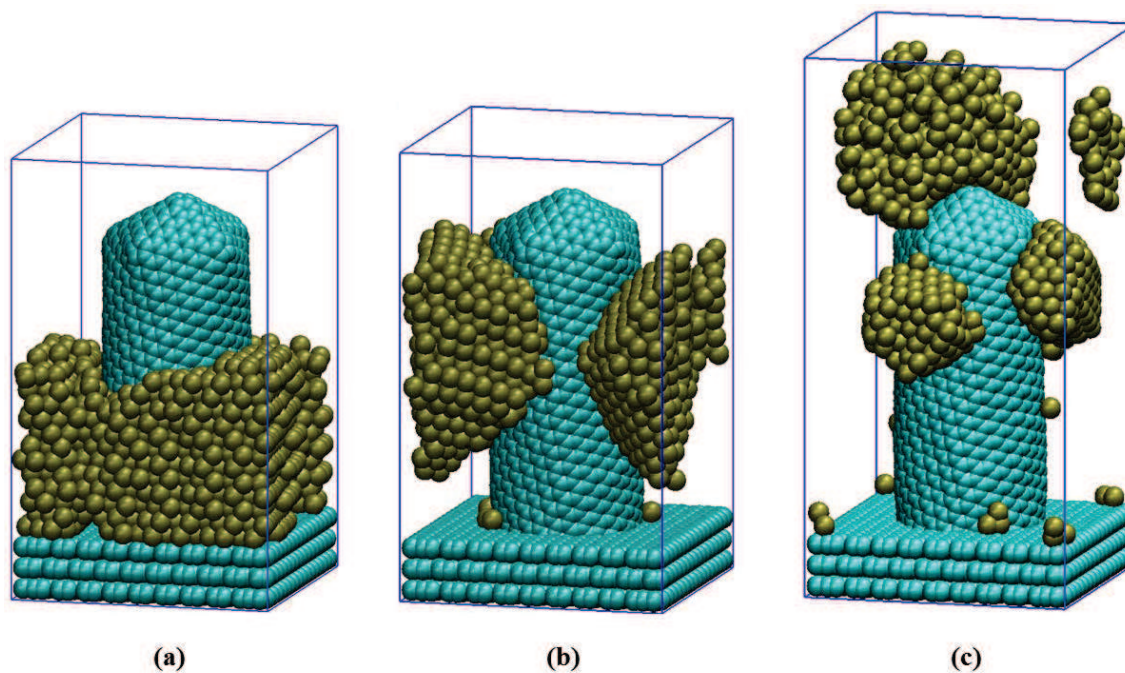


Figure 5.2 - Schematic picture of Pt deposit on CNTs. (A) Pt energy with 1 eV, (B) Pt energy with 0.1 eV and (C) Pt energy with 0.026 eV. ● C and ● Pt

These changes of the Pt clusters in the simulation were quantified by calculating a RDF which provides structural information of the deposits. Figure 5.3 shows the RDFs of Pt cluster with the deposited energy of 1.0 eV, 0.1 eV and 0.026 eV respectively.

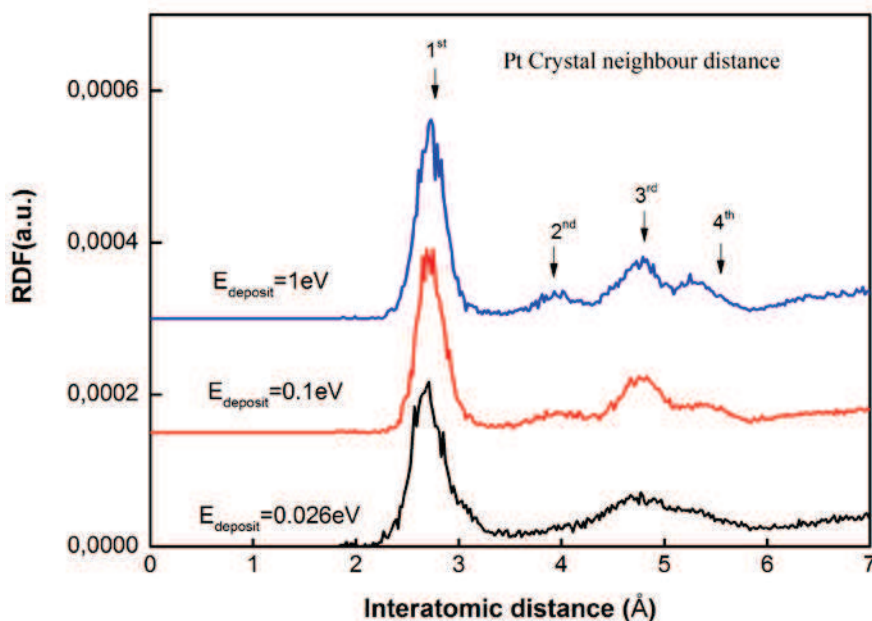


Figure 5.3 – The RDF of the Pt clusters deposit on CNTs for the 3 energy distributions.

At high mean kinetic energy (1.0 eV), the calculated RDF exhibits four outstanding peaks and the peak positions are corresponding to four nearest neighbor distance of Pt crystal (table 5.2).

Table 5.2 – Five nearest neighbor distances of platinum crystal, lattice constant $a_0=3.9239 \text{ \AA}$
RDFs peaks position of Pt deposit on CNTs

	1 st neighbor (\AA)	2 nd neighbor (\AA)	3 rd neighbor (\AA)	4 th neighbor (\AA)	5 th neighbor (\AA)
distance(\AA)	$a_0/\sqrt{2}$	a_0	$\sqrt{3/2}a_0$	$\sqrt{2}a_0$	$\sqrt{3}a_0$
number of neighbor	12	6	24	4	8
Pt crystal value	2.7746	3.9239	4.8058	5.5492	6.79
Pt-1eV	2.73	3.99	4.81	5.32	-
Pt-0.1eV	2.72	4.03	4.79	5.44	-
Pt-0.026 eV	2.72	-	4.78	-	-

This means that structure is ordered. This is also observable from the corresponding snapshot in figure 5.2 (a). Similarly, the RDF at 0.1eV energy distribution also has four peaks with nearly identical peak positions. But the peaks are less sharp which is indicating the structure is less crystallized than in the case of 1.0eV. For 0.026eV energy distribution, the RDF is different, the first peak broadens and the second, third and fourth collapse into a broad single one which means that ordering of Pt clusters is no more well established. This is in agreement with the observation of figure 5.2 (c) where clusters forming on the top of CNT exhibit a disordered structure.

To further characterize the Pt cluster structure, we calculated the XRD patterns of the simulated systems. Figure 5.4 shows the intensity of the XRD θ - 2θ peaks as a function of the Pt depositing energy. By comparing XRD plot with standard platinum crystal XRD pattern figure 5.5, it can be observed that in all cases, the simulated XRD have three peaks Pt(111),

Pt(200) and Pt(311) and there is a little shift in the peak position because of the smaller simulation box (detailed in table 5.3). While for each case, as the Pt energy change from 1 eV to 0.026 eV, the peaks of Pt(200) and Pt(311) are broadening and becoming halo peaks. This indicates that Pt cluster changed from crystal to less ordered structure in agreement with the corresponding RDF in figure 5.3 and morphologies in 5.2.

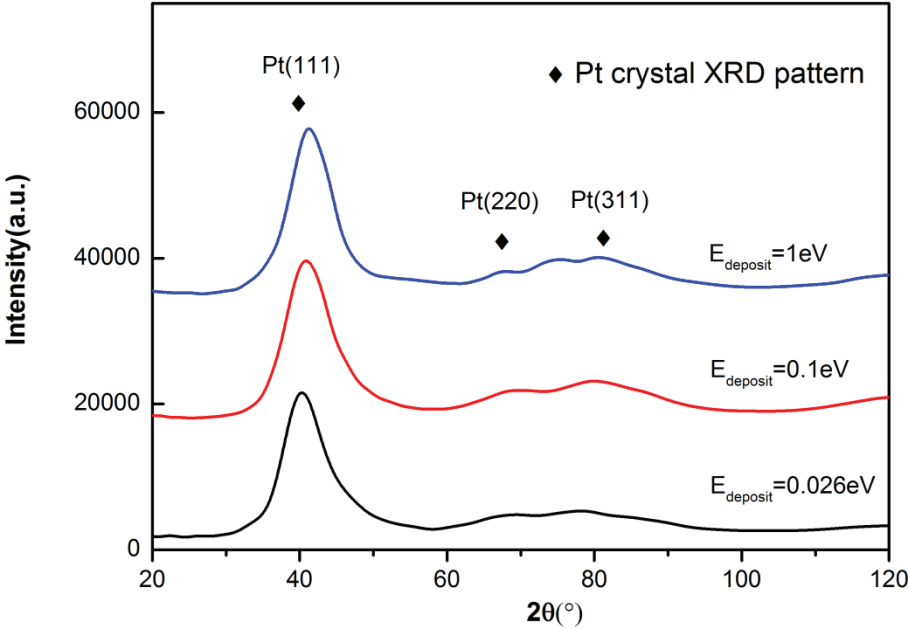


Figure 5.4 - X-Ray intensity vs. 2θ of Pt-cluster deposit on CNTs with different

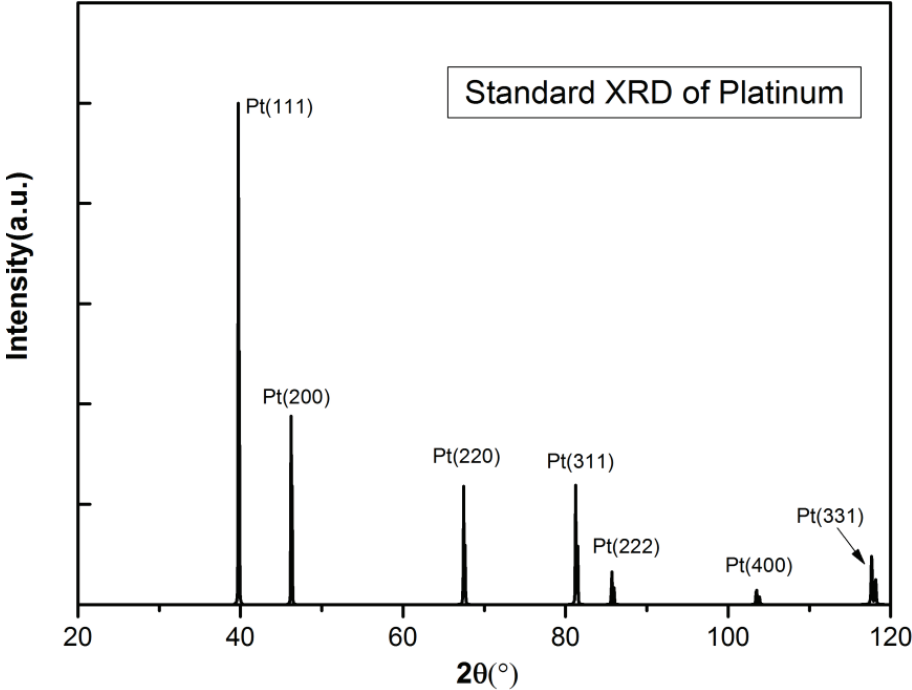


Figure 5.5 - XRD patterns of the bulk Pt crystal

Table 5.3 - the 2θ position of XRD peak for standard Pt crystal and Pt cluster in the MD simulation

Standard Pt crystal

Unit: 2θ ($^{\circ}$)

Pt	Pt(111)	Pt(200)	Pt(220)	Pt(311)	Pt(222)	Pt(400)	Pt(331)
Peak position	39.75	46.25	67.45	81.25	85.7	103.5	118.15

Pt cluster in MD simulations

Unit: 2θ (deg)

Pt	Pt(111)	Pt(200)	Pt(220)	Pt(311)	Pt(222)	Pt(400)	Pt(331)
Pt 1.0 eV	40.78	-	68.96	81.45	-	-	-
Pt 0.1 eV	41.15	-	67.42	80.81	-	-	-
Pt 0.026 eV	40.43	-	69.31	78.31	-	-	-

When comparing these calculations with those corresponding to potential 2 [22,23], the cluster morphologies are identical. This indicates that the effect of the bonding of the potential 2 does not play a significant role in the cluster morphology and structure for Pt deposition on CNTs.

5.3.2 Platinum atom deposit on porous carbon with Pt - C LJ potential

In this section, platinum atom deposit onto the porous carbon with the L-J potential 1. On figure 5.6 are plotted snapshots for Pt atoms deposit with three different energies: 1eV, 0.1eV and 0.026eV. In all cases, Pt cluster deposit on porous carbon exhibit more crystallized structure than those deposited on CNTs in section 5.3.1. As the depositing energy of platinum decreased from 1 eV to 0.026eV, the morphology of Pt cluster changed from one spherical-like cluster, to one peanut-like cluster and to several small clusters, respectively.

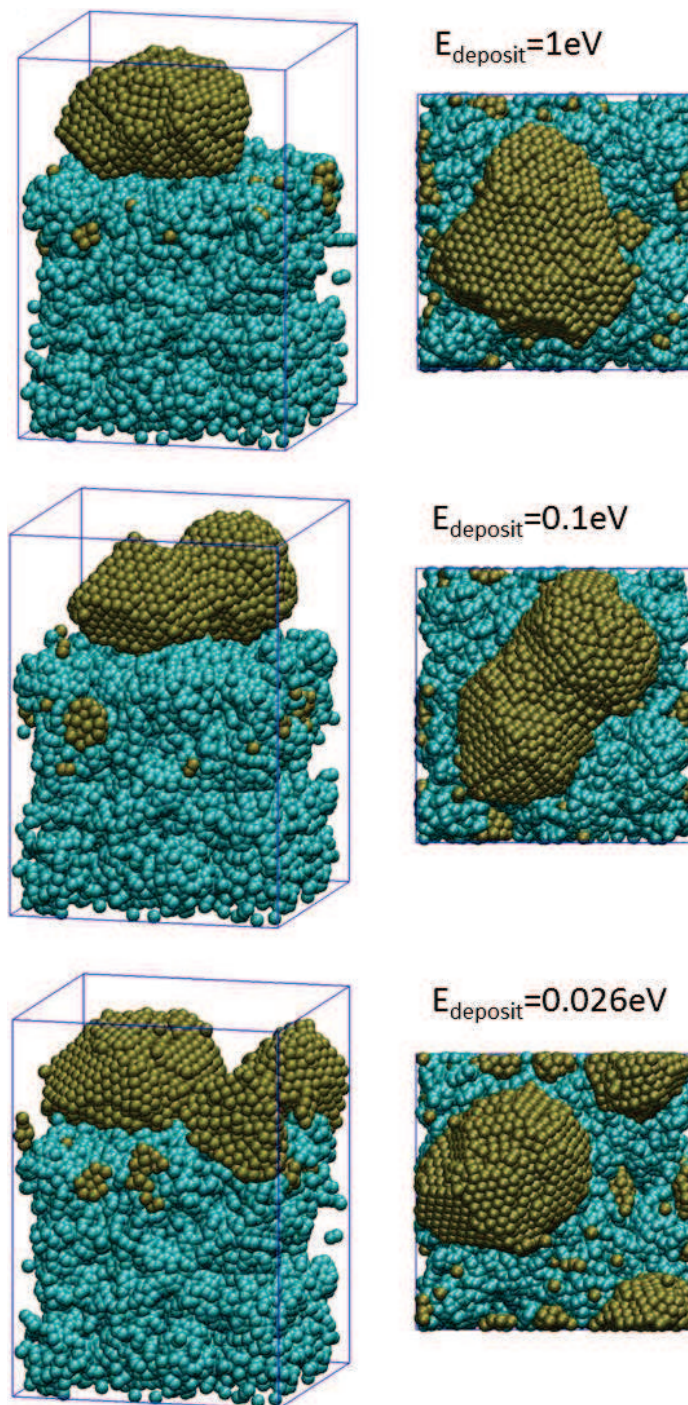


Figure 5.6 - Schematic picture of Pt deposit on porous carbon with potential 1. ●C and ●Pt

The RDFs of Pt clusters in these growth simulations are plotted in Fig. 5.7 at the three depositing energy. It can be noticed that the RDF at 1.0eV shows the sharper and higher peaks and the position of the five nearest neighbors is recovered (see table 5.5), indicating that Pt clusters exhibit a very well defined crystal structure. This confirms the view of the corresponding snapshot in figure 5.6. At the lower energies, 0.1 eV and 0.026 eV, the RDFs

also have five peaks showing the crystalline structure is remaining, however, the intensity of the peaks are lowered compared to the highest energy, especially the second and fifth peaks. Moreover they become broader, which depicts a less ordered structure when comparing to growth at 1eV. This is slightly different than for Pt deposition on CNTs, where the disorder is more pronounced at low energy. This is rather surprising because the CNT substrate being more ordered one could guess a better ordering on CNT than on porous disordered carbon.

Table 5.4 – RDFs peaks position of Pt deposit on porous carbon with potential 1

	1 st neighbor (Å)	2 nd neighbor (Å)	3 rd neighbor (Å)	4 th neighbor (Å)	5 th neighbor (Å)
Pt crystal value	2.7746	3.9239	4.8058	5.5492	6.79
Pt-1ev	2.74	3.92	4.79	5.51	6.24
Pt-0.1ev	2.74	3.95	4.78	5.44	6.25
Pt-0.026ev	2.74	3.96	4.78	5.48	6.28

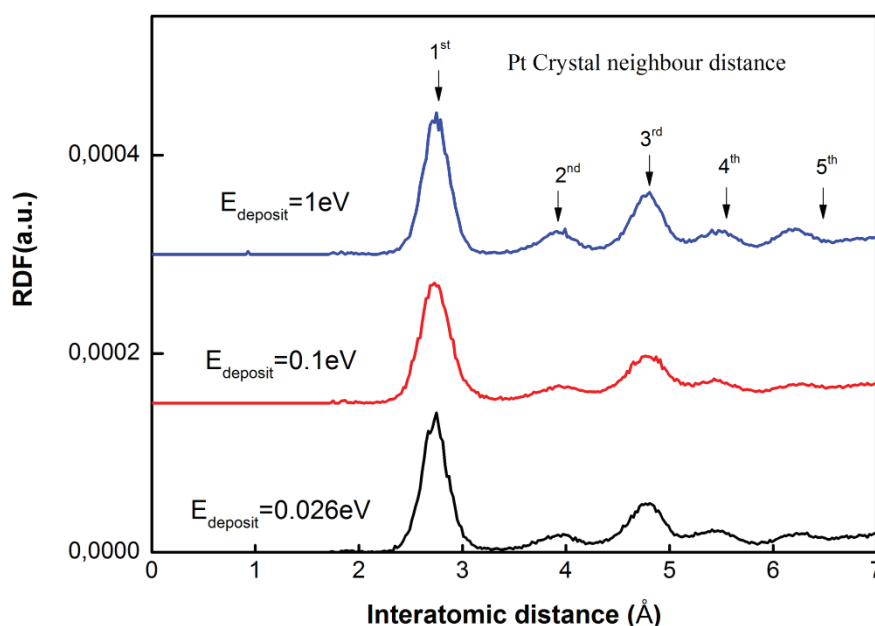


Figure 5.7 – The RDF of the Pt clusters deposit on porous carbon with potential 1

A further insight can be achieved by comparing the Pt crystal XRD patterns with those calculated in these simulations. The calculated X-ray intensities vs. 2θ of Pt cluster for the three energy distributions are shown in figure 5.8 and detailed in table 5.5. Looking at the 1

eV XRD plot, it is observed that peak positions are located at $2\theta = 40.32, 45.43, 68.01$ and 81.21° attributed to the Pt(111), Pt(200), Pt(220) and Pt(311) structures, which is in agreement with the Pt bulk values. It has to be noticed that the Pt(200) peak is progressively disappearing when lowering the incoming energy. So ordering is also better when increasing energy.

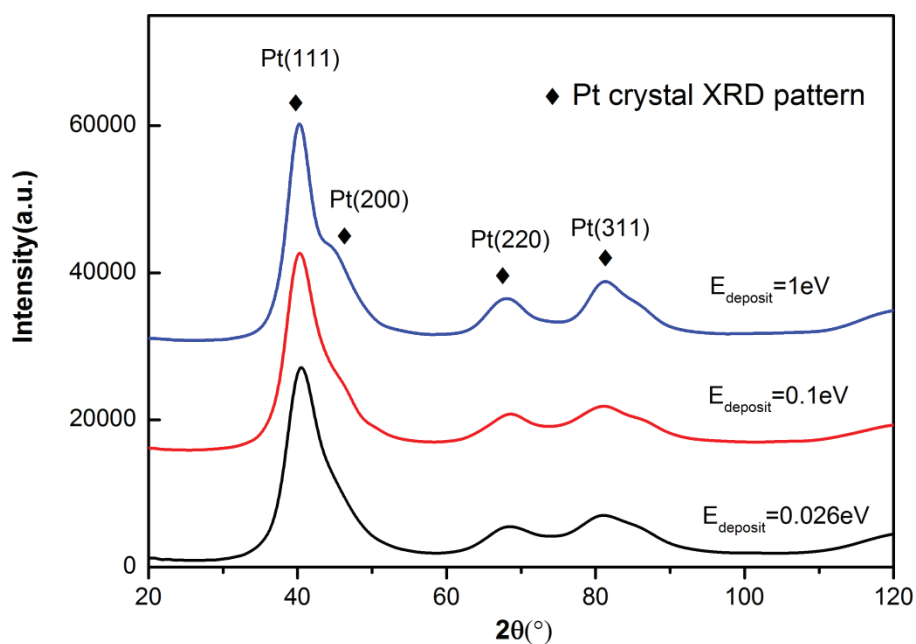


Figure 5.8 – Simulated X-Ray intensity vs. 2θ of Pt-cluster deposit on porous carbon with potential 1

Table 5.5 - the 2θ position of XRD peak for standard Pt crystal and Pt cluster in simulation

Pt cluster in simulation

Unit: 2θ ($^{\circ}$)

Pt	Pt(111)	Pt(200)	Pt(220)	Pt(311)	Pt(222)	Pt(400)	Pt(331)
Pt 1.0 eV	40.32	45.43	68.01	81.21	-	-	-
Pt 0.1 eV	40.41	-	68.64	81.62	-	-	-
Pt 0.026 eV	40.62	-	68.45	81.06	-	-	-

5.3.3 Platinum atom deposit on porous carbon with Pt - C LJ potential 2

In this section, simulations are performed for platinum deposit on porous carbon with potential 2. Snapshots obtained with potential 2 are shown in figure 5.9, with atom deposition energy of Pt-1eV on the top, 0.1eV in the middle and 0.026eV on the bottom.

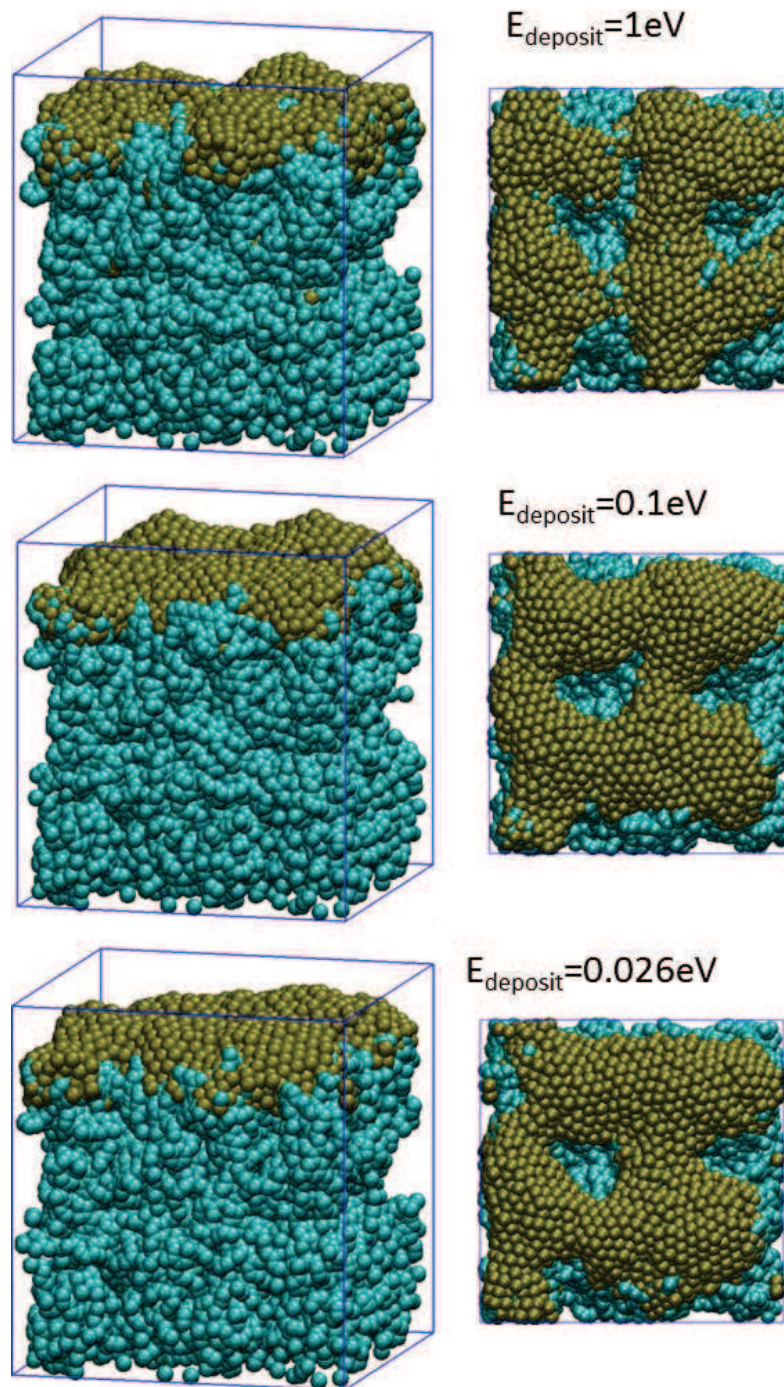


Figure 5.9 - Schematic picture of Pt deposit on porous carbon with potential 2. ●C and ●Pt

The value of ϵ in potential 2 is around 5 times larger than potential 1. With larger ϵ , the bonding between Pt-C used in potential 2 is stronger than for potential 1. So the morphology of Pt changes from cluster to film-like structure. Pt clusters are more flat and smooth. So the higher binding energy allows the growth to fit more closely with the substrate and atomic

scale surface roughness is responsible for perturbing the crystal order [23]. Moreover the Pt atoms are allowed to diffuse through the pores of the substrate (Fig. 5.9). With the previous potential, they do not penetrate into the substrate, due to the lower interaction energy with the substrate compared to the cohesive energy of Pt. The latter leading to more crystallized cluster and so prevents Pt incorporation. This can be related to experimental findings that show the Pt in-diffusion into porous carbon [83-85].

RDF plots are reported in figure 5.10 and are detailed in table 5.6. In all these three cases, the first peak is very broad; second, third and fourth peaks are overlapping for all energies. This is representative of disorder. Nevertheless when looking at the snapshot in Figure 5.9, centered hexagons are clearly visible on the surface. So calculation of the XRD patterns will inform about the the order/disorder status.

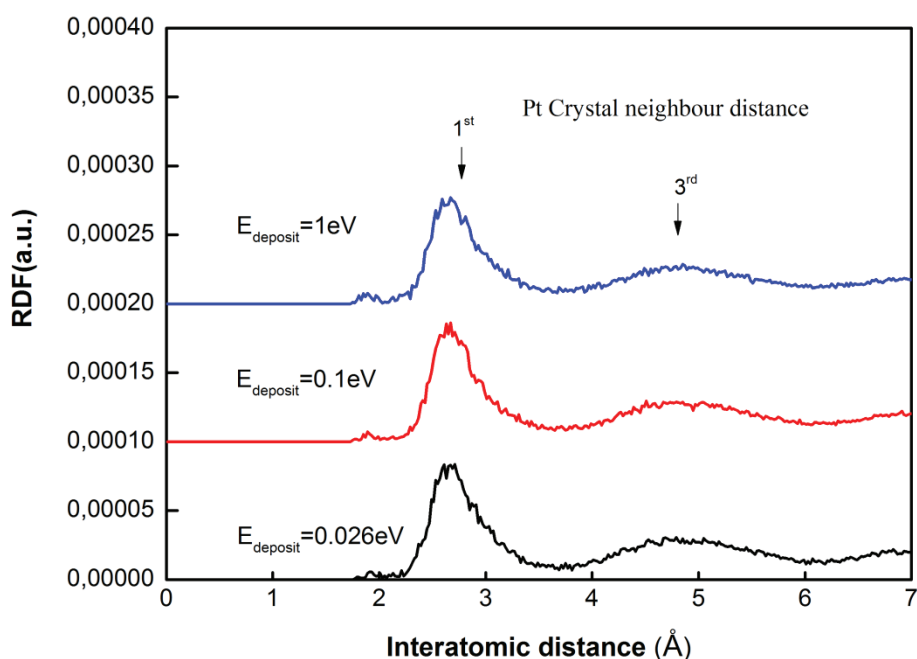


Figure 5.10 – The RDF of the Pt clusters deposit on porous carbon with potential 2

Table 5.6 – RDFs peaks position of Pt deposit on porous carbon with potential 1

	1 st neighbor (Å)	2 nd neighbor (Å)	3 rd neighbor (Å)	4 th neighbor (Å)	5 th neighbor (Å)
Pt crystal value	2.7746	3.9239	4.8058	5.5492	6.79
Pt-1ev	2.66	-	4.79	-	-
Pt-0.1ev	2.65	-	4.67	-	-
Pt-0.026ev	2.67	-	4.85	-	-

As we can see from figure 5.8, the calculated X-ray intensities vs. 2θ of Pt clusters are shown in figure 5.11 and detailed in table 5.7. It can be seen that only two broad peaks arise for each samples attributed to Pt(111) and Pt(220) orientations. This is consistent with observing some surface order in-plane and the fading of 2nd and other neighbor distances.

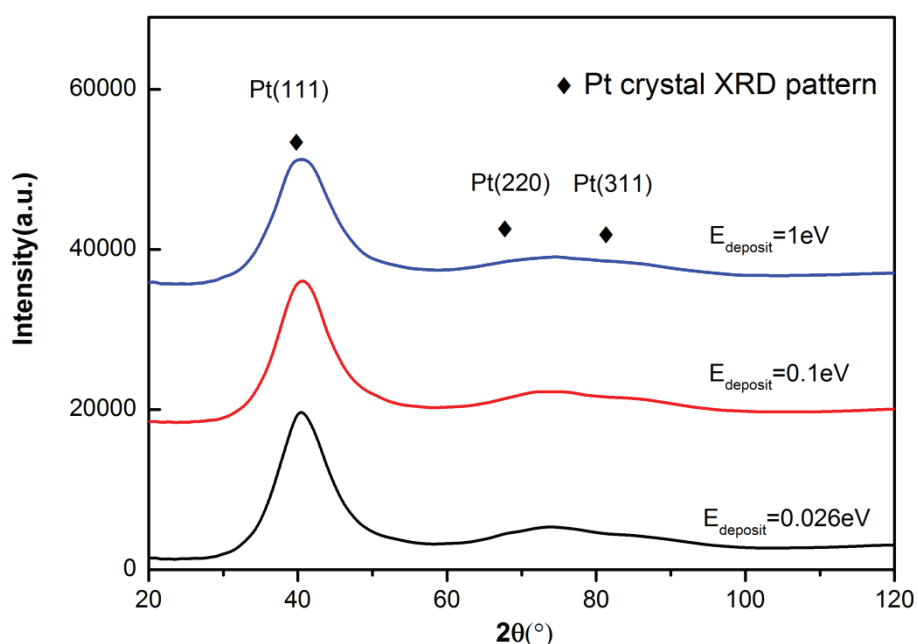


Figure 5.11 – the simulated X-Ray intensity vs. 2θ of Pt-cluster deposit on porous carbon with potential 2

Table 5.7 - the 2θ position of XRD peak for standard Pt crystal and Pt cluster in simulation

Pt cluster in simulation

Unit: 2θ (deg)

Pt	Pt(111)	Pt(200)	Pt(220)	Pt(311)	Pt(222)	Pt(400)	Pt(331)
Pt 1.0 eV	40.56	----	73.95	----	----	----	----

Pt 0.1 eV	40.73	----	72.8	----	----	----	----
Pt 0.026 eV	40.69	----	74.6	----	----	----	----

5.4 Conclusion

Plasma sputter deposition of platinum atoms on two nanostructured carbon substrates was studied by MD simulations at room temperature (300K) and compared against two sets of LJ potential parameters and against three different kinetic energy distributions of incoming Pt atoms. When considering the cluster growth on CNTs, the cluster location along the CNT walls depend on the kinetic energy: when increasing kinetic energy, the clusters are growing deeper towards the CNTs baseline. The morphology is also affected: when increasing energy the clusters are more crystallized as expected. There is no significant difference between the two interaction potentials used regarding the cluster morphology. In both cases crystallized clusters are obtained. This is probably due to the crystallized substrate which drives it.

The situation is quite different on the porous carbon where the less binding potential 1 leads better crystallized clusters. This comes from the Pt cohesive energy which is large enough compared to the surface binding energy for “ignoring” the details of the surface. On the contrary when using the more binding potential 2, the Pt will fit closely the surface morphology and leads to a more two dimensional film. The structure remains crystalline to some extent, due to the low thickness.

Chapter 6: Two dimensional fluid model for magnetron plasma discharge with COMSOL

Pour compléter l'approche microscopique de la dynamique moléculaire réalisée aux chapitres précédents, nous nous sommes intéressés à une approche plus globale du procédé de dépôt par la simulation fluide d'un réacteur simplifié.

Cette étape préliminaire est le premier pas vers une approche multi-échelles. Si la DM doit permettre de mieux comprendre les caractéristiques du dépôt en fonction des propriétés du milieu, par exemple l'énergie des atomes incidents, cette même énergie pourrait être connue en simulant le plasma et le transport des espèces dans le réacteur. Pour cette dernière étape, l'approche généralement utilisée PIC-Monte-Carlo est difficilement applicable si l'on veut modéliser l'ensemble du réacteur. Une solution reste l'approche fluide mais la mise au point de modèles cohérents est une entreprise délicate et peu répandue. Nous avons choisi d'utiliser un modèle tiré des travaux de thèse de C. Costin [4] qui présente un modèle détaillé avec plusieurs résultats à comparer.

Par ailleurs, lorsque de tels modèles existent, ils sont généralement résolus dans des géométries simplifiées à l'aide de codes numériques dédiés. Dans l'optique de pouvoir modéliser des réacteurs réels, nous avons fait le choix d'utiliser un logiciel commercial COMSOL Multiphysics® dont la méthode de résolution est basée sur la méthode des éléments finis.

Ce chapitre décrit le modèle utilisé, son implémentation dans le logiciel de simulation et les résultats préliminaires. L'étude d'influence sur le maillage a permis de définir une grille de calcul avec un bon compromis qualité de maille/temps calcul. Le champ magnétique obtenu est en bon accord avec celui obtenu par Costin. De même, le champ électrique statique calculé en l'absence de charge d'espace est cohérent avec le champ présumé. Bien que le modèle ait été implémenté dans sa totalité dans le logiciel, il reste à poursuivre les calculs avec la résolution des équations permettant d'obtenir les densités électronique et ionique, ainsi que l'énergie électronique. La résolution de ces équations non-linéaires et fortement couplées n'est pas triviale, et nécessite encore des efforts, notamment dans la recherche des bons réglages des solveurs. En effet, si les capacités du logiciel COMSOL doivent permettre de résoudre ce modèle, son caractère boîte noire rend son utilisation moins souple qu'un code maison.

6.1 Introduction

Direct-current (DC) magnetron sputtering has been widely used in the thin film deposition of elemental/compound materials. The structures and properties of the growing film are affected by the process operating conditions, as well as the interactions, through collisions, between energetic particles. The interactions between these particles and the process gas (such as argon) result in momentum and energy exchange between the colliding particles and the gas, and may result in excitation, ionization and dissociation of the process gas as well as other neutrals [86]. The use of a magnetron plays an important role in confining electrons around the vicinity of the target (cathode), and in increasing the collision probability of electrons with the process gas. This in turn increases the creation rate of ions within the plasma.

In this chapter, the two dimensional fluid DC magnetron plasma discharge model referred from Costin [87] was studied using the software COMSOL Multiphysics®. COMSOL is a numerical code based on the finite element method which allows solving partial differential equations (PDEs) in 1D, 2D and 3D domains. There are predefined application modes where the governing PDEs are preset but one can as well freely define the PDEs. Among the predefined application modes there are modules for electromagnetics, mechanics, fluid dynamics, heat transfer and acoustics. All of these application modes can be coupled to multiphysics simulations. Independently of the application mode the geometry, material parameters and boundary conditions of the problem can be set up in a graphical user interface (GUI). Besides, It has possibility of using powerful steady-state solvers, which are essential for systematic study of multiple modes [88]. However, even though COMSOL is a performing tool, it remains a “black box” without too much room for adjustments of routines included.

As the first motivation, this work consists of a large scale numerical approach of the sputtering process / reactor in comparison with the small scale approach: MD simulation. The best will be to link the results concerning the plasma parameters with input data of the MD simulation, and so to have an important numerical tool (MD + multiphysics reactor) of the entire process. The next objective is to simulate with a fluid approach, because we want information on real reactor with acceptable calculation time. Finally, because it is our first work on this subject, we begin with a model previously solved to which we can compare. We have chosen the model of Costin [87, 89, 90], because we have not lot of choice and also because we have “a lot ” of results and a detailed description of the model in the PhD manuscript [89].

In this work, 2D magnetron plasma discharge model is based on a fully-coupled treatment of plasma fluid model together with the electric and magnetic field evolution equations. For numerical simulations the fluid model has an advantage in terms of the computing time but it loses validity when decreasing the gas pressure so when the mean free path of charged particles strongly exceeds the characteristic length of the discharge. Although magnetron discharges work at low pressures (1 to tens of mTorr), the presence of the magnetic field reduces the effective distance covered by electrons between two collisions (the motion between two collisions is a spiral and thus the traveled distance can be long even if the distance between collision is small), which is equivalent to an increase of the pressure, thus fulfilling the hydrodynamic hypothesis [86].

The assumptions used for the model are:

- 1) An original two-dimensional (r, z), time-dependent fluid model approach is used to describe the transport of two charged species, electrons and Ar ions, in a cylindrically symmetric dc planar magnetron reactor. The transport of the charged species is described by the corresponding first three moments of the Boltzmann equation: continuity, momentum transfer and mean energy transfer equation. All transport equations are treated in the same manner, using a classical drift–diffusion expression for fluxes.
- 2) For ease of calculation, we assume that the electric field and the static magnetic field are independent with each other. The magnetic field is created by the permanent magnets without any effect of the electrostatic field and the movement of the charged particles. Actually, the magnetic field generated by azimuthal drift current in the plasma ring in front of the target are only be the order of a few amperes [91], which is about a few per cent of the static field. This is not considered in this system.

6.2 Formulation review

6.2.1 The electron equations

The basic fluid equations for electron are written below (equation 6.1-6.3). They are described by the corresponding first three moments of the Boltzmann equation: continuity, momentum transfer and mean energy transfer equation.

$$\frac{\partial n_e}{\partial t} + \nabla \cdot \vec{\Gamma}_e = S_e \quad (\text{E-6.1})$$

$$m_e n_e \left[\frac{\partial \vec{v}_e}{\partial t} + (\vec{v}_e \cdot \nabla) \vec{v}_e \right] = e n_e (\vec{E} + \vec{v}_e \times \vec{B}) - \nabla \cdot \vec{\bar{P}}_e - m_e n_e f_{me} \vec{v}_e \left(1 + \frac{f_{iz}}{f_{me}} \right) \quad (\text{E-6.2})$$

$$\frac{\partial (n_e \varepsilon_e)}{\partial t} + \nabla \cdot \vec{\Gamma}_{\varepsilon e} = -\vec{\Gamma}_e \cdot \vec{E} - \theta_e n_e \quad (\text{E-6.3})$$

where n_e is the electron density, m_e the electron mass, \vec{v}_e the velocity, f_{iz} the ionization frequency by electron-neutral collisions, \vec{E} the electric field intensity, $\vec{\bar{P}}$ the pressure tensor, e the particle charge, t the time, ε_e the electron mean energy (in eV), θ_e the energy loss rate for electron-neutral collisions, $\vec{\Gamma}_e = n_e \vec{v}_e$ is the flux of electron and $\vec{\Gamma}_{\varepsilon e} = n_e \langle \varepsilon_e \vec{v}_e \rangle$ the energy flux for electrons, The source term in the continuity equation $S = f_{iz} n_e$, considering that electrons are created only by electron-neutral ionization collisions. The magnetic field, \vec{B} , considered in the calculations takes into account only the stationary magnetic field produced by the magnets below discharged region, excluding the one generated by movement of the charged species.

The flux can be expressed in the form:

$$\vec{\Gamma}_e = \vec{\Gamma}_e^0 + \vec{\Gamma}_e^1 \quad (\text{E-6.4})$$

where $\vec{\Gamma}_e^0$ the classical drift and $\vec{\Gamma}_e^1$ a contribution of the magnetic field

Some simplifying assumptions were made in E-6.2 in order to obtain the electron flux in E-6.4:

- 1) The inertial term $m_e n_e [\partial \vec{v}_e / \partial t + (\vec{v}_e \cdot \nabla) \vec{v}_e]$ were neglected due to small mass of the electron,
- 2) The ionisation frequency f_{iz} was also neglected with respect to the total electron-neutral momentum transfer frequency, f_{me}
- 3) Considering isotropic electron distribution function, the pressure tensor becomes a scalar, where $P_e = n_e k T_e$,

Thus, the momentum transfer equation can be written as:

$$n_e \vec{v}_e = -\frac{e}{m_e f_{me}} n_e \vec{E} - \nabla \left(\frac{k T_e}{m_e f_{me}} n_e \right) - \frac{e}{m_e f_{me}} n_e \vec{v}_e \times \vec{B} \quad (\text{E-6.5})$$

where $\mu_e = \frac{e}{m_e f_{me}}$ and $D_e = \frac{k T_e}{m_e f_{me}}$ are electron mobility and diffusion coefficient, respectively. The two electron flux components are then,

$$\vec{\Gamma}^0 = -\mu_e n_e \vec{E} - \nabla (D_e n_e) \quad (\text{E-6.6})$$

$$\vec{\Gamma}^1 = -n_e \vec{v}_e \times \frac{\vec{\Omega}_e}{f_{me}} \equiv -\vec{\Gamma}_e \times \frac{\vec{\Omega}_e}{f_{me}} \quad (\text{E-6.7})$$

$\vec{\Omega}_e = \frac{e \vec{B}}{m_e}$ is related to electron cyclotron giro-frequency. Due to the cylindrical symmetry, $\vec{\Gamma}_e^0$

has only two components, $\vec{\Gamma}_{er}^0$ and $\vec{\Gamma}_{ez}^0$, while $\vec{\Gamma}_e^1$ can be obtained by the magnetic field with the matrix below:

$$\begin{pmatrix} \vec{\Gamma}_{er}^1 \\ \vec{\Gamma}_{ez}^1 \end{pmatrix} = \frac{1}{f_{me}^2 + \Omega_e^2} \begin{pmatrix} -\Omega_e^2 & \Omega_{er} \Omega_{ez} \\ \Omega_{er} \Omega_{ez} & -\Omega_{er}^2 \end{pmatrix} \begin{pmatrix} \vec{\Gamma}_{er}^0 \\ \vec{\Gamma}_{ez}^0 \end{pmatrix} \quad (\text{E-6.8})$$

The energy flux can be written in the same way as electron flow, using the energy mobility μ_{ε} , and the energy diffusion coefficient D_{ε} :

$$\vec{\Gamma}_{\varepsilon\varepsilon} = \vec{\Gamma}_{\varepsilon\varepsilon}^0 + \vec{\Gamma}_{\varepsilon\varepsilon}^1 \quad (\text{E-6.9})$$

and the first and second term can be expressed:

$$\vec{\Gamma}_{\varepsilon\varepsilon}^0 = -\mu_e n_e \varepsilon_e \vec{E} - \nabla(D_e n_e \varepsilon_e) \quad (\text{E-6.10})$$

$$\vec{\Gamma}_{\varepsilon\varepsilon}^1 = -n_e \langle \varepsilon_e \vec{v}_e \rangle \times \frac{\vec{\Omega}_e}{f_{me}} \equiv -\vec{\Gamma}_{\varepsilon\varepsilon} \times \frac{\vec{\Omega}_e}{f_{me}} \quad (\text{E-6.11})$$

$$\begin{pmatrix} \vec{\Gamma}_{\varepsilon\varepsilon r}^1 \\ \vec{\Gamma}_{\varepsilon\varepsilon z}^1 \end{pmatrix} = \frac{1}{f_{me}^2 + \Omega_e^2} \begin{pmatrix} -\Omega_{ez}^2 & \Omega_{er}\Omega_{ez} \\ \Omega_{er}\Omega_{ez} & -\Omega_{er}^2 \end{pmatrix} \begin{pmatrix} \vec{\Gamma}_{\varepsilon\varepsilon r}^0 \\ \vec{\Gamma}_{\varepsilon\varepsilon z}^0 \end{pmatrix} \quad (\text{E-6.12})$$

The reduced electron transport parameters, $D_e N$ and $\mu_e N$, depend on electron energy

distribution function (EEDF), $f(\vec{r}, u)$, where $u = \frac{m_e v^2}{2e}$ is the electron kinetic energy in eV.

Under the classical two terms approximation of EEDF they can be written [92] as

$$D_e(\vec{r})N = \frac{1}{3} \sqrt{\frac{2e}{m_e}} \int_0^\infty \frac{u}{\sigma_{me}(u)} f_0(\vec{r}, u) du \quad (\text{E-6.13})$$

$$\mu_e(\vec{r})N = \frac{1}{3} \sqrt{\frac{2e}{m_e}} \int_0^\infty \frac{u}{\sigma_{me}(u)} \frac{\partial f_0(\vec{r}, u)}{\partial u} du \quad (\text{E-6.14})$$

where σ_{me} is the total electron-neutral momentum transfer collision cross section, N is the gas density $N = p/kT$ and $f_0(\vec{r}, u)$ is the isotropic part of $f(\vec{r}, u)$, satisfying the normalization condition:

$$\int_0^\infty f_0(\vec{r}, u) u^{1/2} du = 1 \quad (\text{E-6.15})$$

The energy flux is written in the same manner as the particle flux, with corresponding reduced transport coefficients, $D_{\varepsilon\varepsilon} N$ and $\mu_{\varepsilon\varepsilon} N$:

$$D_{\varepsilon\varepsilon}(\vec{r})N = \frac{1}{\varepsilon_e(\vec{r})} \frac{1}{3} \sqrt{\frac{2e}{m_e}} \int_0^\infty \frac{u}{\sigma_{me}(u)} f_0(\vec{r}, u) du \quad (\text{E-6.16})$$

$$\mu_{ee}(\vec{r})N = \frac{1}{\varepsilon_e(\vec{r})} \frac{1}{3} \sqrt{\frac{2e}{m_e}} \int_0^\infty \frac{u}{\sigma_{me}(u)} \frac{\partial f_0(\vec{r}, u)}{\partial u} du \quad (\text{E-6.17})$$

The spatial map of electron transport parameters can be obtained adopting the local mean energy approximation [92], which consists in introducing the spatial dependence of EEDF via the electron mean energy profile, $\varepsilon_e(\vec{r})$. The profile $\varepsilon_e(\vec{r})$ of the electron mean energy is obtained as solution of electron mean energy transfer equation (E-6.3). Due to the high density of the magnetron plasma, a maxwellian EEDF was considered instead of calculating the solution of electron Boltzman equation,

$$f_0(\vec{r}, u) = f_0[\varepsilon_e(\vec{r}), u] \equiv \frac{2}{\sqrt{\pi}} \left[\frac{2\varepsilon_e(\vec{r})}{3} \right]^{-3/2} e^{-3u/2\varepsilon_e(\vec{r})} \quad (\text{E-6.18})$$

In the equation 6.3, electron energy loss rate in elastic and inelastic (excitation, ionisation) collisions is calculated according to the same reference [92]

$$\theta_e(\vec{r}) = N \frac{2m_e}{M_n} \sqrt{\frac{2e}{m_e}} \int_0^\infty \sigma_{en}^{el}(u) f_0(\vec{r}, u) u^2 du + \sum_k^{\text{intel}} W_k f_{ke}(\vec{r}) \quad (\text{E-6.19})$$

where M_n is the mass neutral atoms, σ_{en}^{el} is elastic cross section of the electron-neutral collision, W_k the energetic threshold for the k-inelastic process characterized by f_{ke} collision frequency. All collision frequencies are calculated with:

$$f_{me}(\vec{r}) = N \sqrt{\frac{2e}{m_e}} \int_0^\infty \sigma_{me}(u) f_0(\vec{r}, u) u du \quad (\text{E-6.20})$$

using collision cross sections given by [93]. Elastic, excitation and ionization collisions with ground state neutrals are considered.

6.2.2 The ions transport equations

The ion transport equations are derived from the moment of the ion Boltzman equation, by assuming small drift velocities when compared to thermal velocities [94]. The electron essentially controls the non-local energy transport, usually considers the first two moments of

the ions Boltzmann equation, corresponding to the ion continuity and momentum transfer equations.

$$\frac{\partial n_i}{\partial t} + \nabla \cdot \vec{\Gamma}_i = S_i \quad (\text{E-6.21})$$

$$m_i n_i \left[\frac{\partial \vec{v}_i}{\partial t} + (\vec{v}_i \cdot \nabla) \vec{v}_i \right] = q_i n_i (\vec{E} + \vec{v}_i \times \vec{B}) - \nabla \vec{P}_i - m_i n_i f_{mi} \vec{v}_i \left(1 + \frac{f_{iz}}{f_{mi}} \right) \quad (\text{E-6.22})$$

In the ion momentum transfer equation, we also make some simplifying assumptions due to the properties of ion:

- 1) The inertial term cannot be neglected due to the ion heavier mass.
- 2) Magnetic field influence was not considered because ion cyclotron giro-radius is larger than the linear dimension of the examined region.
- 3) The ion pressure tensor was also considered as scalar, $P_i = n_i k T_i$, by the reason of isotropic ion distribution function assumed.

Under such assumptions, ion momentum transfer equation becomes:

$$n_i \vec{v}_i = -\frac{e}{m_i f_{mi}} n_i \vec{E} - \nabla \left(\frac{k T_i}{m_i f_{mi}} n_i \right) - \frac{n_e f_{iz}}{n_i f_{mi}} n_i \vec{v}_i - \frac{1}{f_{mi}} n_i \left[\frac{\partial \vec{v}_i}{\partial t} + (\vec{v}_i \cdot \nabla) \vec{v}_i \right] \quad (\text{E-6.23})$$

For convenience the ion flux is written in a drift-diffusion form, by introducing an effective electric field, \vec{E}^{eff} , [95] so that

$$\vec{\Gamma}_i = n_i \vec{v}_i = \mu_i n_i \vec{E}^{eff} - \nabla (D_i n_i) \quad (\text{E-6.24})$$

Identifying these two expressions, E-6.23 and E-6.24, for the ion flux and performing some simple calculations [96], an equation for the space-time evolution of \vec{E}^{eff} is yielded

$$\frac{\partial \vec{E}^{eff}}{\partial t} = f_{mi} (\vec{E} - \vec{E}^{eff}) - f_{iz} \frac{n_e}{n_i} \frac{\vec{v}_i}{\mu_i} - \frac{1}{\mu_i} (\vec{v}_i \cdot \nabla) \vec{v}_i \quad (\text{E-6.25})$$

Argon ions reduced diffusion coefficient is deduced from Einstein relation

$$D_i N = \mu_i N \frac{k T_i}{e} \quad (\text{E-6.26})$$

where ion reduced mobility depends on the reduced effective electric field

$$\mu_i N = f\left(\frac{\vec{E}^{eff}}{N}\right) \quad (\text{E-6.27})$$

Argon ions were supposed to be thermalized at gas temperature, $T_i = T_{Ar}$. The ion momentum transfer frequency, f_{mi} , was calculated through the expression for classical mobility

$$f_{mi} = N \frac{e}{m_i (\mu_i N)} \quad (\text{E-6.28})$$

6.2.3 The electric and static magnetic fields equations

The electric field and plasma potential are given by the Poisson equation:

$$\Delta V = -\frac{e}{\epsilon_0} (n_i - n_e) \quad (\text{E-6.29})$$

$$\vec{E} = -\nabla V \quad (\text{E-6.30})$$

In magnetostatic field where no electric currents are present, it is possible to formulate and solve the problem using a scalar magnetic potential. In a current-free region where $\nabla \times H = 0$, this implies that the magnetic scalar potential V_m can be defined from the relation $H = -\nabla V_m$, which is analogous to the definition of the electric potential for static electric fields.

Using the constitutive relation

$$B = \mu_0 (H + M), \text{ M is the magnetization} \quad (\text{E-6.31})$$

The equation $\nabla \cdot B = 0$ becomes

$$-\nabla \cdot (\mu_0 \nabla V_m - \mu_0 M) = 0 \quad (\text{E-6.32})$$

and we use this equation for modeling of magnetostatics in the absence of electric currents.

6.2.4 Input data

The transport coefficient and the properties of the theoretical model, such as reduced mobility and diffusion or electron energy loss rate, are presented in this section. They are used as the input data in COMSOL.

In the argon plasma, by introducing the total electron-neutral momentum transfer collision cross section $\sigma_{me}(u)$ according to [93], the coefficient of mobility and diffusion are calculated according to E-6.3, 6.4, 6.6 and 6.7 and plotted as a variable of mean energy of electron (ε_e) shown in figure 6.1 and 6.2. The profile of the electron mean energy ε_e is obtained as a solution of the electron mean energy transfer equation (E-6.3).

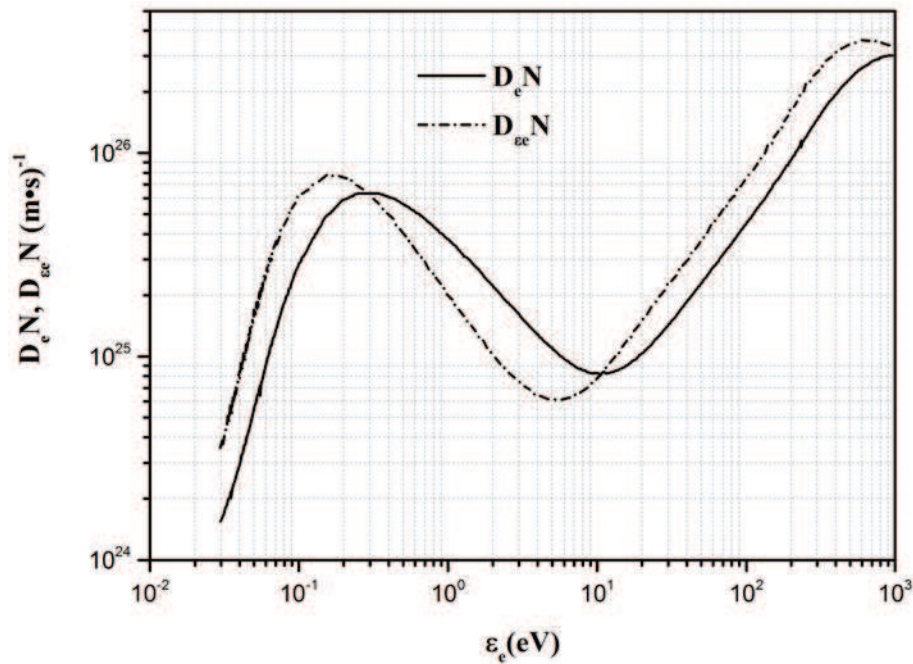


Figure 6.1 - the reduced diffusion coefficient of electron based on mean energy of electron.

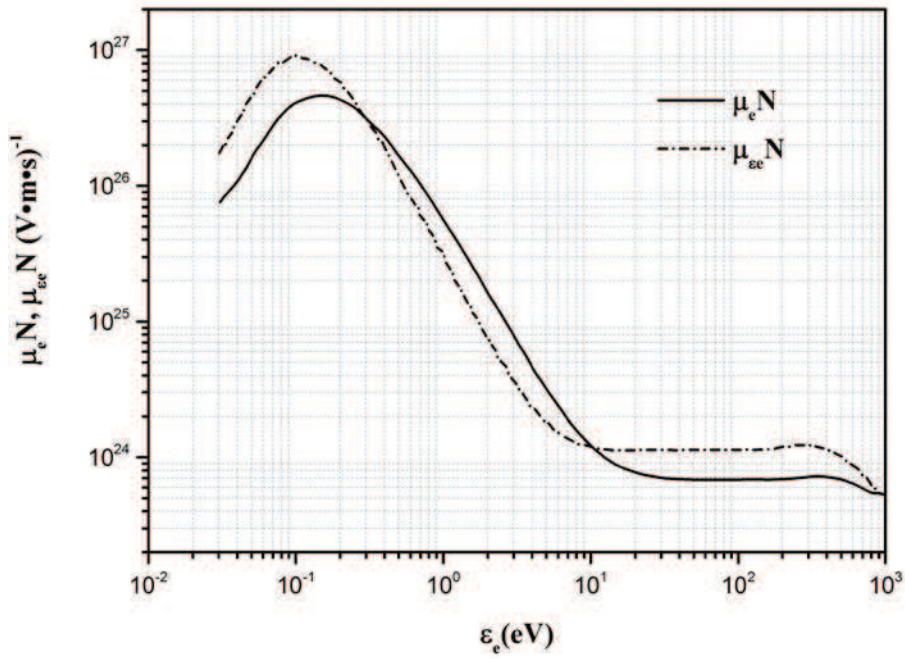


Figure 6.2-the reduced mobility of electron based on mean energy of electron.

Similarly, the rate of energy losses for electrons is calculated by E-6.19 and plotted in figure 6.3.

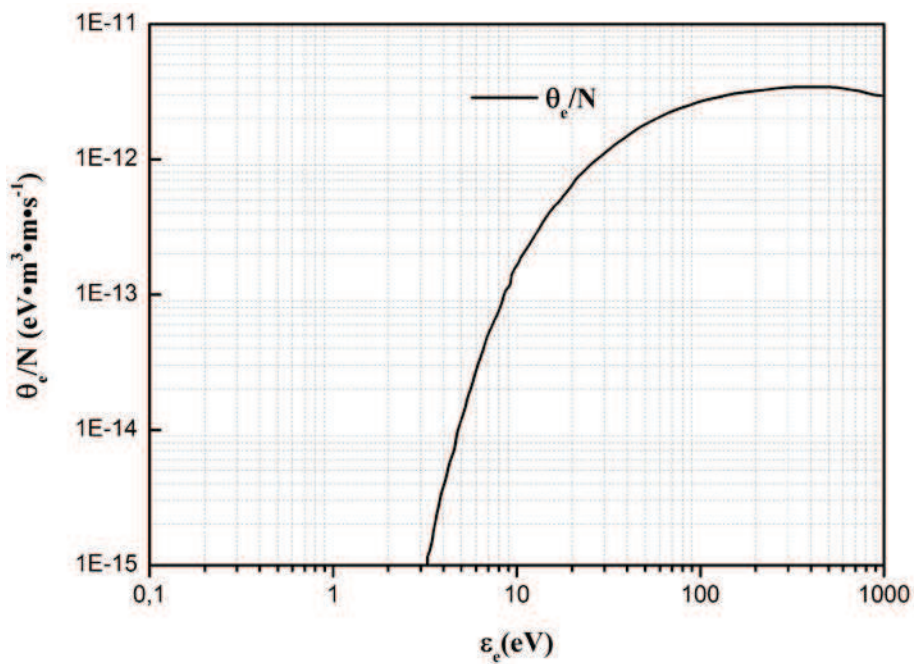


Figure 6.3 the relationship between the mean electron energy loss rate and the mean electron energy.

Figure 6.4 displayed the relationship f_{iz} / f_{me} with mean electron energy according to the reference [89], where f_{iz} is the ionization frequency by electron-neutral impact and f_{me} is the total momentum transfer frequency for electron-neutral. f_{me} can be calculated from

$$f_{me} = \frac{e}{m_e \mu_e} \text{ and } f_{iz} \text{ can be got from this interpolation function.}$$

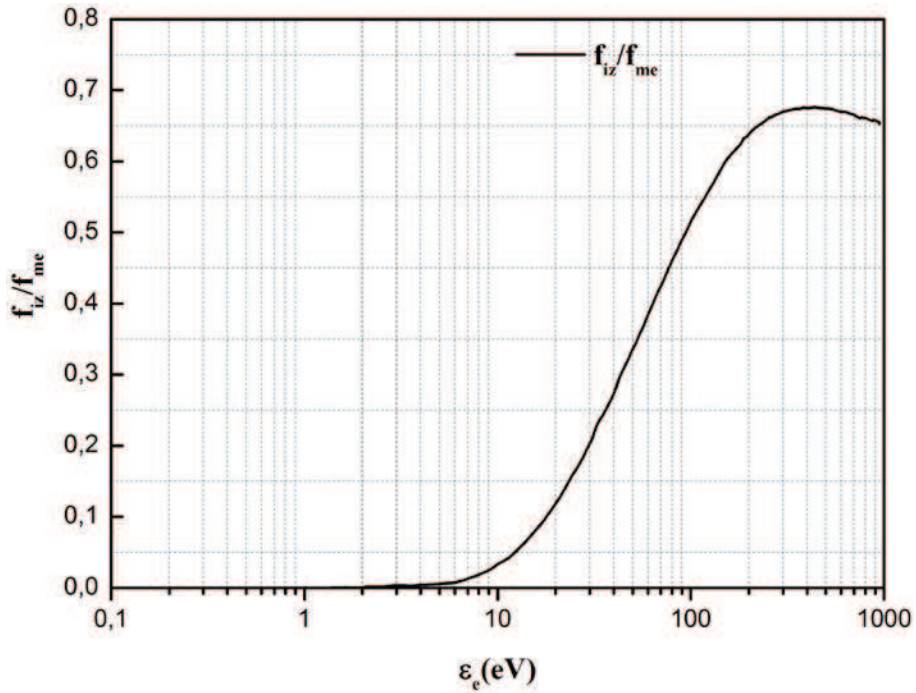


Figure 6.4-the value of f_{iz} / f_{me} based on the the electron energy

The ion transport coefficients used in COMSOL model can be obtained from H. W. Ellis et al [97] and A. V. Phelps [98]. Figure 6.5 shows values of the reduced mobility of argon ions depending on E/N, where E is the effective electric field. Correspondingly, the coefficient of argon ions can be deduced from the Einstein relation (E-6.26).

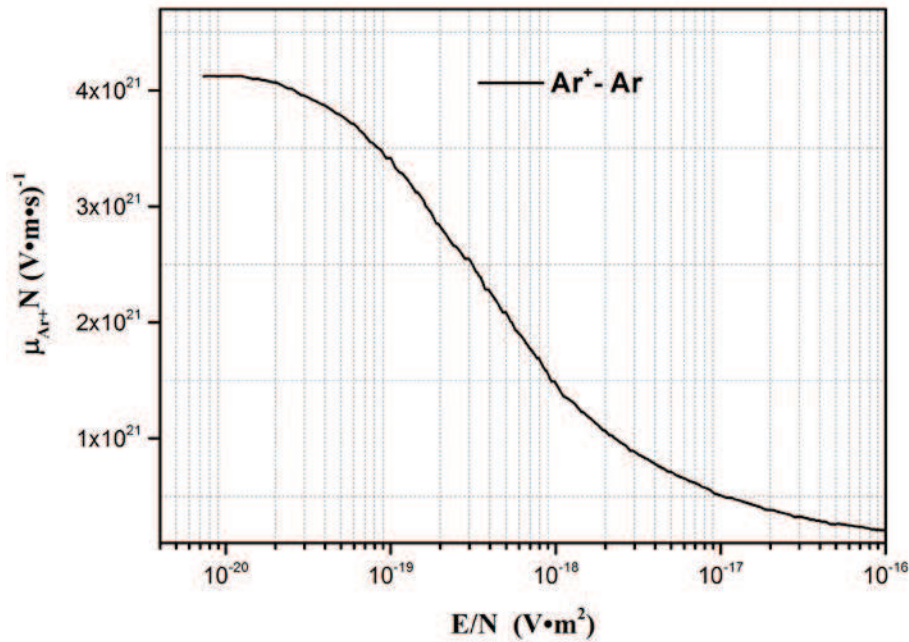


Figure 6.5-the relationship between reduced mobility of argon ion with the E/N

6.3 Numerical procedure with COMSOL

6.3.1 Geometry

Figure 6.6 shows schematically 2D reactor geometry with cathode, anode and magnets. Due to the cylindrical symmetry of the system only a bi-dimensional picture is plotted. The cathode is a metallic disc with radius of 16.5 mm, and grounded metallic walls play the role of the anode ($R_{\max} = Z_{\max} = 26.95$ mm). A gap between anode and cathode serves as insulator with a distance of 0.25mm. The magnetic field is created by a pair of arranged coaxial permanent magnets below the plasma chamber. The magnet core is a cylinder with the diameter of 12.5 mm and height of 12 mm, another magnet shape of a ring with 24 mm of inner diameter, 30 mm outer diameter and height of 13 mm (figure 6.7). The polarity of two magnets alternates. Thus, the magnetic field lines start from one magnet and close on another in a semi-toroidal geometry. This magnetic configuration is the most common used in planar cathodes.

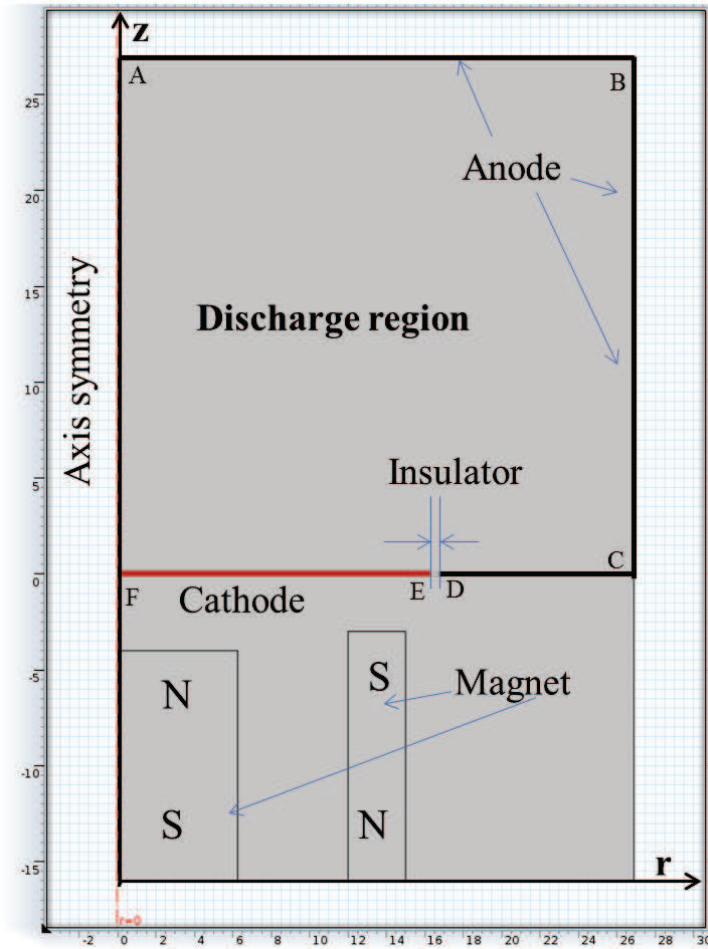


Figure 6.6 – Reactor geometry.

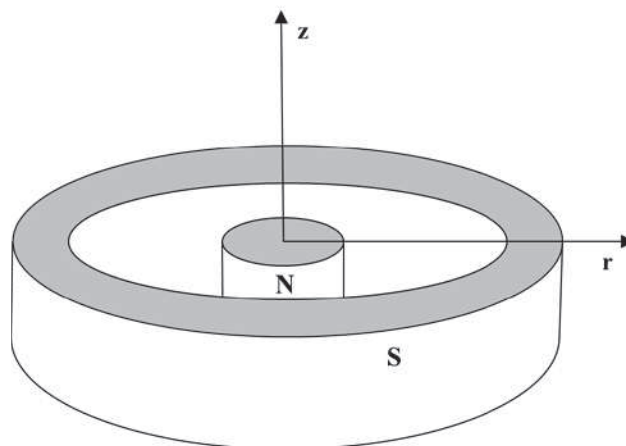


Figure 6.7 - Magnet configuration used in the model.

What needs illustration is that the magnetic field simulated in this model involves the whole domain displayed in figure 6.1, while for plasma and electric field just in the discharge region.

6.3.2 Materials and initial value

Argon was chosen as the working gas and the Soft iron (without losses) are used for the magnets. Initial values for the dependent variables can serve as an initial condition for a transient simulation or as an initial guess for a nonlinear solver. Before calculation, the initial values of the system are specified and summarized in table 6.1.

Table 6.1-The initial value of the system.

Parameters	Value	Unit	Description
V_0	-550	V	Applied voltage
P_0	0,02	torr	Gas pressure
T_0	350	K	Gas temperature
M_0	650	kA/mkA·m ⁻¹	The magnetization of soft irons
n_e	10 ¹⁵	m ⁻³	The initial electron density
n_i	10 ¹⁵	m ⁻³	The initial ions density
n_{ee}	6.25 ³⁵	kg·m ⁻¹ ·s ⁻³ ·A ⁻¹	The initial electron energy density

6.3.3 Model implementation

In the model of COMSOL, we use the electrostatic field (module Electrostatics) and the static magnetic field (module Magnetic Field, No Currents) in the whole domain (figure 6.6) exploring the external electromagnetic for the plasma system and then, we use “General form PDE” and “Coefficient Form PDE” for characterizing the equations of electron continuity, electron energy and ions continuity in discharge region.

$$e_a \frac{\partial^2 u}{\partial t^2} + d_a \frac{\partial u}{\partial t} + \nabla \cdot \Gamma = f \quad (\text{E-6.33})$$

Equation 6.33 is the default equation for a General Form PDE interface in COMSOL. By specifying the coefficients for a general form PDE, with the equation coefficients, e_a , d_a , Γ and

f, we can get the equation of electron continuity, electron energy and ions continuity. Taking electron as an example, by setting variable as n_e and the coefficients of $e_a=1$ and $d_a=0$, the general form PDE become the equation of electron continuity in E-6.1. The momentum transfer equation of electron can be expressed as electron flux $\vec{\Gamma}_e$ in the form in E-6.4 considering $\vec{\Gamma}_e^0$ as the classical drift-diffusion flux and $\vec{\Gamma}_e^1$ a contribution of the magnetic field. This term can be expressed as intermediate variable involving input data of mobility and coefficient of electron, the variable (n_e, n_i, n_{ee}, B_r or B_z). The equations of electron mean energy transfer and the ions continuity are treated in the same way.

However, the equation of the space-time evolution of \vec{E}^{eff} , where \vec{E}^{eff} was used in ion flux instead of \vec{E} , does not have the general form as described in E-6.33. So we choose “Coefficient Form PDE” as interface for this equation. In coefficient form, the PDE problem reads

$$e_a \frac{\partial^2 u}{\partial t^2} + d_a \frac{\partial u}{\partial t} + \nabla \cdot (-c \nabla u - \alpha u + \gamma) + \beta \cdot \nabla u + \alpha u = f \quad (\text{E-6.34})$$

6.3.4 Boundary conditions

Fluid equations as well as Poisson equation can be solved only if boundary conditions are specified. All the boundary conditions of equation used in this model are summarized in table 6.2.

Table 6.2-the boundary condition of the system

	AB(anode)	BC(anode)	CD(anode)	DE(interval)	EF(cathode)	FA (axis symmetry)
Electric field		$V = 0$		$\vec{n} \cdot E = 0$	$V = -350V$	$\frac{\partial V}{\partial r} = 0$
Electrons		$\Gamma_e^\perp = n_e \langle v_e \rangle / 2$ $\langle v_e \rangle = \sqrt{\frac{2e}{m_e}} \int_0^\infty f_0(\vec{r}, u) u du$ $f_0(\vec{r}, u) = f_0[\varepsilon_e(\vec{r}), u] = \frac{2}{\sqrt{\pi}} \left[\frac{2\varepsilon_e(\vec{r})}{3} \right]^{\frac{3}{2}} e^{-\frac{3u}{2\varepsilon_e(\vec{r})}}$		$-\vec{n} \cdot \Gamma_e = 0$	$\Gamma_e^\perp = -\gamma_i \Gamma_i^\perp \left(1 - \frac{\Omega_{er}^2}{f_{me}^2 + \Omega_{er}^2} \right)$ $\gamma_i = 0.02$	$\frac{\partial n_e}{\partial r} = 0$
Electron energy		$\Gamma_{e\varepsilon}^\perp = \frac{n_e \langle \varepsilon_e v_e \rangle}{2} = \frac{-\Gamma_{e\varepsilon}}{2}$ $\Gamma_{e\varepsilon} = \sqrt{(\Gamma_{e\varepsilon r})^2 + (\Gamma_{e\varepsilon z})^2}$		$-\vec{n} \cdot \Gamma_{e\varepsilon} = 0$	$\Gamma_{e\varepsilon}^\perp = \Gamma_e^\perp \varepsilon_0 = -\gamma_i \Gamma_i^\perp \left(1 - \frac{\Omega_{er}^2}{f_{me}^2 + \Omega_{er}^2} \right) \varepsilon_0$ $\varepsilon_0 = 1eV$ $\gamma_i = 0.02$	$\frac{\partial n_{e\varepsilon}}{\partial r} = 0$
Ions		$\Gamma_i^\perp = \frac{n_i v_{thi}}{4} + \delta \mu_i n_i E_{iz}^{eff \perp}$ $v_{thi} = \left(\frac{8kT_i}{\pi m_i} \right)^{1/2}$ <i>If $E_{iz}^{eff \perp} \cdot \vec{n} > 0$ then $\delta = 1$ else $= 0$</i>		$-\vec{n} \cdot \Gamma_i = 0$	$\Gamma_i^\perp = \frac{n_i v_{thi}}{4} + \delta \mu_i n_i E_{iz}^{eff \perp}$ $v_{thi} = \left(\frac{8kT_i}{\pi m_i} \right)^{1/2}$ <i>If $E_{iz}^{eff \perp} \cdot \vec{n} > 0$ then $\delta = 1$ else $= 0$</i>	$\frac{\partial n_i}{\partial r} = 0$

The details of the boundary conditions are shown below:

The boundary condition of electron:

Anode: $\Gamma_e^{\parallel} = 0$ and $\Gamma_e^{0\perp} = n_e \langle v_e \rangle / 2$ [92],

$$\text{where } \langle v_e \rangle = \sqrt{\frac{2e}{m_e}} \int_0^{\infty} f_0(\vec{r}, u) u du \quad (\text{E-6.35})$$

is the mean electron velocity obtained by integrating over EEDF.

Cathode: In the same conditions, the parallel flux is the same as anode with $\Gamma_e^{\parallel} = 0$, while normal flux has two components: one is coming from the discharge, $n_e \langle v_e \rangle / 2$, while the other one is due to the secondary electrons emitted by ion impact [90].

$$\Gamma_e^{\perp} = -\gamma_i \Gamma_i^{\perp} \left(1 - \frac{\Omega_{er}^2}{f_{me}^2 + \Omega_e^2} \right) = -\gamma_{net} \Gamma_i^{\perp} \quad (\text{E-6.36})$$

$$\text{With } \gamma_{net} = -\gamma_i \left(1 - \frac{\Omega_{er}^2}{f_{me}^2 + \Omega_e^2} \right) \text{ and } \gamma_i = 0.01 \quad (\text{E-6.37})$$

The boundary condition of electron energy:

The boundary conditions for the equivalent flux are available for electron energy transport by changing $\langle v_e \rangle$ to $\langle \varepsilon_e v_e \rangle$ and taking a mean energy, $\langle \varepsilon_0 = 1 eV \rangle$, for secondary electrons emitted at the cathode surface, even if in the literature are given energy values between 2 - 6 eV [99].

The boundary condition of ion:

For all surfaces, normal ion flux is given by,

$$\Gamma_i^{\perp} = n_i v_{thi} / 4 + \delta \mu_i n_i E_{eff}^{\perp} \quad (\text{E-6.38})$$

where $v_{thi} = \left(\frac{8kT_i}{\pi m_i} \right)^{1/2}$ is ion thermal velocity;

if E_{eff}^{\perp} is directed to the surface, $\delta=1$ and $\delta=0$ otherwise.

For Poisson equation, the boundary conditions include the fact that the anode is grounded ($V_{\text{anode}} = 0$) and that a negative voltage, V_{cathode} , is applied to the cathode.

6.3.5 Mesh

All of the meshes were created using COMSOL's physics based meshing option. The mesh of the geometry is divided in two parts, the insulator between anode and cathode and other remaining part. We use edge style to mesh the insulator and free triangular for the other. the max and min element size of four mesh (Extra fine, Fine, Normal and Coarse) are presented in table 6.3.

Table 6.3-the max and min element size of four kind mesh style.

Mesh style	Insulator (Edge)		Other domain (Free Triangular)	
	Max element size	Min element size	Max element size	Min element size
Extra fine	0,005	0,005	0,322	0,0858
Fine	0,1	0,1	0,644	0,15
Normal	0,2	0,2	0,858	0,429
Coarse	0,5	0,5	1,29	0,644

6.4 Preliminary result

The accuracy of the solution by COMSOL Multiphysics is highly dependent of the distribution and size of the elements. A mesh density analysis was carried out to learn about the effect of mesh density on the numerical solution convergence of magnetic field and its behavior. Four meshes were created, these meshes are designated to be Extral fine, Fine, Normal and Coarse. The mesh statistics is presented in table 6.4.

Table 6.4-the mesh statistics.

Mesh type	Extra fine	Fine	Normal	Coarse
Number of boundary elements	785	345	256	176
Number of elements	38256	7546	4229	2001
Minimum element quality	0,7032	0,7577	0,7611	0,8537
Mesh quality (> 0,95)	99% (volume)	95% (volume)	90% (volume)	80% (volume)
Calculation time (seconds)	42	6	3	1

Figure 6.8 displayed the electric field (E_r , E_z and $\|E\|$) at $z=0$, (A)-(D) are the different mesh style with extra fine, fine, normal and coarse separately. It can be seen that the electric field in insulator is much affected by the mesh. With the mesh of extra fine and fine, $\|E\|$ have two peaks at the edge of insulator with combination of E_r and E_z , while for normal and coarse, this phenomenon disappear. This is because more calculation of the electric potential (E-6.29 and 6.30) will performed in the insulator when extra fine and fine mesh applied. If the size of mesh (normal or coarse mesh) is equivalent or larger than insulator (0.25mm), almost no mesh point will be created on insulator, the calculation of electric field will neglect this part and will introduce the disappearance of the two peak of $\|E\|$.

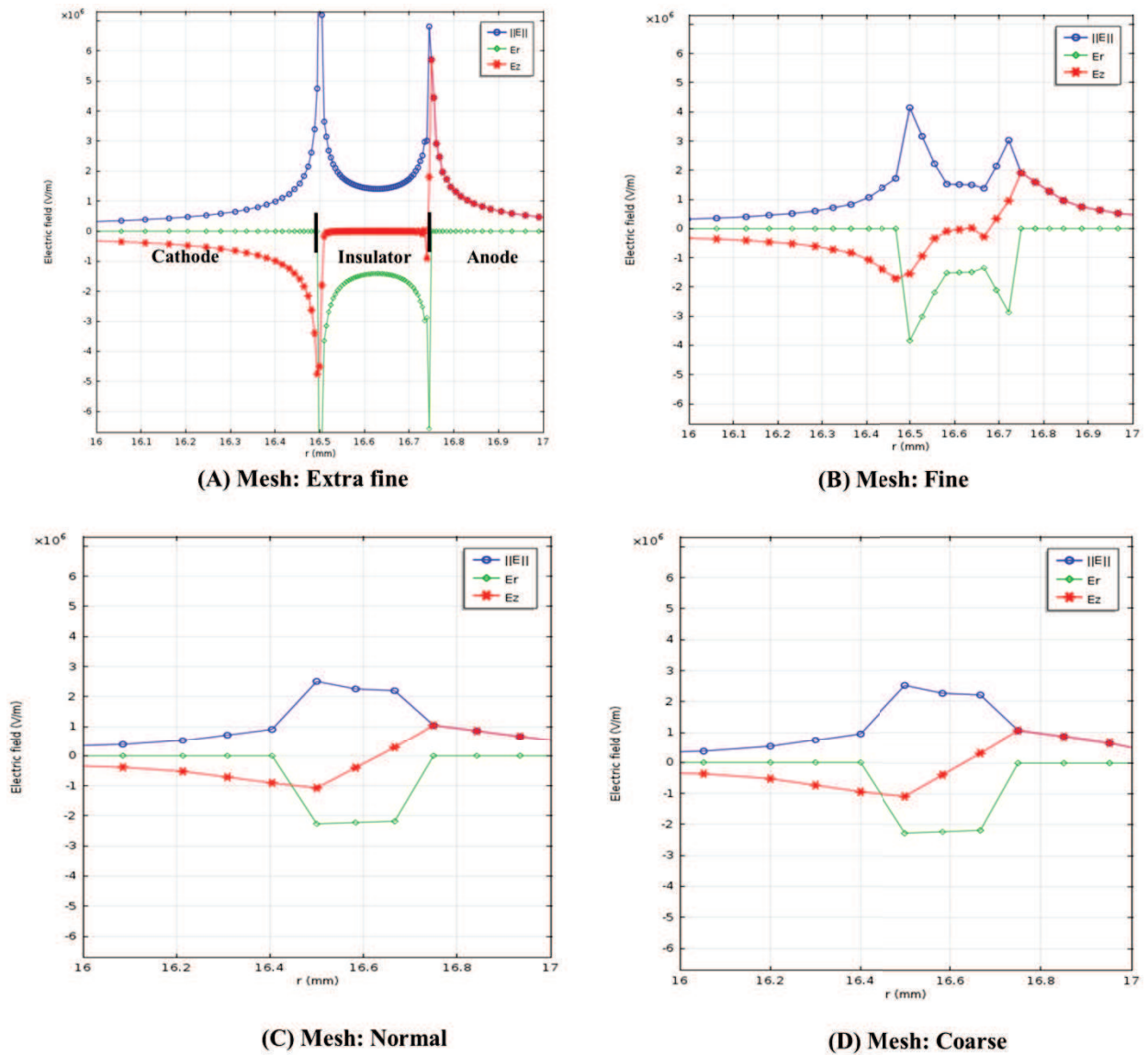


Figure 6.8-the Electric field (E_r , E_z and $||E||$) at $z=0$, (A)-(D) are the different mesh style with extra fine, fine, normal and coarse separately.

The magnetic field (B_r and B_z) with four different mesh style (extra fine, fine, normal and coarse) at $z=0$ is shown in figure 6.9. The magnetic field obtained for both the extra fine and fine mesh agreed with result from Costin's [87, 89] (figure 6.10), while data from the normal and coarse mesh was a little bit inconsistent in the B_z curve indicated with red circles. Based on the result above, it can be concluded that either the extra fine or fine mesh would be adequate for the future simulations but the normal or coarse mesh should no longer be used.

While the result converges and that extra fine meshes can be quite expensive in terms of computation time. Thus the fine meshing is used for all further computations.

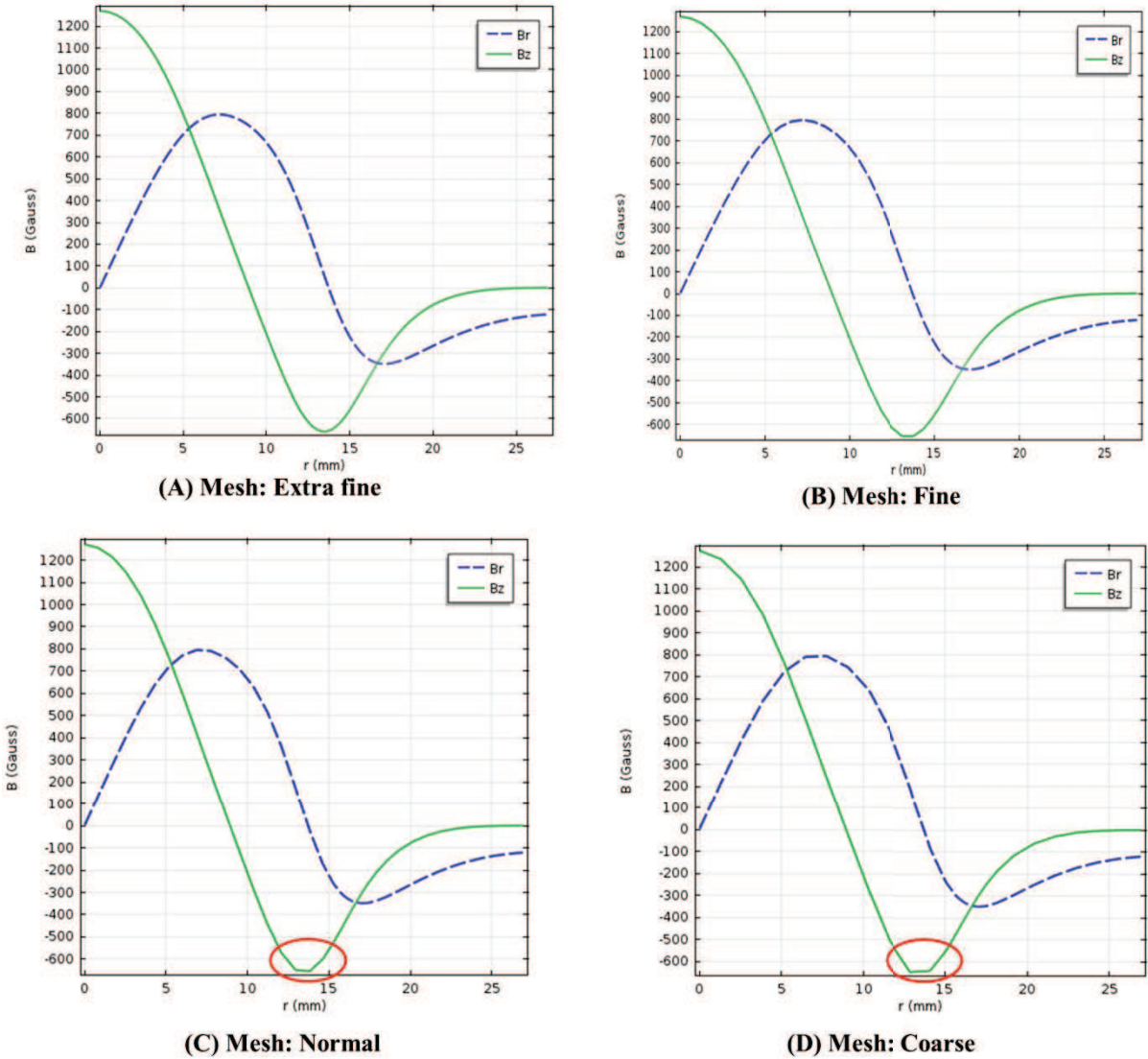


Figure 6.9-the the megnetic field (B_r and B_z) (right) at $z=0$, (A)-(D) are the different mesh style with extral fine, fine, normal and coarse seperately)

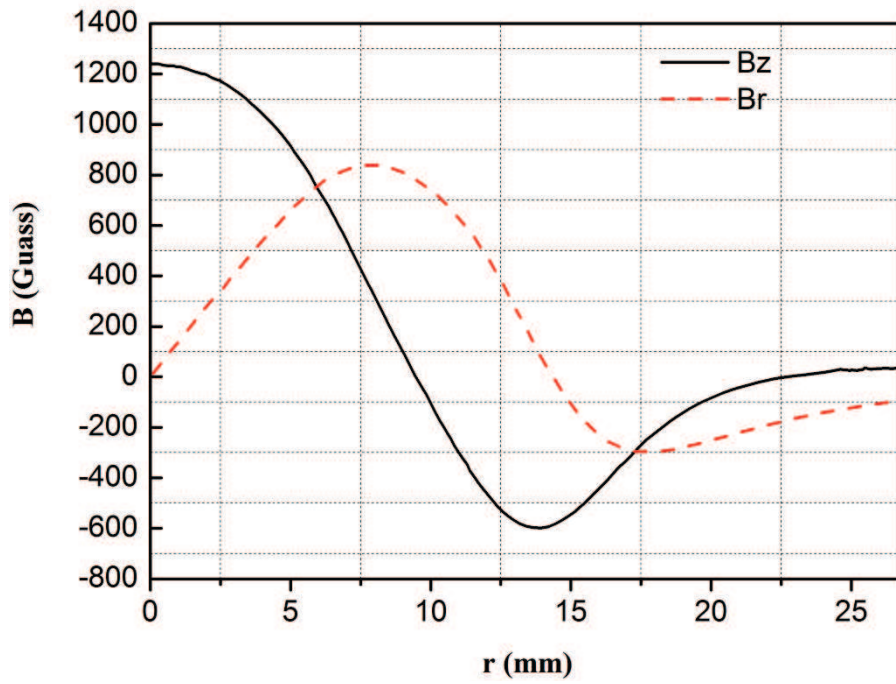


Figure 6.10 the magnetic field at $z = 0$ (B_z left and B_r right) created in Costin's model [89].

The mesh of the geometry with style fine is displayed in figure 6.11 (left); the static magnetic field is simulated and displayed in figure 6.11 (right).

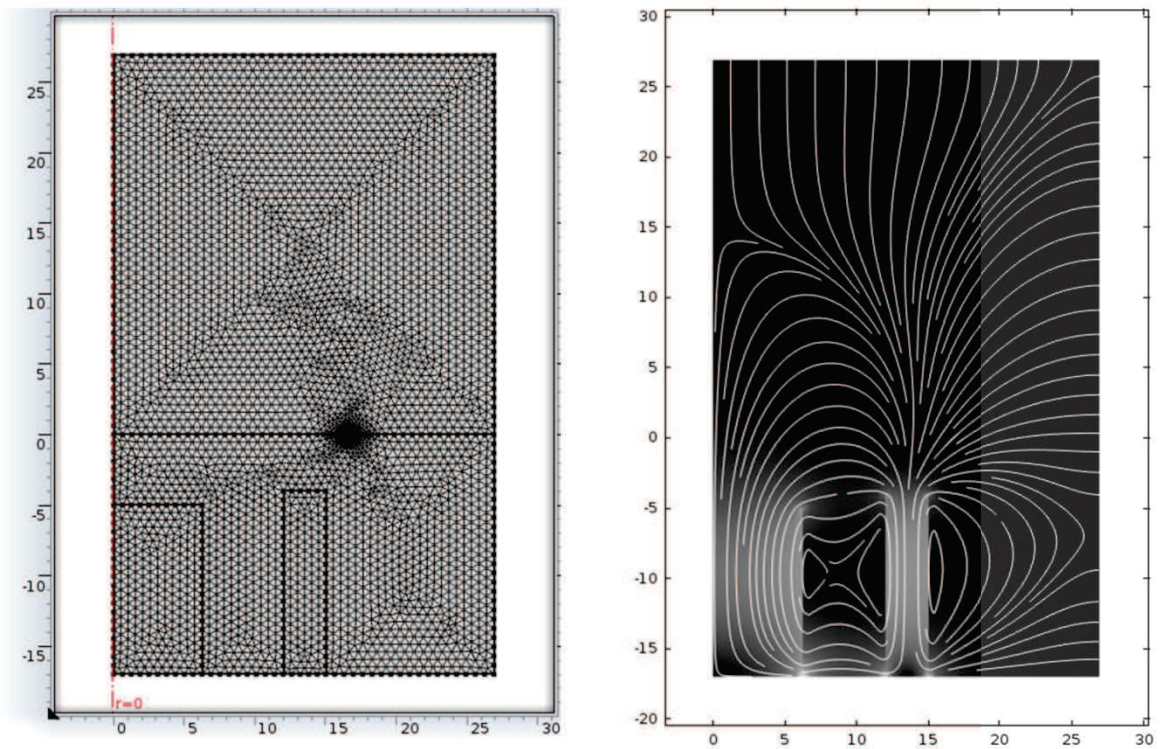


Figure 6.11 – the generated mesh with fine style (left) and static magnetic field created in the simulation (right).

The electric potential are presented in figure 6.12. Considering the inatial value of density of electron and ions are the same (table 6.1), the space charge in the initial stage is zero.

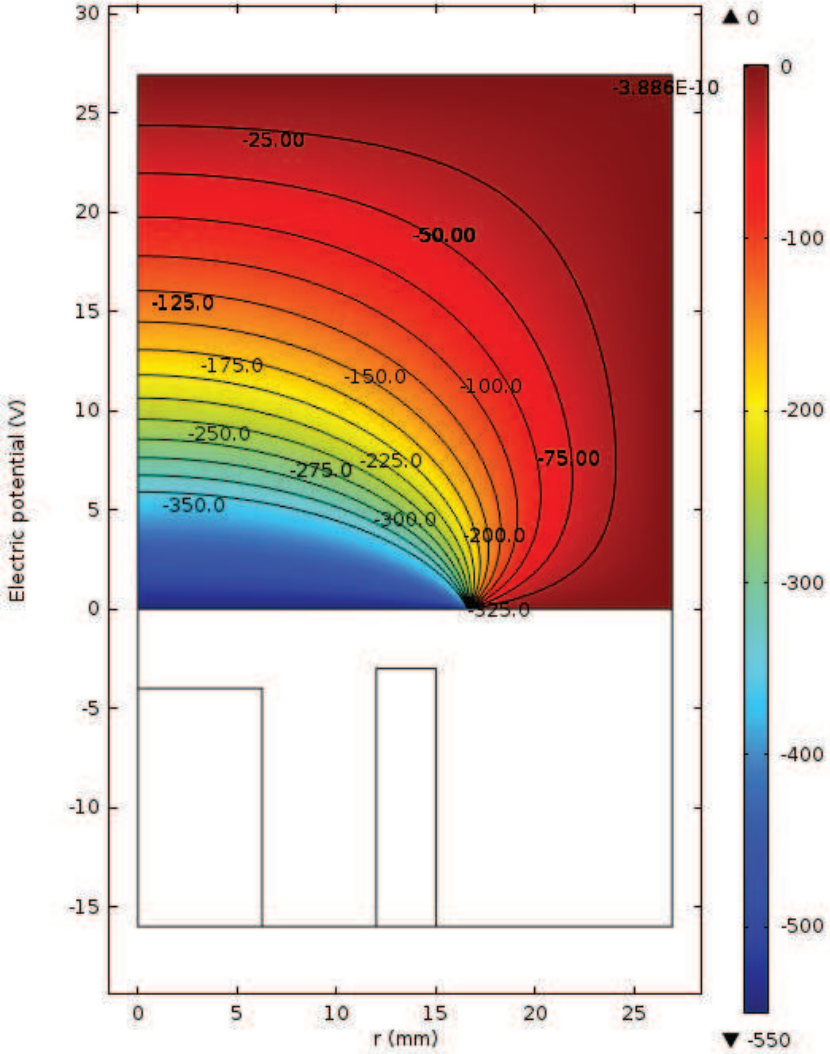


Figure 6.12-The inatial electric potential created in the simulation.

6.5 Conclusion

COMSOL Multiphysics models have been used to perform 2D magnetron plasma discharge model from Costin [87, 89, 90]. The charged particles are described by the fluid model, using a classical drift–diffusion expression for fluxes. The electron flux are separated into two parts and treating the influence of the magnetic field as an additional term in the flux expression.

The effective electric field instead of real electric field is used to characterize the drift-diffusion flux for argon. The preliminary study allowed the choice of a mesh with a good ratio mesh quality / computation time, the calculated magnetic field is in good agreement with the one of Costin [87, 89], as equations are non-linear and highly-coupled, current work is focused on the resolution of n_e , $n_e \mathcal{E}_e$ and n_i equations in particular on the solver setting.

Chapter 7: Conclusion and future work

L'objectif principal de cette thèse est d'étudier le dépôt de couches minces par pulvérisation plasma à l'aide de simulations de dynamique moléculaire, en mettant l'accent sur les mécanismes atomistiques de la formation de la microstructure dans diverses conditions de dépôt pertinentes pour les expériences. Le but de ce travail ne pouvait être atteint sans une bonne connaissance des fondamentaux de la simulation MD et des processus de dépôt par pulvérisation plasma de la croissance de couches minces tels que rappelés dans le chapitre 2.

Sur cette base, trois systèmes différents ont été étudiés:

Des dépôts de films minces de Zr_xCu_{100-x} sur Si (100) par procédé magnétron de co-pulvérisation ont été étudiés par simulations de dynamique moléculaire utilisant des conditions initiales similaires à celles des expériences. Les résultats montrent que la phase de films minces Zr_xCu_{100-x} est déterminée par la composition de l'alliage binaire et par l'énergie cinétique moyenne des atomes incidents.

Les films simulés contenant une grande quantité de l'élément principal (supérieur à 80%) sont cristallisés, alors que pour les compositions intermédiaires, une phase faiblement ordonnée est mise en évidence. Les résultats des simulations de dynamique moléculaire ont été comparés avec les analyses DRX des films minces déposés expérimentalement qui montrent également que la structure des films est cristalline à une teneur élevée ou faible Zr et est amorphe aux quantités intermédiaires, i.e. de 20 à 75% en Zr. En outre, avec des énergies cinétiques supérieures, il est possible de former une couche compacte et uniforme. Avec une énergie plus faible, la morphologie sera en agrégats ou en films en fonction de la composition atomique.

Le chapitre 4 décrit la croissance initiale d'un film mince de HEA puis de son "recuit simulé" sur silicium. Les alliages simulés possèdent la structure fcc / bcc modulée par la composition, en conformité avec l'expérience. En analysant statistiquement les paramètres δ et Ω , une tendance à évoluer vers une solution solide de verres métalliques massifs a été trouvée. Ceci peut être utilisé pour aider à prédire qualitativement la phase structurale en fonction de la composition chimique. Les simulations MD montrent une croissance en agrégats qui évoluent au cours de l'étape de recuit de 200K à 1500K. Une coalescence de cluster induite est observée avant d'être accompagnée par un processus similaire à une fusion des agrégats. Cela commence vers 1050 K où les atomes individuels se déplacent à l'intérieur des agrégats se traduisant par un saut vertical dans la RMSD totale. Par ailleurs, les calculs XRD à différentes températures de recuit montrent une transition entre la phase bcc/fcc en accord avec les expériences.

Dans le chapitre 5, le dépôt par pulvérisation plasma d'atomes de platine sur deux substrats carbonés nanostructurés a été étudié par simulation de dynamique moléculaire à température ambiante (300K) et pour deux ensembles de paramètres de potentiels Lennard-Jones et à trois distributions d'énergie cinétique différentes (1 eV, 0.1eV et 0.026 eV) d'atomes Pt incidents sur le substrat. Lorsque l'on considère la croissance d'agrégats sur les nanotubes de carbone, leurs propriétés dépendent de l'énergie cinétique: Avec une énergie cinétique moyenne élevée (1 eV), des agrégats de Pt denses et bien cristallisés sont formés. Ils reposent sur la base des CNT. A distribution d'énergie moyenne intermédiaire (0.1eV), les agrégats sont cristallins et formés dans la partie médiane des CNT alors qu'à 0.026eV (300 K), des agrégats amorphes sont formés sur le haut des CNT. Ceci provient de la diffusion des atomes de Pt qui est renforcée par l'augmentation de l'énergie cinétique combiné avec un potentiel d'interaction faible entre Pt et les CNT. Il n'y a pas de différence significative entre les deux potentiels d'interaction utilisés en ce qui concerne la morphologie des agrégats. Ce qui semble indiquer que le substrat CNT cristallisé guide fortement la croissance.

La situation est très différente sur le carbone. Les calculs de RDF et XRD des agrégats de Pt déposés sur le carbone poreux avec un potentiel à faible énergie de liaison Pt-C ont une structure amorphe pour l'ensemble des vitesses de dépôt, tandis que pour ceux ayant un potentiel avec une énergie de liaison supérieure montre des amas de Pt présentent une structure bien cristallisée. Cela provient de l'énergie cohésive du Pt qui est suffisamment grande par rapport à l'énergie de liaison de surface pour "ignorer" l'accommodation aux détails de la surface. Au contraire lors de l'utilisation du potentiel pour lequel l'énergie de liaison Pt-C est bien plus grande, les atomes de Pt s'adaptent plus étroitement à la morphologie de surface et ceci conduit à un film plus

bidimensionnel. La structure cristalline reste dans une certaine mesure conservée, en raison de la faible épaisseur.

Les résultats des trois simulations de MD sont en bon accord avec les résultats expérimentaux: il s'avère que la modélisation à l'échelle atomique permet de prédire la structure de films d'une ou quelques centaines de nanomètres d'épaisseur déposés par pulvérisation cathodique magnétron. Les simulations MD peuvent donc être un outil utile pour la conception de nouveaux alliages.

Le chapitre 6 a permis d'introduire la simulation numérique des décharges magnétron avec le logiciel COMSOL en vue de déterminer les paramètres d'entrée pour les simulations de MD. Les particules chargées sont décrites par le modèle hydrodynamique, en utilisant des expressions classiques des flux. Le flux d'électrons est séparé en deux parties et le traitement de l'influence du champ magnétique apparaît comme un terme supplémentaire dans l'expression du flux. Un champ électrique efficace est utilisé au lieu du champ électrique réel pour caractériser le flux des ions argon.

Le but de cette simulation numérique est de déterminer les caractéristiques de l'environnement plasma du dépôt, tels que la distribution des vitesses, la densité d'énergie et la densité des ions et électrons, etc. Ces informations, très proches de la réalité, peuvent alors être introduites comme éléments de modélisation et de conditions initiales dans la simulation MD. L'étude préliminaire a permis de faire le choix d'un maillage d'un bon rapport qualité / temps de calcul. Le champ magnétique calculé est en bon accord avec la référence [1-3]. Les équations sont non linéaires et hautement couplées. Le travail actuel est axé sur la résolution des équations en abordant notamment les paramètres du solveur.

Summary

The primary goal of this thesis was to investigate the plasma sputtering thin film deposition using molecular dynamics simulations, with emphasis on atomistic mechanisms of structure formation and phase composition under various deposition conditions relevant to the real world. The goal of this work can only be achieved with a good knowledge on the fundamentals of MD simulation and the sputter deposition process of the thin film growth. Therefore, in chapter 2 of the thesis, Molecular dynamics (MD) simulations and the implementation of process for describing the magnetron sputter deposition of thin film in MD simulation is discussed. Base on this model, three different systems have been performed:

- 1) In chapter 3, Zr_xCu_{100-x} thin films grown on Si(100) substrate by magnetron co-sputtering process were studied by MD simulations using initial conditions similar to the experimental ones. The results show that the phase of Zr_xCu_{100-x} thin films is

determined by the composition of the binary alloy and affected by the mean kinetic energy of the incoming atoms.

Simulated films containing large amount of one of the element (higher than 80%) are crystallized, whereas for intermediate compositions low ordered phase is evidenced. The results from the MD simulations were compared with XRD analyses of the experimentally deposited thin films. The experimental results also show that the structure of the films changes from crystalline at a high or low Zr content to amorphous at intermediate Zr contents, ranging from 20 to 75%. Besides, with higher depositing energy, it is likely to form a compact and uniform film. With lower energy, the morphology will be clusters or film depending on the atomic composition.

- 2) Chapter 4 described MD simulations initial growth of HEA thin films and its' annealing onto silicon. The simulated alloys were found to possess fcc/bcc structure affected by the composition of their elements which is corresponding to the experiment. By statistically analyzing the parameters δ and Ω for reported HEAs, a tendency to evolve from solid solution to bulk metallic glasses was found, which can be used to assist in qualitative predictions of phase for the HEAs when varying chemical composition. MD simulation reports growth of clusters which evolve during the annealing step from 200K to 1500K. An induced cluster coalescence is observed to be accompanied by a fusion-like process. This is starting around 1050 K where individual atoms are moving inside the clusters leading to a vertical jump in the total RMSD. Moreover XRD calculations at different annealing temperatures show the transition between HEA bcc phase to HEA fcc phase in agreement with experiments.

3) In chapter 5, Plasma sputtering deposition of platinum atoms on two nanostructured carbon substrates was studied by MD simulations at room temperature (300K) and compared against two sets of LJ potential parameters and against three different kinetic energy (1eV, 0.1eV and 0.026eV) distributions of incoming Pt atoms. When considering the cluster growth on CNTs, the properties of Pt clusters depend on the kinetic energy: With higher depositing energy (1 eV), a denser and more crystallized Pt clusters are formed and are supported on the baseline of the CNT. The medium energy distribution (0.1eV) leads to the crystalline clusters formed in the middle part of CNTs while amorphous clusters formed at the tip of CNTs with lowest energy 0.026eV. This comes from the Pt diffusion which is enhanced by increasing the incoming kinetic energy combined with the weak interaction potential between Pt and CNTs. There is no significant difference between the two interaction potentials used regarding the cluster morphology. In both cases crystallized clusters are obtained. This is probably due to the crystallized substrate which drives it.

The situation is quite different on the porous carbon where the less binding potential 1 leads better crystallized clusters. The RDF and XRD of the Pt clusters deposited on porous carbon with potential 2 indicated an amorphous structure for all of the three depositing velocity, while for those with potential 1 with higher binding ability shows the Pt clusters exhibit crystalline structure. This comes from the Pt cohesive energy which is large enough compared to the surface binding energy for “ignoring” the details of the surface. On the contrary when using the more binding potential 2, the Pt will fit closely the surface morphology and leads to a more two dimensional film. The structure remains crystalline to some extent, due to the low thickness.

The results of three MD simulations are in good agreement with experimental results: it proves that modeling at the atomic level allows predicting the structure of hundreds of nanometer thick films grown by magnetron sputter deposition. MD may thus be a helpful tool for designing of new alloys.

Different from three MD simulations above, chapter 6 introduces the numerical simulation of 2D magnetron plasma discharge with COMSOL in view of determining input parameters for further MD simulations. The charged particles are described by the fluid model, using a classical drift-diffusion expression for fluxes. The electron fluxes are separated into two parts and treating the influence of the magnetic field as an additional term in the flux expression. The effective electric field instead of real electric field is used to characterize the drift-diffusion flux for argon ions.

The goal of this numerical simulation was used to characterize the plasma environment of the depositing system, such as the distribution of electron and ion density, velocity of electron and ions, electron energy density, etc. Based on information of plasma, the depositing energy of incoming atoms in MD simulation can be calculated instead of classical formula (modified Thompson formula) and then performed in the MD simulation. The preliminary study allowed the choice of a mesh with a good ratio mesh quality / computation time, the calculated magnetic field is in good agreement with the reference [87, 89, 90], as equations are non-linear and highly-coupled, current work is focused on the resolution of n_e , $n_e \mathcal{E}_e$ and n_i equations, in particular addressing the solver settings.

Future Work

MD simulations can successfully keep track of the short time and small size scale processes that occur during cluster-surface reactions. However, the shortages also arise with it.

With the small size, it is hard to consider the entire process in the real experiment. With the small time scale, some subsequent events (for example, thermally activated atomic migration and surface diffusion), which are very important in determining thin film growth and equilibrium structure, may not be rapid enough to be captured by conventional MD simulations.

For the first problem, as we did in chapter 7, we use numerical approach to characterize the sputtering process in experiment reactor and create a link, the results from numerical simulation concerning the plasma parameters with those of the MD simulation, and so we will have an important numerical tool (MD + multiphysics reactor) for the entire process.

For the shortage of limited time, two methods can solve this problem:

- 1) A hybrid simulation as presented by Jacobsen et al. [100] for metal systems could be used. In this hybrid simulation, MD simulation methods are combined with MC (Monte Carlo) simulation methods. In this way, the short time scale collision events can be modeled using MD simulations while, the long time scale events between the collisions, such as surface diffusion and structure relaxation, can be simulated using MC simulation methods [101].
- 2) Another method is the temperature-accelerated dynamics (TAD) developed by Sorensen and Voter [102]. This method is based on harmonic transition state theory and is a combination of conventional molecular dynamics and statistical mechanics. The main idea behind this method is to study the thermally activated behavior of the system by performing an MD simulation at a higher temperature rather than at

ordinary temperatures. Therefore, the rate of the activated processes can be raised and become accessible to the simulation and the accessible time scale is extended by orders of magnitude while the correct dynamics is still maintained.

In the future work, simulations that can model the deposition process with an experimental deposition rate and conditions to give direct insight into the whole experimental process and provide a more complete picture.

References

- [1] M. Frenklach, Simulation of surface reactions, *Pure And Applied Chemistry*, 70 (1998) 477-484.
- [2] C. Cavallotti, E. Pantano, A. Veneroni, M. Masi, Multiscale simulation of silicon film growth, *Crystal Research And Technology*, 40 (2005) 958-963.
- [3] J. Halley, P. Schelling, Y. Duan, Simulation methods for chemically specific modeling of electrochemical interfaces, *Electrochimica Acta*, 46 (2000) 239-245.
- [4] B.G. David, B. Pascal, Molecular dynamics for low temperature plasma–surface interaction studies, *Journal of Physics D: Applied Physics*, 42 (2009) 194011.
- [5] X. Zhou, H. Wadley, Atomistic simulations of the vapor deposition of Ni/Cu/Ni multilayers: The effects of adatom incident energy, *Journal Of Applied Physics*, 84 (1998) 2301-2315.
- [6] X. Zhou, H. Wadley, R.A. Johnson, D. Larson, N. Tabat, A. Cerezo, A. Petford-Long, G. Smith, P. Clifton, R. Martens, Atomic scale structure of sputtered metal multilayers, *Acta Materialia*, 49 (2001) 4005-4015.
- [7] H. Wadley, X. Zhou, R. Johnson, M. Neurock, Mechanisms, models and methods of vapor deposition, *Progress In Materials Science*, 46 (2001) 329-377.
- [8] B. Alder, T. Wainwright, Molecular dynamics by electronic computers, *Transport processes in statistical mechanics*, (1958) 97-131.
- [9] B. Alder, T. Wainwright, Studies in molecular dynamics. I. General method, *The Journal of Chemical Physics*, 31 (1959) 459-466.
- [10] S. Plimpton, LAMMPS user's manual, Sandia National Laboratory, (2005).
- [11] B. Alder, T. Wainwright, Phase transition for a hard sphere system, *The Journal of Chemical Physics*, 27 (1957) 1208-1209.
- [12] J. Gibson, A.N. Goland, M. Milgram, G. Vineyard, Dynamics of radiation damage, *Physical Review*, 120 (1960) 1229.
- [13] L. Verlet, Computer "Experiments" on Classical Fluids. I. Thermodynamical Properties of Lennard-Jones Molecules, *Physical Review*, 159 (1967) 98-103.
- [14] H.J.C. Berendsen, J.P.M. Postma, W.F. van Gunsteren, A. DiNola, J. Haak, Molecular dynamics with coupling to an external bath, *The Journal of Chemical Physics*, 81 (1984) 3684.

- [15] J. Lennard-Jones, On the forces between atoms and ions, Proceedings of the Royal Society of London. Series A, 109 (1925) 584-597.
- [16] S. Zhen, G.J. Davies, in: *physica status solidi (a)*, WILEY-VCH Verlag, 1983, pp. 595-605.
- [17] L. Zhang, S. Jiang, Molecular simulation study of nanoscale friction for alkyl monolayers on Si (111), *The Journal of Chemical Physics*, 117 (2002) 1804.
- [18] M.S. Daw, M.I. Baskes, Embedded-atom method: Derivation and application to impurities, surfaces, and other defects in metals, *Physical Review B*, 29 (1984) 6443.
- [19] S. Foiles, Application of the embedded-atom method to liquid transition metals, *Physical Review B*, 32 (1985) 3409.
- [20] S. Foiles, M. Baskes, M. Daw, Embedded-atom-method functions for the fcc metals Cu, Ag, Au, Ni, Pd, Pt, and their alloys, *Physical Review B*, 33 (1986) 7983.
- [21] M.S. Daw, S.M. Foiles, M.I. Baskes, The embedded-atom method: a review of theory and applications, *Materials Science Reports*, 9 (1993) 251-310.
- [22] S.M. Foiles, M.I. Baskes, Contributions of the embedded-atom method to materials science and engineering, *MRS Bulletin*, 37 (2012) 485-491.
- [23] X. Zhou, R. Johnson, H. Wadley, Misfit-energy-increasing dislocations in vapor-deposited CoFe/NiFe multilayers, *Physical Review B*, 69 (2004) 144113.
- [24] J. Tersoff, Modeling solid-state chemistry: Interatomic potentials for multicomponent systems, *Physical Review B*, 39 (1989) 5566-5568.
- [25] J. Tersoff, Empirical interatomic potential for carbon, with applications to amorphous carbon, *Physical Review Letters*, 61 (1988) 2879-2882.
- [26] J. Tersoff, New empirical approach for the structure and energy of covalent systems, *Physical Review B*, 37 (1988) 6991.
- [27] J. Tersoff, Empirical interatomic potential for silicon with improved elastic properties, *Physical Review B*, 38 (1988) 9902-9905.
- [28] K. Meyer, I.K. Schuller, C.M. Falco, Thermalization of sputtered atoms, *Journal Of Applied Physics*, 52 (1981) 5803-5805.
- [29] A. Gras-Marti, J.A. Valles-Abarca, Slowing down and thermalization of sputtered particle fluxes: Energy distributions, *Journal Of Applied Physics*, 54 (1983) 1071-1075.

- [30] X. Yang, Y. Zhang, Prediction of high-entropy stabilized solid-solution in multi-component alloys, *Materials Chemistry And Physics*, 132 (2012) 233-238.
- [31] A. Takeuchi, A. Inoue, Classification of bulk metallic glasses by atomic size difference, heat of mixing and period of constituent elements and its application to characterization of the main alloying element, *Materials Transactions*, 46 (2005) 2817-2829.
- [32] C. Klein, A.R. Philpotts, *Earth materials: introduction to mineralogy and petrology*, Cambridge University Press, 2012.
- [33] N. Mattern, Structure formation in Metallic Glasses, *Microstructure Analysis in Materials Science*, (2005) 15-17.
- [34] T. MASUMOTO, Recent progress of amorphous metallic materials, (1994).
- [35] Y. Kawamura, H. Kato, A. Inoue, T. Masumoto, Fabrication of bulk amorphous alloys by powder consolidation, *International Journal Of Powder Metallurgy*, 33 (1997) 50-61.
- [36] Y.Q. Cheng, E. Ma, Atomic-level structure and structure–property relationship in metallic glasses, *Progress In Materials Science*, 56 (2011) 379-473.
- [37] D. Wang, Y. Li, B. Sun, M. Sui, K. Lu, E. Ma, Bulk metallic glass formation in the binary Cu–Zr system, *Applied Physics Letters*, 84 (2004) 4029-4031.
- [38] P. Yu, H. Bai, W. Wang, Superior glass-forming ability of CuZr alloys from minor additions, *Journal Of Materials Research*, 21 (2006) 1674-1679.
- [39] A. aP ă duraru, A. Kenoufi, N.P. Bailey, J. Schiøtz, An interatomic potential for studying CuZr bulk metallic glasses, *Advanced Engineering Materials*, 9 (2007) 505-508.
- [40] T. Mei-Bo, Z. De-Qian, P. Ming-Xiang, W. Wei-Hua, Binary Cu–Zr bulk metallic glasses, *Chinese Physics Letters*, 21 (2004) 901.
- [41] D. Xu, B. Lohwongwatana, G. Duan, W. Johnson, C. Garland, Bulk metallic glass formation in binary Cu-rich alloy series–Cu_{100–x}Zr_x (x= 34, 36, 38.2, 40 at.%) and mechanical properties of bulk Cu₆₄Zr₃₆ glass, *Acta Materialia*, 52 (2004) 2621-2624.
- [42] J. Musil, R. Daniel, Structure and mechanical properties of magnetron sputtered Zr–Ti–Cu–N films, *Surface and Coatings Technology*, 166 (2003) 243-253.
- [43] J. Das, M.B. Tang, K.B. Kim, R. Theissmann, F. Baier, W.H. Wang, J. Eckert, “Work-Hardenable” Ductile Bulk Metallic Glass, *Physical Review Letters*, 94 (2005) 205501.
- [44] N. Karpe, J. Böttiger, J.P. Krog, A. Nordström, Ö. Rapp, Influence of deposition conditions and ion irradiation on thin films of amorphous Cu □ Zr superconductors, *Thin Solid Films*, 275 (1996) 82-86.

- [45] J. Dudonis, R. Bručas, A. Miniotas, Synthesis of amorphous Zr □ Cu alloys by magnetron co-sputtering, *Thin Solid Films*, 275 (1996) 164-167.
- [46] Z. Sha, Y. Feng, Y. Li, Statistical composition-structure-property correlation and glass-forming ability based on the full icosahedra in Cu–Zr metallic glasses, *Applied Physics Letters*, 96 (2010) 061903-061903-061903.
- [47] Z.D. Sha, Y.W. Zhang, Y.P. Feng, Y. Li, Molecular dynamics studies of short to medium range order in Cu₆₄Zr₃₆ metallic glass, *Journal Of Alloys And Compounds*, 509 (2011) 8319-8322.
- [48] G.A. Almyras, C.E. Lekka, N. Mattern, G.A. Evangelakis, On the microstructure of the Cu₆₅Zr₃₅ and Cu₃₅Zr₆₅ metallic glasses, *Scripta Materialia*, 62 (2010) 33-36.
- [49] Y. Zhang, X. Yang, P. Liaw, Alloy Design and Properties Optimization of High-Entropy Alloys, *JOM*, 64 (2012) 830-838.
- [50] Y. Zhang, T. Zuo, Y. Cheng, P.K. Liaw, High-entropy Alloys with High Saturation Magnetization, Electrical Resistivity, and Malleability, *Scientific Reports*, 3 (2013).
- [51] J.-W. Yeh, in: *Annales de chimie, Lavoisier*, 2006, pp. 633-648.
- [52] U. Hsu, U. Hung, J. Yeh, S. Chen, Y. Huang, C. Yang, Alloying behavior of iron, gold and silver in AlCoCrCuNi-based equimolar high-entropy alloys, *Materials Science and Engineering: A*, 460 (2007) 403-408.
- [53] J.-M. WU, S.-J. LIN, J.-W. YEH, S.-K. CHEN, Y.-S. HUANG, H.-C. CHEN, Adhesive wear behavior of Al_xCoCrCuFeNi high-entropy alloys as a function of aluminum content, *Wear*, 261 (2006) 513-519.
- [54] C.-M. Lin, H.-L. Tsai, Evolution of microstructure, hardness, and corrosion properties of high-entropy Al_{0.5}CoCrFeNi alloy, *Intermetallics*, 19 (2011) 288-294.
- [55] J.W. Yeh, S.K. Chen, S.J. Lin, J.Y. Gan, T.S. Chin, T.T. Shun, C.H. Tsau, S.Y. Chang, Nanostructured High - Entropy Alloys with Multiple Principal Elements: Novel Alloy Design Concepts and Outcomes, *Advanced Engineering Materials*, 6 (2004) 299-303.
- [56] H.-W. Chang, P.-K. Huang, J.-W. Yeh, A. Davison, C.-H. Tsau, C.-C. Yang, Influence of substrate bias, deposition temperature and post-deposition annealing on the structure and properties of multi-principal-component (AlCrMoSiTi) N coatings, *Surface and Coatings Technology*, 202 (2008) 3360-3366.
- [57] M.-H. Tsai, J.-W. Yeh, J.-Y. Gan, Diffusion barrier properties of AlMoNbSiTaTiVZr high-entropy alloy layer between copper and silicon, *Thin Solid Films*, 516 (2008) 5527-5530.

- [58] T.-K. Chen, M.-S. Wong, T.-T. Shun, J.-W. Yeh, Nanostructured nitride films of multi-element high-entropy alloys by reactive DC sputtering, *Surface and Coatings Technology*, 200 (2005) 1361-1365.
- [59] T.K. Chen, T.T. Shun, J.W. Yeh, M.S. Wong, Nanostructured nitride films of multi-element high-entropy alloys by reactive DC sputtering, *Surface and Coatings Technology*, 188-189 (2004) 193-200.
- [60] V. Dolique, A.-L. Thomann, P. Brault, Y. Tessier, P. Gillon, Complex structure/composition relationship in thin films of AlCoCrCuFeNi high entropy alloy, *Materials Chemistry And Physics*, 117 (2009) 142-147.
- [61] V. Dolique, A.-L. Thomann, P. Brault, Y. Tessier, P. Gillon, Thermal stability of AlCoCrCuFeNi high entropy alloy thin films studied by in-situ XRD analysis, *Surface and Coatings Technology*, 204 (2010) 1989-1992.
- [62] B. Jelinek, S. Groh, A. Moitra, M.F. Horstemeyer, J. Houze, S.G. Kim, G.J. Wagner, M.I. Baskes, MEAM potential for Al, Si, Mg, Cu, and Fe alloys, arXiv preprint arXiv:1107.0544, (2011).
- [63] S.-W. Kao, J.-W. Yeh, T.-S. Chin, Rapidly solidified structure of alloys with up to eight equal-molar elements—a simulation by molecular dynamics, *Journal of Physics: Condensed Matter*, 20 (2008) 145214.
- [64] P. Brault, G. Moebis, Molecular dynamics simulations of palladium cluster growth on flat and rough graphite surfaces, *The European Physical Journal Applied Physics*, 28 (2004) 43-50.
- [65] C.-C. Tung, J.-W. Yeh, T.-t. Shun, S.-K. Chen, Y.-S. Huang, H.-C. Chen, On the elemental effect of AlCoCrCuFeNi high-entropy alloy system, *Materials Letters*, 61 (2007) 1-5.
- [66] W.-R. Wang, W.-L. Wang, S.-C. Wang, Y.-C. Tsai, C.-H. Lai, J.-W. Yeh, Effects of Al addition on the microstructure and mechanical property of Al_xCoCrFeNi high-entropy alloys, *Intermetallics*, 26 (2012) 44-51.
- [67] J.-P. Tessonier, L. Pesant, G. Ehret, M.J. Ledoux, C. Pham-Huu, Pd nanoparticles introduced inside multi-walled carbon nanotubes for selective hydrogenation of cinnamaldehyde into hydrocinnamaldehyde, *Applied Catalysis A: General*, 288 (2005) 203-210.
- [68] V. Selvaraj, M. Alagar, K.S. Kumar, Synthesis and characterization of metal nanoparticles-decorated PPY–CNT composite and their electrocatalytic oxidation of formic acid and formaldehyde for fuel cell applications, *Applied Catalysis B: Environmental*, 75 (2007) 129-138.

- [69] S.S. Gupta, N. Bandyopadhyaya, J. Datta, Carbon-supported platinum catalysts for direct alcohol fuel cell anode, *Materials And Manufacturing Processes*, 21 (2006) 703-709.
- [70] W. Li, C. Liang, J. Qiu, W. Zhou, H. Han, Z. Wei, G. Sun, Q. Xin, Carbon nanotubes as support for cathode catalyst of a direct methanol fuel cell, *Carbon*, 40 (2002) 787-790.
- [71] S.H. Joo, S.J. Choi, I. Oh, J. Kwak, Z. Liu, O. Terasaki, R. Ryoo, Ordered nanoporous arrays of carbon supporting high dispersions of platinum nanoparticles, *Nature*, 412 (2001) 169-172.
- [72] K.-Y. Chan, J. Ding, J. Ren, S. Cheng, K.Y. Tsang, Supported mixed metal nanoparticles as electrocatalysts in low temperature fuel cells, *Journal Of Materials Chemistry*, 14 (2004) 505-516.
- [73] A. Tseung, S. Dhara, Loss of surface area by platinum and supported platinum black electrocatalyst, *Electrochimica Acta*, 20 (1975) 681-683.
- [74] I. Lee, K.-Y. Chan, D.L. Phillips, Growth of electrodeposited platinum nanocrystals studied by atomic force microscopy, *Applied Surface Science*, 136 (1998) 321-330.
- [75] G. Clark, L. Kesmodel, Ultrahigh vacuum scanning tunneling microscopy studies of platinum on graphite, *Journal of Vacuum Science & Technology B: Microelectronics and Nanometer Structures*, 11 (1993) 131-136.
- [76] J. Pikunic, C. Clinard, N. Cohaut, K.E. Gubbins, J.-M. Guet, R.J.-M. Pellenq, I. Rannou, J.-N. Rouzaud, Structural modeling of porous carbons: constrained reverse Monte Carlo method, *Langmuir*, 19 (2003) 8565-8582.
- [77] S.Y. Liem, K.-Y. Chan, Simulation study of platinum adsorption on graphite using the Sutton-Chen potential, *Surface Science*, 328 (1995) 119-128.
- [78] S.Y. Liem, K.-Y. Chan, Effective pairwise potential for simulations of adsorbed platinum, *Molecular Physics*, 86 (1995) 939-949.
- [79] A. Sutton, J. Chen, Long-range finnis–sinclair potentials, *Philosophical Magazine Letters*, 61 (1990) 139-146.
- [80] M.P. Allen, D.J. Tildesley, J.R. Banavar, Computer simulation of liquids, *Physics Today*, 42 (1989) 105.
- [81] B.H. Morrow, A. Striolo, Assessing how metal–carbon interactions affect the structure of supported platinum nanoparticles, *Molecular Simulation*, 35 (2009) 795-803.
- [82] C.K. Acharya, D.I. Sullivan, C.H. Turner, Characterizing the interaction of Pt and PtRu clusters with boron-doped, nitrogen-doped, and activated carbon: Density functional theory

calculations and parameterization, *The Journal of Physical Chemistry C*, 112 (2008) 13607-13622.

[83] P. Brault, A. Caillard, A. Thomann, J. Mathias, C. Charles, R. Boswell, S. Escribano, J. Durand, T. Sauvage, Plasma sputtering deposition of platinum into porous fuel cell electrodes, *Journal of Physics D: Applied Physics*, 37 (2004) 3419.

[84] A. Caillard, P. Brault, J. Mathias, C. Charles, R. Boswell, T. Sauvage, Deposition and diffusion of platinum nanoparticles in porous carbon assisted by plasma sputtering, *Surface and Coatings Technology*, 200 (2005) 391-394.

[85] P. Brault, C. Josserand, J.-M. Bauchire, A. Caillard, C. Charles, R.W. Boswell, Anomalous diffusion mediated by atom deposition into a porous substrate, *Physical Review Letters*, 102 (2009) 045901.

[86] T.E. Sheridan, M.J. Goeckner, J. Goree, Model of energetic electron transport in magnetron discharges, *Journal of Vacuum Science & Technology A: Vacuum, Surfaces, and Films*, 8 (1990) 30-37.

[87] C. Costin, L. Marques, G. Popa, G. Gousset, Two-dimensional fluid approach to the dc magnetron discharge, *Plasma Sources Science and Technology*, 14 (2005) 168.

[88] P.G.C. Almeida, M.S. Benilov, M.J. Faria, Multiple solutions in the theory of dc glow discharges, *Plasma Sources Science and Technology*, 19 (2010) 025019.

[89] C. Costin, Modélisation d'une décharge magnétron DC dans l'argon et en mélanges argon-oxygène par un modèle fluide, 2005.

[90] C. Costin, G. Popa, G. Gousset, On the secondary electron emission in DC magnetron discharge, *Journal Of Optoelectronics And Advanced Materials*, 7 (2005) 2465-2469.

[91] S. Rossnagel, H. Kaufman, Induced drift currents in circular planar magnetrons, *Journal of Vacuum Science & Technology A: Vacuum, Surfaces, and Films*, 5 (1987) 88-91.

[92] L. Alves, G. Gousset, C. Ferreira, Self-contained solution to the spatially inhomogeneous electron Boltzmann equation in a cylindrical plasma positive column, *Physical Review E*, 55 (1997) 890.

[93] J. Bretagne, G. Calde, M. Legentil, V. Puech, Relativistic electron-beam-produced plasmas. I. Collision cross sections and loss function in argon, *Journal of Physics D: Applied Physics*, 19 (1986) 761.

[94] V.E.e. Golant, A.P. Zhilinskiĭ, I.E.e. Sakharov, *Fundamentals of plasma physics*, Wiley New York, 1980.

- [95] A.D. Richards, B.E. Thompson, H.H. Sawin, Continuum modeling of argon radio frequency glow discharges, *Applied Physics Letters*, 50 (1987) 492-494.
- [96] A. Salabas, G. Gousset, L.L. Alves, Two-dimensional fluid modelling of charged particle transport in radio-frequency capacitively coupled discharges, *Plasma Sources Science & Technology*, 11 (2002) 448-465.
- [97] H. Ellis, R. Pai, E. McDaniel, E. Mason, L. Viehland, Transport properties of gaseous ions over a wide energy range, *Atomic Data And Nuclear Data Tables*, 17 (1976) 177-210.
- [98] A. Phelps, Cross sections and swarm coefficients for nitrogen ions and neutrals in N₂ and argon ions and neutrals in Ar for energies from 0.1 eV to 10 keV, *Journal of Physical and Chemical Reference Data* 20(1991) 557-573.
- [99] B.N. Chapman, *Glow discharge process: sputtering and plasma etching*, Wiley, 1980.
- [100] J. Jacobsen, B. Cooper, J.P. Sethna, Simulations of energetic beam deposition: From picoseconds to seconds, *Physical Review B*, 58 (1998) 15847.
- [101] S. Blackwell, R. Smith, S.D. Kenny, J. Walls, Modeling evaporation, ion-beam assist, and magnetron sputtering of thin metal films over realistic time scales, *Physical Review B*, 86 (2012) 035416.
- [102] M.R. Sorensen, A.F. Voter, Temperature-accelerated dynamics for simulation of infrequent events, *The Journal of Chemical Physics*, 112 (2000) 9599-9606.

Lu XIE

Simulations du dépôt par pulvérisation plasma et de la croissance de couches minces

Résumé :

L'objectif de cette thèse est d'étudier le dépôt de couches minces par pulvérisation plasma à l'aide de simulations de dynamique moléculaire, en mettant l'accent sur les mécanismes de la formation de la microstructure dans diverses conditions de dépôt pertinentes pour les expériences.

Des dépôts de films minces de Zr_xCu_{100-x} et AlCoCrCuFeNi sur Si (100) par procédé magnétron de co-pulvérisation ont été étudiés par simulations de dynamique moléculaire utilisant des conditions initiales similaires à celles des expériences. Les résultats montrent que la phase de films minces Zr_xCu_{100-x} est déterminée par la composition de l'alliage binaire et par l'énergie cinétique moyenne des atomes incidents. Les alliages AlCoCrCuFeNi simulés possèdent la structure fcc / bcc modulée par la composition, en conformité avec l'expérience. Ils ont une tendance à évoluer vers une solution solide de verres métalliques massifs a été trouvée.

Le dépôt par pulvérisation plasma d'atomes de platine sur deux substrats carbonés nanostructurés (carbone poreux et nanotubes de carbone) a également été étudié à température ambiante (300K) et pour deux ensembles de paramètres de potentiels Lennard-Jones et à trois distributions d'énergie cinétique différentes d'atomes Pt incidents sur le substrat. Les résultats des simulations sont en bon accord avec les résultats expérimentaux.

Enfin, la simulation numérique des décharges magnétron a été introduite en vue de déterminer les paramètres d'entrée pour les simulations de MD. Les particules chargées sont décrites par le modèle hydrodynamique, en utilisant des expressions classiques des flux. Les caractéristiques du réacteur sont reproduites par les premières simulations.

Mots clés : dynamique moléculaire, croissance, agrégat, couche mince, plasma, magnétron

Simulations of plasma sputtering deposition and thin film growth

Abstract :

The objective of this thesis is to study the deposition of thin films by plasma sputtering using molecular dynamics simulations, focusing on the mechanisms of formation of the microstructure in various deposition conditions relevant to experiments.

Deposition of thin films AlCoCrCuFeNi and Zr_xCu_{100-x} on Si (100) by magnetron sputtering process of co-sputtering have been studied by molecular dynamics simulations using similar experiments to those initial conditions. The results show that the phase Zr_xCu_{100-x} thin films is determined by the composition of the binary alloy and the average kinetic energy of the incident atoms. The simulated AlCoCrCuFeNi alloys have fcc / bcc structure modulated by the composition in accordance with experience. They have a tendency to evolve into a solid solution of bulk metallic glasses found.

Plasma deposition of platinum atoms spray on two nanostructured carbon substrates (porous carbon and carbon nanotubes) has also been studied at room temperature (300K) and two sets of parameters of Lennard-Jones potential and three distributions of different kinetic energy Pt atoms incident on the substrate. The simulation results are in good agreement with the experimental results.

Finally, the numerical simulation of magnetron discharges was introduced to determine the input parameters for the MD simulations. The charged particles are described by the hydrodynamic model, expressions using conventional flow. The characteristics of the reactor are reproduced by the first simulations.

Keywords : molecular dynamics, growth, aggregate, thin film, plasma magnetron



Groupe de Recherches sur
l'Energétique des Milieux Ionisés
14 rue d'Issoudun BP6744
F-45067 Orléans Cedex 2, France

